TARGETED MAGNETIC HYPERTHERMIA FOR LUNG CANCER

A DISSERTATION
SUBMITTED TO THE FACULTY OF
UNIVERSITY OF MINNESOTA
BY

TANMOY SADHUKHA

IN PARTIAL FULFILLMENT OF THE REQUIREMENTS
FOR THE DEGREE OF
DOCTOR OF PHILOSOPHY

JAYANTH PANYAM
ADVISOR

TIMOTHY SCOTT WIEDMANN
CO-ADVISOR

JANUARY 2013

ACKNOWLEDGEMENTS

Over the past five and a half year as a graduate student, I have had the wonderful opportunity to meet, work with and enjoy the company of numerous delightful people. This rocky road would have been impossible to tread without their generous help and support for which I am deeply indebted.

I would first like to express my deepest gratitude to my advisors Dr. Jayanth Panyam and Dr. Timothy S. Wiedmann. While every graduate student deems themselves fortunate to have a great mentor, my lucky stars have blessed me with two. Their unique areas of expertise have helped me to weave a wholesome picture and gain new perspectives on everyday science, while their constant support and guidance bolstered my scientific development and reinforced my confidence whenever I faltered.

The unmatched brilliance, unwavering dedication and deep motivation of my advisor and mentor Dr. Jayanth Panyam has been the cornerstone of my scientific progress. Throughout my graduate studies, he has been a hallmark of patience – correcting my mistakes, listening to my concerns, addressing my questions, encouraging me to strive for excellence and greeting me with a smile even on the n^{th} time I walk into his office during a day. Thank you very much for being an integral part of this journey.

I have never come across a person wittier than my co-advisor Dr. Timothy S. Wiedmann. His original ideas, constructive criticism and invaluable suggestions have helped me to stay focused and to successfully execute my research. I have spent countless hours in his lab using the induction heating system and performing aerosol studies. All

that time, I've always marveled at the organization and resourcefulness of his lab and never stopped wondering if there are any "cool tools" he doesn't possess. Dr. Wiedmann, I will always be grateful for your help, scientific advice and the insightful chats in your office.

I will also like to acknowledge my committee members – Dr. William F. Elmquist (chair) and Dr. Robert A. Kratzke for critically examining my work and providing invaluable feedback and suggestions. Thank you for being in my advisory committee. Having you in my committee has made this a very enjoyable learning experience.

The role of diversity in scientific learning cannot be undermined, and to this end I must sincerely acknowledge the past and present members of our lab. I have learnt a lot and thoroughly enjoyed the company of my wonderful lab members: Dr. Yogesh Patil, Dr. Ayman Khdair, Dr. Udaya Toti, Dr. Komal Shahani, Dr. Bharat Guru, Dr. Suresh Swaminathan, Dr. Alex Grill, Dr. Marina Usacheva, Lin Niu, Ameya Kirtane, Steve Kalscheuer and Garvey Liu. It has been an absolute pleasure working with them.

Many studies in this thesis could not have been possible without the assistance of several researchers at the University of Minnesota. First and foremost I will like to thank Dr. Pengyun Zeng for introducing me to the world of magnetic particles and their manifold applications. She had also been my go-to person during the initial months after I started this thesis project. I will also like to thank Ying Jing from the Electrical and Computer Engineering Department at the University of Minnesota for her immense help in maintaining and restoring the induction heating equipment to working conditions and for her help with the magnization studies. Thank you to Dr. Josh Parker, Dr. Paula Overn,

Dr. Gerry O'Sullivan and Lindsey Harper at the Comparative Pathology Shared Resource for their extensive assistance with histology and immunohistochemistry. Thanks to Dr. Nisha Shah at the Flow Cytometry Core Facility for her help with cell sorting and other flow cytometry studies. I'd like to thank Dr. Bob Hafner for his help in acquiring TEM images of the magnetic particles. A special thanks to Research Animal Resources, especially Brenda Koniar for her immense assistance with the animal studies and the lively conversations in her office.

I will also like to acknowledge the "Mentor-predoctoral fellow research award" from the Department of Defense for the financial support for this thesis.

I'd like to thank the faculties, staff and students in the Department of Pharmaceutics with a special thanks to Candy McDermott and Erica Stapic for their kindness and help. I cherish the blissful moments with Erica's son Luka whose innocent smile has lit up numerous work-day mornings in the final months of my graduate studies. I'm immensely grateful to Dr. Carolyn Fairbanks for being a part of numerous endeavors of my PhD life. She had been my temporary advisor when I joined the department, the course coordinator of Phar 6164 where I TA-ed multiple times and has never ceased to be anything but a wonderful supporter. Thank you very much.

There is no denying the importance of friends for maintaining sanity during the grueling PhD research. Very special thanks to Cece, for confiding in me, supporting my ideas and for being such a wonderful friend. I really treasure our friendship.

One of the things that kept me awake (apart from my daughter after she was born) was caffeine. It will not be an exaggeration to say that a lot of this work would not have

been completed without a hot cup of flavored roast with extra espresso shots. Thank you Espresso Expose for keeping me on my feet.

Finally, it's time to thank the most important people in my life. I have to heartily thank my parents for believing in me and loving me unconditionally. Your endless efforts for my well-being have brought me where I am now and I can never thank you enough for that. I am immensely fortunate to have an extremely caring elder sister Tanusree. She has always been blind to my flaws and made me believe that I can do anything if I tried. Thank you for everything.

Throughout my graduate studies, my parents-in-law have always appreciated and encouraged my efforts. I sincerely thank them for loving me and accepting me as a part of their lovely family. I am also very grateful to my brother-in-law, Sisir and his family for their ever supportive and loving companionship.

In the walk of life, we come across people who sweep us off our feet with their warm affection and deep caring love and change our lives forever. I met such an amazing girl during my undergraduate studies. Over the years, she has become my best friend, my soul mate, my life-partner and the incredible mother of my precious daughter Pranjoli. Words can't describe how much I'm grateful to you Arpita, my dear wife! You have always been my fortress, my greatest strength and my biggest supporter. You have taken away all the worries from my heart and filled it with love and hope and I will cherish our relationship forever. Thank you for believing in me and for sticking with me through all the harsh winters of our life. Above all, thank you for Pranjoli (Zoey). It's amazing how someone so small, and as cute as a button, can bring so much joy! One minute she's this

“sugar-high” toddler bouncing off the walls, the next minute she’s giggling at her self-created game and then on the next, she’s a warm cuddly angel melting the heart with hugs and kisses. Thank you so much Zoey for brightening our lives. Home would never be home without the two of you. So…Thank you! Thank you! Thank you!!!

DEDICATION

This thesis is dedicated to
my dear parents,
amazing wife
and
precious daughter

ABSTRACT

Lung cancer (specifically, non-small cell lung cancer; NSCLC) is the leading cause of cancer-related deaths in the United States. Poor response rates and survival with current treatments clearly indicate the urgent need to develop an effective means to treat NSCLC. Magnetic hyperthermia is a novel non-invasive approach for ablation of lung tumors, and is based on heat generation by magnetic materials, such as superparamagnetic iron oxide (SPIO) nanoparticles, when subjected to an alternating magnetic field. However, inadequate delivery of magnetic nanoparticles to tumor cells can result in sub-lethal temperature change and induce resistance. Additionally, non-targeted delivery of these particles to the healthy tissues can result in toxicity. To overcome these problems, we used aerosol-based, tumor-targeted SPIO nanoparticles to induce highly selective hyperthermia for the treatment of lung cancer.

Mechanistic study on the mode of cell kill by magnetic hyperthermia revealed that the extent and mechanism of MH-induced cell kill is dramatically altered with aggregation of SPIO nanoparticles. While well-dispersed SPIO nanoparticles induced apoptosis similar to that observed with conventional hyperthermia, sub-micron size aggregates, induced temperature-dependent autophagy through generation of oxidative stress. Micron size aggregates caused rapid membrane damage and acute cell kill, likely due to physical motion of the aggregates in alternating magnetic field. Overall, this work highlighted the potential for developing highly effective anticancer therapeutics through designed aggregation of SPIO nanoparticles.

Cancer stem cells (CSCs) are a sub-population of stem-like cells that are thought to be responsible for tumor drug resistance and relapse. We determined the susceptibility of CSCs to magnetic hyperthermia. Multiple assays for CSCs, including side population phenotype, aldehyde dehydrogenase expression, mammosphere formation and in vivo xenotransplantation, indicated that magnetic hyperthermia reduced or, in some cases, eliminated the CSC sub-population in treated cells. Magnetic hyperthermia demonstrated pleiotropic effects, inducing acute necrosis in some cells while stimulating reactive oxygen species generation and slower cell kill in others. These results suggest the potential for lower rates of tumor recurrence after magnetic hyperthermia compared to conventional cancer therapies.

We then studied the effectiveness of inhalation delivery of tumor targeted SPIO nanoparticles for magnetic hyperthermia treatment of lung cancer. We developed EGFR-targeted, inhalable SPIO nanoparticles for magnetic hyperthermia of NSCLC. EGFR targeting resulted in 50% higher concentration of iron oxide in the lungs 1 week post inhalation, when compared to non-targeted SPIO nanoparticles. Magnetic hyperthermia using targeted SPIO nanoparticles resulted in significant inhibition of *in vivo* tumor growth over a period of one month.

Overall, this work demonstrates the potential for developing an effective anticancer treatment modality for the treatment of NSCLC, using targeted magnetic hyperthermia.

TABLE OF CONTENTS

LIST OF TABLES

LIST OF FIGURES

LIST OF ABBREVIATIONS

7AAD	7-amino actinomycin D
A549-Luc	Luciferase transfected A549 cells
ALDH	Aldehyde dehydrogenase
AMF	Alternating magnetic field
ANOVA	Analysis of variance
BCRP	Breast cancer resistance protein
bFGF	Basic fibroblast growth factor
CM-H2DCFDA	5-(and-6)-chloromethyl-2',7'-dichlorodihydrofluorescein diacetate, acetyl ester
CMV	Cytomegalovirus
CSC	Cancer stem cells
CT	Computed tomography
CTP	Carboxy-terminated pluronic F127
DLS	Dynamic light scattering
DNA	Deoxyribonucleic acid
DPBS	Dulbecco's phosphate buffered saline
EDC	1-Ethyl-3-(3-dimethylaminopropyl)carbodiimide
EGFR	Epidermal growth factor receptor
FBS	Fetal bovine serum
FDA	Food and drug administration
FITC	Fluorescein isothiocyanate

FT-IR	Fourier-transformed infrared spectroscopy
GAPDH	Glyceraldehyde 3-phosphate dehydrogenase
GEMM	Genetically engineered mouse model
GSD	Geometric standard deviation
H&E	Hematoxylin and eosin
HRP	Horse radish peroxidase
HSP70	Heat shock protein 70
LC3B	Microtubule-associated protein light chain 3B
LDH	Lactate dehydrogenase
MA	Micro aggregates
MH	Magnetic hyperthermia
MMAD	Mean median aerodynamic diameter
NA	Nano aggregates
NAC	N-acetyl cysteine
NIH	National institute of health
NM	Commercial SPIO nanoparticles (Nanomag ®)
NMR	Nuclear magnetic spectroscopy
NP	Nanoparticles
NSCLC	Non small cell lung cancer
PARP1	Poly [ADP-ribose] polymerase 1
PBS	Phosphate buffered saline
PDT	Photodynamic therapy

P-gp	P-glycoprotein
PI	Propidium iodide
PI3K	Phosphatidylinositide 3-kinases
ROS	Reactive oxygen species
SCLC	Small cell lung cancer
SD	Standard deviation
SE	Standard error of mean
SPIO	Superparamagnetic iron oxide
Sulfo-NHS	N-hydroxysulfosuccinimide (sodium salt)
TBST	Tris-buffered saline containing Tween 20
TEM	Transmission electron microscopy
VEGF	Vascular endothelial growth factor
w/w	weight by weight
WBH	Conventional hyperthermia (water bath heating)
XRD	X-ray diffraction

Chapter 1

INTRODUCTION

1.1. Non-Small Cell Lung Cancer (NSCLC)

Although lung cancer accounts for only 15% of all newly-diagnosed cancers in the United States, it is the leading cause of cancer-related deaths in the United States [2]. The American Cancer Society provides disturbing statistics for the year 2011, where there were 221,130 new cases and 156,940 estimated deaths from lung cancer [3,4].

The incidence of lung cancer is strongly correlated with cigarette smoking, with about 90% of lung cancers in men and 75-85% of lung cancers in women attributed to smoking [5]. The risk of developing lung cancer in smokers is related to the age at which smoking started, time for which smoking continues and the number of cigarettes smoked. According to estimated projections, an absolutely radical reduction in smoking rates is required to achieve a significant reduction in the prevalence of lung cancer [6]. However, it is worthwhile to note that approximately 10% of patients with lung cancer in the United States are found to be lifelong non-smokers. U.S. Environmental Protection Agency (2007) has estimated that secondhand smoke, i.e. the inhalation of tobacco smoke from other smokers, accounts for about 3000 deaths per year from lung cancer. Furthermore, it was recently reported that exposure to passive smoking during childhood increased the susceptibility to lung cancer in adulthood by 3.6 fold [7]. Asbestos exposure increases the risk of lung cancer nine times and a combination of asbestos exposure with cigarette

smoking raises the risk to as much as 50 times. Lung diseases such as chronic obstructive pulmonary disease are associated with a greater risk (four to six times) for the development of lung cancer even when the effect of concomitant cigarette smoking is excluded. Other causes of lung cancer include air pollution (up to 1% lung cancer deaths), radon gas exposure (estimated 12% lung cancer mortalities) and genetic predisposition.

There are two main types of lung cancer – small cell lung cancer (SCLC) and non-SCLC (NSCLC). NSCLC is more prevalent and accounts for 85% of all lung cancer cases. NSCLC can be further subdivided histologically into adenocarcinoma (40% of all cases), squamous cell carcinoma (25 – 30%), large cell carcinoma (10%) and not otherwise specified histology [8]. The present 5-year survival rate for NSCLC (all stages combined) in the United States is roughly 15%. One reason for this is that the majority of patients are diagnosed at a late stage, locally-advanced or metastatic disease [9] as NSCLC has a tendency for early metastasis. The median survival time of a Stage 4 (metastatic) NSCLC patient is about 8 months. Therefore, for a vast majority of patients with NSCLC, primary care is principally palliative with most of them ultimately succumbing to the disease.

Needless to say, the detection of lung cancer at an early stage is a critical requirement in order to improve the overall survival rate. For diagnosis, lung tumors are almost always first revealed by x-ray. In fact, the prevalent and historical use of x-ray positions this imaging methodology as the standard for detecting and characterizing tumors in the lung. Conventional clinical staging is most often performed with computed

tomography (CT) of the thorax and upper abdomen. However, in spite of being helpful in detecting early-stage tumors, CT is not specifically known to have any effect on reducing mortality rates [10]. Various genetic alterations such as mutations in the tumor suppressor gene p53 [11] and deletion or mutation of the retinoblastoma gene [12] have been reported, thus implicating these proteins as potential markers for the detection of lung cancer. Also, increased levels of angiogenic molecules like the vascular endothelial growth factor (VEGF) in serum and tumor tissue have been associated with poor prognosis in lung cancer patients [13,14]. Gessner et al. [15] reported the breath-based detection of angiogenic markers (VEGF, bFGF, angiogenin) to specifically distinguish between early-stage NSCLC versus chronic obstructive pulmonary disease (COPD) patients and healthy volunteers.

At present, surgical resection is the primary choice of treatment, followed by radiation and/or chemotherapy. Depending on the progression of the disease, surgical removal of large or singular tumor masses may involve removal of parts of a lobe (wedge and segment resection) if affected with very small tumors, one or more lobes (lobectomy), or an entire lung (pneumonectomy). Surgery is a highly invasive and expensive treatment option. Metastatic and locally advanced disease stages are not amenable to surgical resection, and importantly, a majority of patients who undergo surgery eventually experience relapse. A less invasive form of surgery called video assisted thoracotomy [16], utilizes a video camera to assist in visualizing and operating on the lung. Though the surgical incisions made are much smaller than those required for surgical resection, video assisted thoracotomy does not allow a complete lung

examination for identifying and removing lesions that remain undetected by preoperative chest x-ray. Besides, surgical intervention can cause lymphocytopenia [17], which is characterized by a decrease in the number of lymphocytes and is often associated with shorter survival times among patients with advanced stages of lung cancer.

Radiotherapy uses high energy x-rays or other types of radiation to kill tumor cells. Depending on the source of radiation relative to the body, it can be divided into two types. External radiation therapy uses a machine outside the body to send radiation toward the cancer. Internal radiation therapy uses a radioactive substance sealed in needles, seeds, wires, or catheters that are placed directly into or near the cancer. Radiotherapy is a minimally invasive form of cancer treatment. However, it is associated with several adverse effects, which severely impact the quality of life.

For chemotherapy of lung cancer, the most commonly used treatment regimens in the first line setting consist of a platinum containing agent (cisplatin or carboplatin), in combination with vinorelbine, gemcitabine, docetaxel, paclitaxel, or pemetrexed [18-24]. These agents are given in a high dose for a limited duration. All of these combinations have proven to be relatively equivalent in response and toxicity, with most studies reporting response rates of 25 to 50%, with virtually no complete responses [25]. Patients who relapse or become refractory to first line therapy are candidates for second line therapeutic regimens. Second line therapy usually consists of sequential use of single chemotherapeutic agents such as docetaxel or experimental therapy [26].

Recently, there is increased interest in investigating the effect of adding a novel biologic drug or a “targeted agent” in combination with platinum-based chemotherapy.

These agents are proven to have reduced toxicity compared to standard cytotoxic chemotherapy, mainly because of the specificity of the mode of action of these drugs. For instance, the addition of a monoclonal antibody (bevacizumab) that targets VEGF to a platinum based chemotherapy regimen has resulted in enhanced delivery of the chemotherapeutic drugs to the tumor site due to alteration in the tumor vasculature [27], causing a statistically significant improvement in progression-free survival and overall survival [28]. On the other hand, EGFR overexpression has been associated with poor prognosis in 40% to 80% of NSCLC patients [29]. However, treatment with EGFR tyrosine kinase inhibitors, gefitinib and erlotinib showed a dramatic antitumor activity in only a minority of patients harboring mutations in the tyrosine kinase domain of EGFR [30,31].

Other treatment options include laser surgery, cryosurgery, electrocautery, radiofrequency ablation and photodynamic therapy. Laser surgery allows surgeons to remove small amounts of lung tissue, and it is proving useful for improving symptoms in stage II and IIIA patients and in treating cancers that have spread to, and are obstructing, the throat. Cryosurgery or cryotherapy uses a chilled probe to freeze and destroy the tumor cells on contact. Electric cauterization or thermal ablation, which uses electricity to produce heat that destroys tissue, is also under investigation as a treatment for early-stage disease. Radiofrequency ablation is a non-surgical technique that uses an x-ray guided electrode to deliver heat to tissues. Since this technique spares nearby normal tissues, patients tend to have minimal side effects. More research is needed to confirm the benefit of radiofrequency ablation over other, non-surgical treatment options. Recently FDA has approved photodynamic therapy (PDT) for the treatment of both early and late stage lung

cancer [32-35]. Though PDT is non-invasive and has fewer side effects, it has some drawbacks including the need for the tumor to be accessible to the inserted bronchoscope and the limited depth of penetration of the laser light, which renders it inefficient for treating larger tumors. Poor response rates and survival with current treatments clearly indicate the immediate need to develop an effective means to treat NSCLC.

1.2. Hyperthermia as an Anticancer Therapy

Hyperthermia, as a medical intervention, is defined as the heating of an organ or a tissue to a temperature between 41ºC and 46ºC to decelerate growth and sensitize, damage or otherwise destroy tissue [36,37]. A non-invasive approach for tumor ablation, hyperthermia is associated with fewer side effects compared to chemotherapy and radiotherapy, and is highly effective in eradicating localized or deep-seated tumors. In clinical studies, diverse hyperthermic approaches have been used, including local/interstitial and regional hyperthermia, whole body hyperthermia [38,39] and hyperthermic perfusion techniques such as hyperthermic isolated limb perfusion [40-42] and hyperthermic peritoneal perfusion [43,44]. Several clinical studies have shown that hyperthermia, often in combination with radiotherapy, surgery and/or chemotherapy, results in improved tumor response and survival rates [45-50].

There are several molecular effectors of hyperthermia in the treated cells. The cell membrane and cytoskeleton undergo changes in fluidity and membrane potential, resulting in the impairment of transmembrane transport and loss of cellular integrity. In

addition, there is impairment of protein synthesis, denaturation of proteins, and aggregation of proteins in the nuclear matrix. Hyperthermia also results in DNA damage, inhibition of repair enzymes and impaired DNA synthesis. Most of these alterations are fatal and result in the induction of apoptosis [51,52]. Tumor cells upregulate stress proteins such as the heat shock proteins (HSP) to counter hyperthermia [53,54]. Elevated HSP expression can impart increased resistance to subsequent chemotherapy and radiation treatments, thereby promoting tumor recurrence. However, HSP-induced heat resistance can be overcome by optimizing hyperthermia protocols. Monitoring of cellular HSP expression can be employed to develop a treatment strategy that is optimized for tumor ablation without inducing resistance.

1.3. Magnetic Hyperthermia Using Super-Paramagnetic Iron Oxide (SPIO) Nanoparticles

Several techniques have been utilized for localized heating of tumors including microwave radiation, ultrasound, laser and electromagnetic radiation. However, the most commonly used heating method in clinical settings is capacitive heating [55,56]. Capacitive heating is a form of electric heating where an electrically non-conducting material interacts with a conducting surface leading to a loss of internal energy in the conducting surface and a subsequent rise in temperature in the adjacent, non-conducting material [57]. Radiofrequency electric field is often used to produce capacitive heating. However the technique has been challenging in clinical settings due to the requirements of precise positioning of the electrodes in the tumor, size of the tumor and its depth in the body [56].

Thus, from the clinical point of view, it is more desirable to use a simple heat mediator, a substance that mediates heat in the bodily tissue to be dispersed throughout the regions of interest. Magnetic nanoparticles have been examined as heat mediators because of their chemical stability, biocompatibility, and non-carcinogenicity.

The technique of using of superparamagnetic nanoparticles subjected to an alternating magnetic field to generate heat is called magnetic hyperthermia [58]. The first report on the use of magnetic particles for tumor heating by exposure to an alternating magnetic field (AMF) dates back to 1957 [59]. The advantage of magnetic hyperthermia is that the heating temperature and area can be well controlled by adjusting particle size, shape, suspending media and the properties of the alternating magnetic field [60]. There are several magnetic materials that can be used for inducing magnetic hyperthermia, but most studies have focused on magnetic iron oxides, Fe_3O_4 (magnetite) [61,62] and γ–Fe_2O_3 (maghemite) [63,64], which have been proved to be well tolerated in clinical studies. In fact, magnetite is approved for human use as a diagnostic agent, and therefore has a good anticipated safety profile [65]

1.4. Basic Concepts of Magnetism

The basic principle of magnetism is that magnetic induction (B), which is the overall magnetic response of the individual atomic moments of a magnetic material located in a magnetic field of strength, H can be denoted by $B = \mu_0(M + H)$, where μ_0 is the permeability of the free space and M is the magnetization of the material. Depending on the type of magnetic material, different types of magnetic behavior is observed

including paramagnetism, diamagnetism, ferromagnetism, antiferromagnetism, ferrimagnetism and superparamagnetism.

Paramagnetism and diamagnetism exhibit magnetic moments only in the presence of an externally applied magnetic field. Paramagnetic materials have unpaired electrons which are free to align their magnetic moment in any direction. In the presence of an external magnetic field these magnetic moments tend to align in the direction of the field, thus reinforcing it. On the other hand, diamagnetism appears in all materials and is characterized by the tendency of a material to oppose an applied magnetic field thereby weakening it. In contrast to paramagnetic materials, a permanent magnet possesses its magnetic moment in the absence of an external magnetic field and may be ferromagnetic, antiferromagnetic or ferrimagnetic, depending on the net alignment of the magnetic moments. In these materials, the alignment only occurs at temperatures below a certain critical temperature, called the Curie temperature (for ferromagnets and ferrimagnets) or the Néel temperature (for antiferromagnets). Above the critical temperature, the unique magnetic properties are lost.

Superparamagnetism is a form of magnetism where, unlike ferromagnetic or ferrimagnetic substances, paramagnetic behavior is observed even at temperatures below the Curie or the Néel temperature. Superparamagnetic nanoparticles are single-domain magnetic materials composed of very small crystallites. Owing to their small size, thermal fluctuations can change the direction of magnetization of the entire crystal. This unique property makes superparamagnetic particles, attractive candidates for clinical heating applications [66].

1.5. Heating Mechanism of Magnetic Particles

Magnetic materials can exhibit three different heating mechanisms when placed in an alternating field: generation of eddy currents in a bulk magnetic material, hysteresis losses in a bulk magnetic material, and relaxation losses in a single domain magnetic material [60,67]. Due to the small size of superparamagnetic particles and the low frequency of the AMF, inductive heating due to eddy current is negligible [67]. While polydispersity of superparamagnetic substances can result in a small remanence, monodisperse particles (<100 nm) fall in the single domain regime and have no hysteresis loop in a measurement of the induced magnetic field as a function of the applied magnetic field. Hence, the usual mechanism of heating of these particles arises from energy losses due to a combination of the two relaxation processes – Brownian relaxation and/or Néel relaxation [67,68]. In small particles (about 5 – 15 nm) or at a high frequency of AMF, Néel relaxation predominates where the particles remain stationary but magnetic moment rotates away from the original easy axis of the crystal towards the external field in order to orientate the moment across an effective anisotropy barrier within each particle. In contrast, Brownian relaxation is the primary source of heat generation in larger particles (more than 20 nm) or at a lower frequency of AMF. Upon application of an external magnetic field, the particle rotates against the viscous friction of the fluid towards the field with its moment locked along the crystal axis.

Each of the relaxation modes are characterized by the respective time constants. The Néel time constant, τ_N, is independent of the viscosity of the surrounding medium

and at any given temperature T, it is primarily determined by the radius of the magnetic core R_M [68,69]. Mathematically,

$$\tau_N = \frac{\sqrt{\pi}}{2}\tau_0 \frac{\exp \Gamma}{\sqrt[2]{\Gamma}}$$

and $\Gamma = \kappa V_m / k_B T$ where, the constant τ_0 is in the order of 10^{-9} s, κ is the anisotropy constant (3 X 10^4), k_B is Boltzmann's constant (1.38 X 10^{-23}) and V_M is the magnetic volume given by $V_M = \frac{4}{3}\pi {R_M}^3$.

In contrast, Brownian time constant τ_B, depends on the viscosity of the surrounding fluid η and the hydrodynamic radius of the magnetic substance R_H and is given by,

$$\tau_B = \frac{3\eta V_H}{k_B T}$$

V_H is the hydrodynamic volume given by, $V_H = \frac{4}{3}\pi {R_H}^3$ where $R_H = R_M + \delta$, δ being the thickness of the sorption layer on the particles. Since the two modes of relaxation occur in parallel, the effective relaxation time, τ, is given by

$$\frac{1}{\tau} = \frac{1}{\tau_N} + \frac{1}{\tau_B}$$

The quantitative basis of heating superparamagnetic particles by an AMF of strength *H*, is given by [70]:

$$P = \pi \mu_0 \chi_0 H^2 f \frac{2\pi f \tau}{1 + (2\pi f \tau)^2}$$

Where *P* is the volumetric power dissipation or the specific absorption rate, which is defined as the amount of heat released per unit volume of the material per unit time,

$\mu_0 = 4\pi \times 10^7$ (TmA^{-1}) is the permeability of free space, *f* is the frequency (Hz), and χ_0 is the actual susceptibility, which can be calculated by a complex Langevin equation [70]. The resulting temperature increase for these particles depends on the duration of heating Δt, and the specific heat capacity of the sample *c* and is given by $\Delta T = P\Delta t/c$.

1.6. Murine models in lung cancer therapy research

Murine models of lung cancer serve as an important tool for understanding the molecular pathways involved in the development of lung cancer and allow for the development and validation of novel therapeutic approaches as well as identification of markers for early diagnosis. To achieve these goals, it is essential for the mouse lung tumor models to closely mimic the different lung tumor types with respect to both critical genetic alterations and tumor cell characteristics. However, for translation therapy, it is also essential for the models to be quantifiable in terms of alteration of tumor growth after administration of the therapeutics. Every tumor model has its own set of merits and demerits. While some models facilitate easy measurement at the expense of similarity with actual human lung tumors, other models provide remarkable resemblance to the host tumors but are extremely difficult to monitor. However, the most popular models are those that try to achieve a balance between the two.

Xenograft models have been extensively used for preclinical testing of lung cancer therapeutics [71]. The most prevalent model is the ***subcutaneous xenograft model,*** which involves subcutaneous injection of human lung cancer cell lines into immunodeficient mice. This model is widely popular due to its simplistic nature and has

several advantages including easy administration of cells to induce tumors without the necessity of anesthesia and also convenient monitoring of the tumors by direct measurement of tumor dimensions, thereby allowing longitudinal follow up. However the primary drawback of this model is the discrepancy between xenograft origin and host microenvironment [72]. As a consequence of these discrepancies, tumor response to cytotoxic agents, radiation therapy [73] and novel anticancer agents are greatly affected. In addition, these differences might be critical in NSCLC, where hypoxia and neovascularization play a major role in tumor progression [74]. Finally, only a few subcutaneous tumor models disseminate and progress to the metastatic stage, thus rendering this model useless in studying metastasis, a major cause of lung cancer mortalities.

Orthotopic models of lung cancer have been developed over the last two decades. These models can utilize the benefits of organ specificity and tumor microenvironment of lung tumors that mimic the clinical situation and still allow longitudinal follow up. Several techniques are prevalent for the transplantation of human lung tumor cells in their natural pulmonary environment. Intrabronchial [75-77] and intrapleural administration [78,79] of lung cancer cell lines resulted in pleural, locally advanced, or multiple synchronous tumors. Tracheal instillation of lung cancer cells into mice has also been utilized as a non-invasive route of delivery of cells to the lungs. Intravenous [80] injections of certain lung cancer cells like A549 also lead to experimental metastasis and tumor formation in the lungs [81]. Transfection of fluorescent proteins or luciferase enzyme in the lung cancer cells allows for fluorescence or luminescence-based imaging of tumor growth [82]. While

these models are useful in studying therapeutic efficacy of cancer treatments, they are not particularly suitable for studying chemoprevention or identification of lung cancer biomarkers. In addition, these models are studied in immumo-compromised rodents, and thus the role of host immune system on tumor development is overlooked.

A modification of the orthotopic model involves surgical implantation of NSCLC fragment into the lung of immunodeficient mice via thoracotomy [83-85]. Tumor fragments from fresh primary tumors or subcutaneous NSCLC xenografts were inserted into the lung parenchyma, on the visceral pleura, or on the parietal pleura. Mortality rates due to the procedure itself were around 10%, and the engraftment rates ranged between 60 and 100%. This technique requires specialized laboratory techniques and experienced professionals to perform the surgical intervention. Despite encouraging preliminary results [86], lack of systemic metastasis and technically difficulty in performing the procedure have discouraged the widespread use of this model for preclinical NSCLC research.

Carcinogen-induced lung tumor models utilize chemical carcinogens for the induction of tumors. This model is very reproducible and almost invariably results in pulmonary adenoma and adenocarcinomas [87,88]. Spontaneous lung cancer develops in approximately 3% of wild mice, however, the susceptibility to and incidence of spontaneous lung tumors vary largely between strains [89]. Strains that have a high spontaneous lung tumor incidence are also very responsive to chemical induction of lung tumors, for example, exposure to cigarette smoke, tar, or chemically pure carcinogens [87]. A/J and SWR mice are among the most sensitive strains for spontaneous tumor

development, while others range from being somewhat sensitive (O20 and BALB/c) to more resistant (CBA and C3H) to almost complete resistant (C57BL/6 and DBA). Several quantitative carcinogenicity assays [87,90,91] and chemopreventive drug screening systems [92,93] have been developed using this model. A wide variety of chemicals have been used for lung tumorigenesis including urethanes, metals, aflatoxins, and constituents of tobacco smoke such as polyaromatic hydrocarbons and nitrosamines [87,94-96]. One of the primary drawbacks of this model is the difficulty in monitoring tumor development and progression, thereby posing a challenge in performing chronological studies to monitor the efficacy of therapeutic agents.

Introduction of genetic lesions found in human lung cancer into the mouse germline or pulmonary tissue has resulted in the development of murine lung tumors. These ***genetically engineered mouse models*** (GEMM) bear close resemblance the human lung tumors and serve as an important tool for studying NSCLC in mice. These animals are usually p53 mutated, favoring genetic instability and tumor formation. Development of lung tumors driven by oncogenic activation of *K-Ras* [97], *EGFR* [98], *BRAF* [99], *PI3K* [100] or the presence of *EML4-ALK* fusion oncogene [101] have been reported. Compared to other murine lung tumor models, GEMM have the advantage of taking immune response into account. Although GEMM mimics human lung cancer better than other models, it is still far from clinical situation. Mutations of a few oncogenes or tumor suppressors are not representative of the multistep progression of lung cancer occurring in humans. Furthermore, GEMM models result in hundreds of primary NSCLC in the same period of time, which are difficult to follow and to quantify during preclinical testing and through

non-invasive imaging. Despite these drawbacks, recent studies have reported that GEMM may be of interest in evaluating the efficacy of common NSCLC treatments [102].

The use of murine models of lung cancer for studying therapeutic efficacy necessitates sophisticated non-invasive tools to follow tumor development and response to therapy [103]. It is essential to measure tumor size as a function of time and existing techniques such as positron emission tomography-computed tomography or magnetic resonance imaging have been adapted for use on small animals [100,104]. However, these techniques are less suitable for high throughput studies since they are expensive and time consuming. Other sensitive and reproducible techniques for monitoring *in vivo* tumor growth are based on fluorescence and bioluminescence imaging [105,106]. Expression of fluorescent proteins can be coupled to oncogenes in transgenic mouse models or transfected to lung tumor cells in xenograft models, thereby facilitating fluorescent imaging of tumor growth. Similarly, transgenic expression of luciferase or its transfection into the tumor cells forming xenografts allows monitoring and quantification of tumor volume by bioluminescence imaging. Feasible imaging and quantitation techniques and expression of the gene of interest are thus important criteria for the selection of a suitable lung tumor model.

In our studies, we used an experimental A549 lung colonization model for the development of orthotopic lung tumor xenografts. A549 is a human lung adenocarcinoma cell line, which was first established from an explanted tumor of a 58 year old Caucasian male [107]. Several reports suggest that A549 cells overexpress EGFR, which makes it an attractive candidate for studying the effectiveness of EGFR targeted drug delivery. A549-

luc-C8 Bioware® Cell Line (Caliper Lifesciences) is a luciferase expressing cell line derived from A549 human lung squamous carcinoma cells by stable transfection of the North American Firefly Luciferase gene expressed from the CMV promoter. Luciferase expression in these cells can facilitate the visualization of tumor cells in live animals using bioluminescence imaging. Intravenous injection of A549-luc-C8 cells leads to colonization of the lungs by these cells. The cells lodged in the lung alveolar epithelium start multiplying, and the progression of tumor growth can be monitored by bioluminescence imaging after an intraperitoneal injection of the chemical substrate luciferin. Lung bioluminescence increases with time after tumor cell injection as illustrated in Figure 1.1.

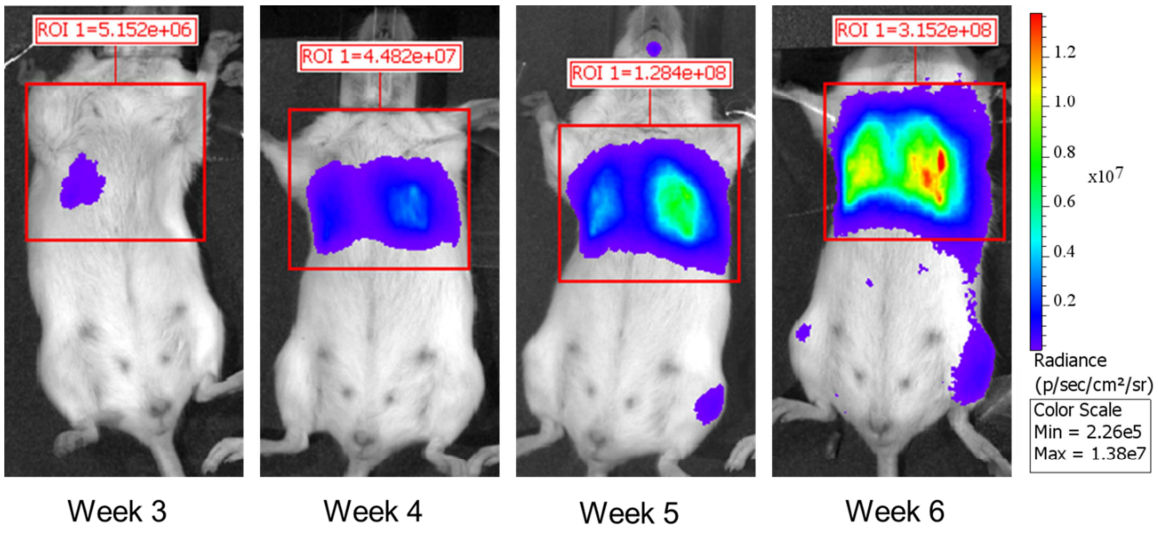

Figure 1.1 Experimental metastatic lung tumor development after A549-Luc cells injection. The luminescence in the lung (tumor) and the radiance between weeks 3 to 6 after tumor cell injection. The absolute value of the radiance is also shown.

1.7. Inhalation drug delivery

Inhalation drug delivery is an attractive option for the treatment of lung diseases. In contrast to systemic delivery, pulmonary delivery is advantageous due to the noninvasive means of delivering high drug concentrations directly to the disease site, which minimizes risk of systemic side-effects while providing rapid onset of clinical response. Additionally, this route bypasses first-pass metabolism in the liver and is also capable of achieving similar or superior therapeutic effect at a fraction of the systemic dose [108-111]. It has been widely accepted as the optimal route of administration of first-line therapy for lung disorders like asthma, chronic obstructive pulmonary disease, cystic fibrosis, and chronic bronchitis [112]. It has also been considered for gene therapy and smoking cessation. An often overlooked and yet promising use of inhalation therapy is for the treatment of lung cancer. While inhaled therapeutics can potentially reach the tumor cells, it is essential to understand the path traversed by these particles in order to develop an optimal therapeutic system.

Human respiratory tract is considered to have two anatomical regions (upper and lower). The upper respiratory tract comprises of the nasal/oral cavity, larynx and pharynx. The lower respiratory tract includes the trachea, bronchi, bronchioles, and alveoli. The trachea follows the larynx as inhaled air moves into the lung. After the trachea, the left and right bronchi are encountered. This is the first of many bifurcations of the respiratory tract, which is repeated until the alveolar ducts are reached. A complex branching pattern arises from these divisions, which in turn affects the mechanism, site of

deposition and dose of therapeutics delivered to the lungs. For most therapeutics, suboptimal dose delivery or uneven distribution in the lungs can compromise the effectiveness of therapy.

Aerosol particle size is one of the most important variables affecting the deposition dose and the distribution of drug in the lung [113-115]. Fine aerosols are distributed on peripheral airways but deposit less therapeutics per unit surface area (due to their smaller mass) than larger particle aerosols which deposit more drug per unit surface area (due to higher mass per particle), but on the larger, more central airways [116]. Most therapeutic aerosols are seldom monodisperse. They consist of a wide range of particle sizes, which is often determined from cascade impaction studies. The particle size follows log-normal distribution and can be quantified by plotting the log of particle diameters against particle number, surface area or volume (mass) on a linear or probability scale and expressed as absolute values or cumulative percentage. There are several ways of defining aerosol particle size. Mass median diameter of an aerosol refers to the particle diameter corresponding to the median of the mass distribution, i.e. it has 50% of the aerosol mass residing above and 50% of its mass below it. The aerodynamic diameter of particles is often defined as the diameter of a sphere of unit density that has the same settling velocity as the particle of interest regardless of its shape or density. The particle aerodynamic diameter (d_a) can be calculated as $d_a = d_h\sqrt{(\rho/\rho_0)}$ where, d_h is mean hydrodynamic diameter determined from light scattering technique, ρ_0 is the standard particle density (1000 kg/m^3) and ρ is the density of the particle of interest. The most commonly used measure of aerosol size is its mean median aerodynamic diameter

(MMAD), which is read from the cumulative distribution curve at the 50% point. Geometric standard deviation (GSD) is a measure of the variability of particle diameters within the aerosol and is calculated from the ratio of the MMAD to the particle diameter at 16% point on the cumulative distribution curve. For a log-normal distribution, the GSD is the same for number, surface area or mass distributions. A GSD of 1 indicates a monodisperse aerosol, while a GSD of >1.2 indicates that the aerosol is heterodisperse.

The aerodynamic size of particles determines the force during the motion of inhaled particles. In the upper airways like the trachea and bronchi, the inertial force of larger particles predominate thereby causing the particles to escape the streamlined flow and collide with the airway wall and deposit [117]. Most particles >10 µm are deposited in the oropharyngeal region due to inertial impaction especially when the drug is inhaled from devices requiring a high inspiratory flow rate (like dry powder inhalers) or when the drug is dispensed from a device at a high forward velocity (like metered dose inhalers) [118]. Ciliary clearance mechanisms transport these larger particles into the oesophagus, where they are subsequently swallowed and contribute minimally, if at all, to the therapeutic response. After the larger particles are cleared in the upper airways, the slightly smaller particles are filtered out of the airstream in the middle airways like the bronchioles and the terminal bronchioles, primarily due to gravitational sedimentation [117]. Finally, very small particles (less than 0.5 µm) are carried to the alveolar region by the airstream where Brownian diffusion is the predominant mechanism of deposition and distribution [119]. While larger particles (>6 µm in humans) are easily cleared from the tracheal region by muco-ciliary clearance [120], very small particles (<1 µm for humans)

are often carried out of the lungs during exhalation [121]. Thus, the highest alveolar deposition in humans is achieved by aerosols having 1 – 5 µm aerodynamic diameter.

The lung size in small rodents like mice is much smaller than that in humans and the diameters of their airways scale proportionately. Additionally, mice are obligate nose breathers, which pose serious challenge in the design of an appropriate inhalation system that allows for high lung deposition of nanoparticles. An MMAD of 1 µm has been shown to result in the highest concentration of the therapeutic agents in all lobes of mouse lungs [122]. This size yields a deposition fraction (percent of mass deposited in the lungs to total mass inhaled) of about 10% [123,124]. However, pre-acclimatization of the animals to the inhalation chambers and prolonged aerosol exposure can prevent undue stress and uneven breathing pattern, thereby increasing lung deposition. Premixing air with carbon dioxide leads to deeper inhalation by the test animals, which in turn can also increase mass delivered into mouse lungs. Other approaches like magnetic deposition of SPIO nanoparticles into the lungs [124] or microspraying technique [125] can also enhance the deposition fraction several folds.

1.8. Tumor targeted drug delivery

An important goal in drug delivery is to enhance the availability of therapeutics at its site of action while minimizing off-target exposure and deposition. One of the techniques for achieving this purpose is by functionalizing nanoparticle surface with cell or organ specific ligands. Several targeting moieties like antibody [126,127], antigen [128,129],

aptamer [130], lectin [131,132], protein/peptide [133,134] and enzyme [135] have been investigated to target cancer cells. Selection of targeting ligands is almost always based on presence or overexpression of the target in tumors of interest.

Several receptors are overexpressed in lung tumors including folate receptor [136], μ-opioid receptor [137], G-protein coupled receptors [138], Insulin-like growth factor-1 receptor [139] and epidermal growth factor receptor (EGFR). Interestingly, EGFR overexpression has been observed in as many as 70% of NSCLC patients [140-142]. In these patients, EGFR overexpression is more frequent in epithelial sites within tumors than those in sites adjacent to and distant from tumors. This suggests that SPIO nanoparticles targeted to EGFR will be specific to tumor cells and will not affect the neighboring healthy cells. Monoclonal antibodies against EGFR (cetuximab) and EGFR tyrosine kinase inhibitors are clinically used for lung cancer. Thus, EGFR is an attractive target in lung cancer.

In our studies, we will use a previously reported 11-residue peptide ligand (YHWYGYTPQNVI) for targeting EGFR. This peptide binds specifically and efficiently to EGFR (dissociation constant of ~20 nM), but has much lower mitogenic activity than EGF [143]. By combining receptor targeting with magnetic activation, superior tumor selectivity is expected.

Although magnetic hyperthermia is a highly promising approach for tumor ablation, currently available techniques for inducing magnetic hyperthermia fail to kill the tumor cells effectively. Inadequate delivery of magnetic nanoparticles to tumor cells

results in sub-lethal temperature change. This can induce resistance in tumor cells, because of induction of heat shock proteins (HSPs). Additionally, non-targeted delivery of these particles to healthy tissues can result in toxicity. To overcome these problems, we propose to use aerosol-based, tumor-targeted SPIO nanoparticles to induce highly selective hyperthermia (Figure 1.2). Aerosolized SPIO particles will be directed to the periphery of the lung by controlling the aerodynamic size of SPIO aggregates. Once the aggregates come in contact with the lung fluids, they will disaggregate to release the individual SPIO nanoparticles. The presence of tumor targeting ligand on the surface will enable SPIO nanoparticles to bind to a greater extent to the tumor cells. SPIO particles that are not bound will undergo muco-ciliary clearance from the lung. Hyperthermia will be induced when the concentration of SPIO particles is the highest in tumors and lowest in normal tissue, thereby preventing toxicity to healthy cells.

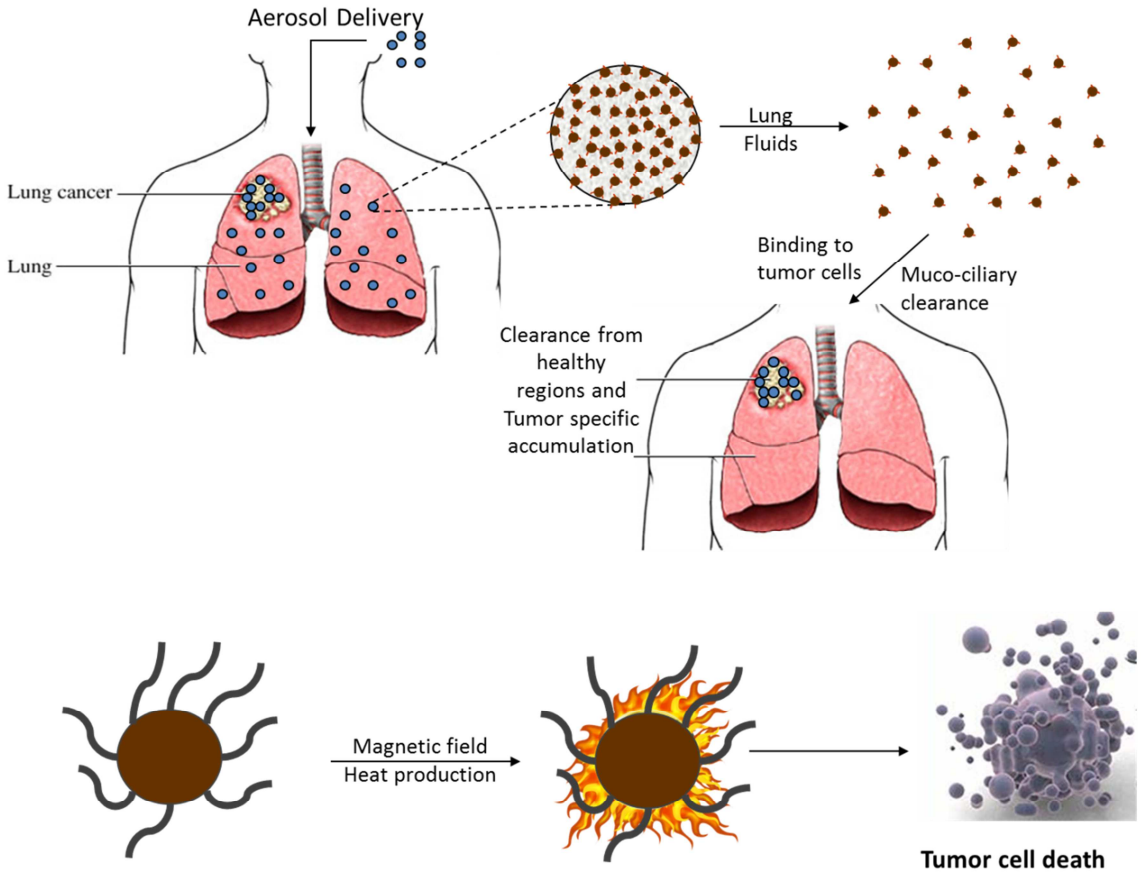

Figure 1.2 Proposed mode of tumor cell kill with targeted magnetic hyperthermia. An inhalable formulation of SPIO nanoparticles conjugated to EGFR targeting ligand will be used. The presence of targeting ligand will enable these particles to bind specifically to the tumor cells. Particles that are not bound are expected to be cleared by muco-ciliary clearance, preventing toxicity to healthy cells. The surfactants in the lung will help disaggregate the formulation into individual targeted SPIO nanoparticles, which are then free to bind to tumor cells. After the unbound particles are cleared from the lung, magnetic field will be applied resulting in heat generation and subsequent tumor cell death.

1.9. Hypothesis and Specific Aims

There are several challenges in developing an effective inhalable lung cancer therapy. The restrictions in the deliverable dose to the lungs warrants a study to determine the most effective mechanism of cell kill. Additionally, lung cancer is notorious for tumor recurrence, where the primary culprit is believed to be cancer stem cells, which are a sub-population of stem-like cells. Thus, it is essential for an effective treatment option to successfully eliminate cancer stem cells. Finally, the major challenge in cancer therapy is the need to specifically target and eliminate malignant cells. The state-of-the-art methods to realize tumor specificity are based on targeting tumor-specific receptors or the use of external stimuli. Receptor targeting provides cell specificity within a specific tissue but suffers from nonspecific systemic distribution. Targeting approaches that utilize activating stimuli such as magnetic hyperthermia provide organ specificity but lack cell specificity in that healthy and malignant cells in a given tissue are equally affected. This is a particular problem in most peripheral lung cancers, because malignant cells are located in the midst of healthy tissue essential for life sustaining respiration. A multi-modal targeting approach involving an external stimulus in conjunction with receptor-based targeting can potentially combine the advantages of the two approaches to specifically target the malignant cells. *We hypothesize that inhalable SPIO nanoparticles surface-functionalized with EGFR targeting ligand, when exposed to an appropriate magnetic field, will enable highly efficient and specific tumor cell death by hyperthermia.* We will test this hypothesis by pursuing the following specific aims:

Specific Aim #1: Determine the mechanism of cell kill by magnetic hyperthermia.

Specific Aim #2: Evaluate the susceptibility of cancer stem cells to magnetic hyperthermia.

Specific Aim #3: Determine the in vivo anticancer efficacy of inhaled EGFR-targeted SPIO nanoparticles

In the following chapters, each aim is addressed. Chapter 2 describes the results of a mechanistic study performed to determine the mode of cell kill by magnetic hyperthermia. SPIO nanoparticles having different extent of aggregation from well-dispersed, non-aggregated nanoparticles to sub-micron size aggregates to larger micron sized aggregates were studied. *In vitro* studies were performed to analyze the extent and mechanism of cell kill by the different particles. The *in vitro* results were verified in an *in vivo* mouse model of subcutaneous A549 lung tumor xenograft. This work highlights the potential for developing highly effective anticancer therapeutics through the modification of the state of aggregation of SPIO nanoparticles. Chapter 3 is focused on studying the effects of magnetic hyperthermia on cancer stem cells. Multiple assays for cancer stem cells, including side population phenotype, aldehyde dehydrogenase expression, mammosphere formation and *in vivo* xenotransplantation, were performed to determine the susceptibility of cancer stem cells to magnetic hyperthermia. This study helped in understanding the long-term effects of magnetic hyperthermia as an anti-cancer treatment modality. In the final study, we developed EGFR-targeted, inhalable SPIO nanoparticles for magnetic hyperthermia of NSCLC. The effect of EGFR targeting on *in vivo* lung tumor retention and the resulting therapeutic efficacy has been discussed in Chapter 4.

Chapter 2

ENHANCING THERAPEUTIC EFFICACY THROUGH DESIGNED AGGREGATION OF NANOPARTICLES

Tanmoy Sadhukha,[a] Timothy S. Wiedmann [a] and Jayanth Panyam[a,b]

[a] Department of Pharmaceutics, [b] Masonic Cancer Center, University of Minnesota, Minneapolis, MN 55455

Keywords: superparamagnetic iron oxide, magnetic hyperthermia, particle size, aggregation, magnetoporation

2.1. Introduction

Nano drug delivery systems are of considerable interest in cancer therapy because of their ability to accumulate passively in tumors [144-146]. A key area of research is the effect of size of the delivery system on therapeutic effectiveness [147-149]. Several reports suggest that the optimal size of nanoparticles for tumor therapy is around 100 nm [146]. However, the presence of proteins can lead to aggregation of nanoparticles in biological environment [150-153]. For example, depending on the surface properties, nanoparticles can form sub-micron to micron size aggregates in the presence of serum proteins [154,155]. The effect of aggregation on the therapeutic performance of nanoparticles has not been previously investigated.

In our studies, we examined the consequence of aggregation on superparamagnetic iron oxide (SPIO) nanoparticle-induced magnetic hyperthermia (MH). Superparamagnetic materials generate heat when placed in alternating magnetic field [156,157]. Depending on the size of the material, heat is generated through either Néel or Brownian relaxation or a combination of the two [67,68]. Heat generated and the associated temperature change from such relaxation phenomena dissipates over short distances due to the high thermal conductivity of water and can therefore be used for highly focused heating [58,158]. This concept is utilized in MH, where an external magnetic field is applied to SPIO nanoparticles trapped in tumor tissue, resulting in local heating and tumor cell kill[58].

Our results show that the extent and mechanism of MH-induced cell kill is dramatically altered with aggregation of SPIO nanoparticles. Aggregated nanoparticles

were much more effective in killing tumor cells than well-dispersed, non-aggregated nanoparticles, and micron size aggregates were more effective than sub-micron size aggregates. Interestingly, cell kill induced by micron size aggregates was largely temperature-independent, and was characterized by acute membrane damage. This is the first report to demonstrate improvements in therapeutic efficacy achieved through designed aggregation of nanoparticles.

2.2. Materials and Methods

2.2.1. Materials

Ferrous chloride tetrahydrate, ferric chloride hexahydrate, myristic acid, Pluronic F127, ascorbic acid, potassium hydroxide, 1,10-phenanthroline and sodium acetate were purchased from Sigma (St. Louis, MO). Penicillin/streptomycin, fetal bovine serum, Dulbecco's phosphate buffered saline, F-12K (Kaighn's modification) and trypsin-EDTA solution were obtained from Invitrogen Corporation (Carlsbad, CA). Cytotox 96® non-radioactive cytotoxicity assay and CellTiter 96® AQueous one solution cell proliferation assay kit were purchased from Promega (Madison, WI). The commercial SPIO nanoparticles (Nanomag®) were purchased from Micromod Partikeltechnologie GmbH (Rostock, Germany). For Western blotting, antibody against HSP70 was from Enzo Life Sciences (Farmingdale, NY), anti-GAPDH-HRP and anti-β-actin-HRP were from Sigma, anti-PARP1, anti-cleaved PARP1, anti-LC3B and HRP-linked anti-rabbit and anti-mouse IgG were from Cell Signaling Technology (Danvers, MA).

2.2.2. Methods

2.2.2.1. Synthesis of SPIO nano and micro aggregates

SPIO nanoparticles were synthesized by condensation of 0.82 g ferric chloride hexahydrate and 0.33 g ferrous chloride tetrahydrate dissolved in 30 ml of degassed and nitrogen-purged water with 3 ml of 5 M ammonium hydroxide. The reaction was allowed to continue for 30 minutes under magnetic stirring (200 gauss magnetic stir bar, 1600 rpm) and nitrogen gas bubbling through the reaction mixture. Iron oxide formed was washed three times with 30 ml of nitrogen-purged water, followed my magnetic separation and heating on a hot (80˚C) oil bath. About 100 mg of myristic acid was added to the heated mixture, which was stirred for another 30 min at 1600 rpm using a 200 gauss magnetic stir bar. Excess myristic acid was removed by two washes with acetone, followed by two washes with water to remove excess acetone. Each wash was followed by magnetic separation of nanoparticles. The myristic acid-coated particles were then suspended in 30 ml water using a water-bath sonicator and 100 mg of pluronic F127 was added and stirred overnight. The final dispersion was fractionated by centrifugation at 800 *g* for 6 minutes. The supernatant contained nano aggregates. The pellet was dispersed in 15 ml of water and 20 mg pluronic F127 by sonication for 1 hour and was comprised of micro aggregates.

Coumarin-6 labeled SPIO nanoparticles were synthesized by incorporating coumarin-6 into the fatty acid layer of SPIO nanoparticles dispersed in water[159]. 1 ml of 500 µg/ml coumarin-6 in ethanol was added to 100 mg magnetite equivalent of SPIO NP in 10 ml of water and stirred overnight. The coumarin-6 labeled SPIO nanoparticles were

washed thrice in water followed by magnetic separation of nanoparticles. The final product was dispersed in 10 ml of water and 5 mg pluronic F127 and observed under a fluorescent microscope to confirm the presence of dye-label on particles.

2.2.2.2. Characterization of SPIO nanoparticles

The hydrodynamic diameter of SPIO nanoparticles was determined by dynamic light scattering. About 1 mg of SPIO nanoparticles was dispersed in 2 ml of deionized water by sonication and the dispersion was subjected to particle size analysis using a Delsa™ Nano C Particle Analyzer (Beckman, Brea, CA). Measurements were performed at 25°C and at a 165° scattering angle. Mean hydrodynamic diameter was calculated based on size distribution by weight, assuming a lognormal distribution. For transmission electron microscopy (TEM), a drop of an aqueous dispersion of SPIO nanoparticles was placed on a Formvar-coated copper grid (150 mesh, Ted Pella Inc. Redding, CA). Excess liquid was removed using a filter paper, and the grid was allowed to air-dry. Particles were imaged using a JEOL JEM-1210 transmission electron microscope (Peabody, MA). The diameters of at least 100 different particles were measured using ImageJ software and averaged to determine the mean Feret's diameter.

The form of iron oxide was assessed by Fourier-transformed infrared spectroscopy (FT-IR). About 5 mg of SPIO nanoparticles was analyzed using Vertex 70 FT-IR spectrophotometer (Bruker Optics Inc., Billerica, MA). Scans were performed

from 4000 cm^{-1} to 400 cm^{-1} and each spectrum was obtained by averaging 16 interferograms at a resolution of 2 cm^{-1}. The data was collected and analyzed using OPUS software (Bruker Optics Inc., Billerica, MA). Magnetic properties were determined with an accurately weighed sample of SPIO nanoparticles, which was sprinkled on a lightly greased silicon wafer and placed in a vibrating sample magnetometer (Micromod Model 3900, Princeton, NJ) operating at room temperature. Magnetization curves were recorded in magnetic fields ranging from -1 T to 1 T, at increments of 0.002 T. The curve was normalized to the weight of magnetite to obtain the saturation magnetization per gram of magnetite. The composition of SPIO nanoparticles was estimated using 1,10 phenanthroline-based iron assay[160]. SPIO nanoparticles were dissolved in 12 N hydrochloric acid. The solution was then diluted with distilled water to obtain a final acid concentration of 0.2 N. To this acid solution, 10 mg/ml ascorbic acid, 1.2 mg/ml 1,10 phenanthroline, 22.4 mg/ml potassium hydroxide and 123 mg/ml sodium acetate were added in a volume ratio of 1:1:1:1:5. Absorbance of the resultant solution was measured at 490 nm using a microplate reader (ELx800 Absorbance Microplate Reader, Biotek, Winooski, VT). Commercial iron oxide powder and ferric chloride (hexahydrate) solutions in 0.2 N hydrochloric acid were used as standards.

2.2.2.3. Cell culture studies

A549 (human lung adenocarcinoma) and A549-Luc (stable luciferase expressing) cells were used in the study. Both cells were propagated using F-12K medium supplemented with 10% fetal bovine serum (FBS) and 1% antibiotic solution and maintained at 37 °C and in 5% carbon dioxide.

2.2.2.4. Cell death after magnetic hyperthermia

About 1 million cells were suspended in 500 µl of F-12K (with 10% FBS) and mixed with 500 µl SPIO nano or micro aggregates in saline to make a final concentration of 1.75 mg/ml magnetite. The suspension was placed in AMF (6 kA/m, 386 kHz) for 5, 15 or 30 min, maintaining the temperature of the cell suspension between 43 – 46°C. Cells not exposed to AMF, with or without SPIO nanoparticles, served as control. Additionally, cells were kept in a water bath for 30 min at 46 °C, to serve as conventional hyperthermia controls. Magnetic hyperthermia induced using a commercial formulation of dextran-coated SPIO (Nanomag®-D-SPIO) was also used for comparison of *in vitro* efficacy. Cells were pelleted 2 hr following treatment, and the amount of LDH released by the cells in the supernatant was determined. LDH released by same number of freeze-thaw lysed cells was used to calculate 100% cell death. In addition, 50,000 treated cells were plated per well in a 24-well plate and assayed for cell survival after 24 hours by MTS assay.

2.2.2.5. Instantaneous PI uptake during AMF exposure:

About 1 million cells were suspended in 500 µl of F-12K (with 10% FBS) and incubated with 500 µl nano or micro aggregates or Nanomag® in saline (final concentration of 1.75 mg/ml magnetite) at 4°C for 30 minutes. 10 µM PI was added to each tube and the treated cells were subjected to 30 minutes of AMF while maintaining the cell suspension temperature below 5°C by using an ice bath. Cells not exposed to AMF, with or without SPIO nanoparticles, were used as controls. Following AMF exposure, cells were immediately washed with buffer, resuspended in medium and kept

on ice. PI present in cells was detected in the FL-3 channel of the flow cytometer (BD, FACSCalibur™). Data from 10,000 cells in each group were analyzed using Cyflogic software.

2.2.2.6. Reactive oxygen species (ROS) generation

Immediately prior to the addition of SPIO formulations, 5-(and-6)-chloromethyl-2',7'-dichlorodihydrofluorescein diacetate acetyl ester (CM-H_2DCFDA) (7.5 µM) and PI were added to the cell suspension. Cells were subjected to flow cytometric analysis after 2 hours. The deacetylated and oxidized product, 2',7'-dichlorofluorescein, formed due to ROS generation in the cells, was detected in the FL-1 channel while PI fluorescence was detected in the FL-3 channel.

2.2.2.7. Western blotting analysis

Cells were lysed using RIPA buffer containing protease inhibitor cocktail (Sigma) on ice. Cell lysates were centrifuged at 13,000 rpm for 10 min to pellet the insoluble cellular debris, and the supernatant was analyzed. Protein concentration in the supernatant was determined by the bicinchoninic acid assay (Thermo Scientific). Protein samples (15 µg) were loaded onto a 4 - 15% Tris-hydrochloride gel (Bio-Rad Laboratories) and, after electrophoresis for 40 min at 100 V, transferred onto a nitrocellulose membrane (Whatman) using a Criterion blotter (Bio-Rad Laboratories). The membrane was blocked with 5% non-fat dry milk in tris-buffered saline containing Tween 20 (TBST) for 1 hr. The membrane was then incubated overnight at 4° C with primary antibodies against PARP1, cleaved PARP1, HSP70, LC3B, GAPDH-HRP or β-actin-HRP, diluted in either 5% non-fat dry milk in TBST or 5% BSA in TBST. After

three 8-min washes with TBST, the membrane was incubated with horseradish peroxidase-conjugated anti-rabbit (for PARP1, cleaved PARP1 and LC3B) or anti-mouse (for HSP70) IgG in 5% non-fat dry milk in TBST for 1 hr and then washed three times with TBST. Protein bands were then visualized using SuperSignal West Pico Chemiluminescent Substrate (Thermo Scientific). For densitometric quantification, immunoblots were digitized on a flatbed scanner and the signal intensities of the visualized bands were quantified using ImageJ (NIH) and OriginPro 8 software (OriginLab Corporation, Northampton, MA).

2.2.2.8. Confocal microscopy

Following incubation with coumarin-6 labeled SPIO nanoparticles and AMF exposure, cells were stained with LysoTracker ® red DND-99 (Invitrogen) for 30 minutes at 37°C or Texas red® -X conjugated wheat germ agglutinin (Invitrogen) for 10 minutes at 37°C and washed with phosphate buffered saline. Ten µl of the cell suspension was added to a glass slide, mounted by a cover glass and sealed with clear nail polish. The slides were imaged using a 40X/1.30 numerical aperture oil-immersion objective in an Olympus FluoView FV1000 BX2 upright confocal microscope (Olympus Corporation). The images were analyzed using FV1000 Viewer software (Olympus Corporation) and ImageJ (NIH).

2.2.2.9. Synthesis of iron oxide microparticles

Uniform spherical magnetite particles were prepared from ferrous hydroxide gels following the procedure of Sugimoto and Matijevic [161]. Ferrous hydroxide was first precipitated as an aqueous gel, which was then aged at 90°C in the presence of nitrate

ion. The final particle size distribution was controlled by the ratio of KOH to $Fe(OH)_2$ ratio. About 201 mg of KNO_3 (Mallinkrodt) was combined with 250 mg of $FeSO_4.7H_2O$ (Sigma-Aldrich) in 10 ml of degassed de-ionized water that was purged with N_2. The reaction mixture was bubbled with nitrogen until the components were dissolved, and then 0.4 ml of 1.25 M KOH (Sigma-Aldrich) was added to produce a green gel. The gel was sonicated in a bath sonicator for 5 s, and the sealed vial was then placed in a glycerin bath maintained at 90°C (±2°C). After 2 hrs, 38 mg of myristic acid (Aldrich) was added to the reaction mixture followed by sonication. The vial was placed in a glycerin bath equilibrated at 80°C for 20 min. The mixture was vortexed and sonicated after every 10 min to redisperse the fatty acid among the particles. After cooling, the coated particles were separated from the reaction mixture by rinsing with acetone to remove unreacted fatty acid and with deionized water to remove the salt. To the particle dispersion, 40 mg of pluronic F127 was added and then sonicated in a bath sonicator for 1 hour to yield the final iron oxide microparticles.

2.2.2.10. PI uptake by cells in rotational magnetic field

Rotating magnetic field was generated by mounting a disc neodymium magnet diametrically on top of a variable speed magnetic stirrer (set at 500 rpm) [162]. About 10,000 A549 cells were plated in a 24-well plate and after 24 hours, 500 µl of media (F-12K + 5% FBS) containing 500 µg magnetite equivalent of nano or micro aggregates were added to the plated cells. Untreated controls received media without any particles. 10 µM PI was also added to the wells for detecting cells with compromised membranes. Some of the nano and micro aggregate groups were placed on the rotating magnetic field

(100 mT, adjusted by changing the distance from the magnet) for 4 minutes. After exposure, 0.1 µM calcein AM (to label viable cells) was added to the wells, which were then observed under a fluorescent microscope.

2.2.2.11. In vivo tumor growth studies

The study was carried out in compliance with protocol approved by the Institutional Animal Care and Use Committee at the University of Minnesota. Female BALB/c-nude mice (C.Cg/AnNTac-*Foxn1*^{nu} NE9; Taconic Farms), four to six weeks of age, were used for the studies. 1 million A549-Luc cells were injected subcutaneously in the abdominal region of the mice and the tumor dimensions were measured every alternate day using digital calipers. The tumor volume (V) was calculated using the formula $V = 0.5(L \times W^2)$, where L and W are the longest and shortest diameters, respectively. When the tumor volume reached 150 mm^3, 40 µl of saline or 225 µg magnetite equivalent of nano or micro aggregate suspension was injected intratumorally and allowed to distribute inside the tumor for 24 hours [163]. After 24 hours, animals in the MH groups were anesthetized and their abdominal region (tumor region) was exposed to AMF (6 kA/m, 386 kHz) for 30 minutes. The tumor temperature was measured using an infrared camera (Infrared solutions) where snapshots of the AMF exposed tumor region of the mice were acquired every 2 minutes. The temperature elevation in the tumor during MH was added to the normal body temperature (assumed to be 37°C) to obtain the calculated tumor temperatures. Tumor volumes were measured every alternate day after treatment by calipers and bioluminescence imaging (IVIS Spectrum, PerkinElmer) of the tumors was performed every week. Development of 1000 mm^3 tumors or 30 days after

cell injection (whichever came first) marked the end of the study for each animal. At the end of the study, the tumors were excised, formalin fixed, paraffin embedded, sectioned and stained with Prussian blue (for iron) or hematoxylin and eosin (for cellular structure). In a separate set of animals, the tumors were excised immediately after MH treatment and processed for Prussian blue and hemetoxylin-eosin staining.

2.2.2.12. Statistical analysis

Statistical analyses were performed using one-way ANOVA, followed by Bonferroni-Holm testing for comparison between individual groups. A probability level of $P < 0.05$ was considered significant.

2.3. Results and Discussions

2.3.1. SPIO nanoparticle aggregate size affects the mechanism of cell kill by MH

To study the effect of aggregation on therapeutic performance, we used a synthetic technique that facilitated the aggregation of SPIO nanoparticles. The final product was fractionated into micro and nano size aggregates. Nano aggregates had an average hydrodynamic diameter of 207 ± 3 nm. Micro aggregates had an average size of 1052 ± 65 nm. The aggregates were composed of 12 ± 3 nm iron oxide cores (Figure 2.1), which were confirmed to be magnetite (Figure 2.2a). Both nano and micro aggregates had high saturation magnetization of 72.9 and 67.7 emu/g of magnetite,

respectively, with negligible remanence (1.64 and 1.44 emu/g of magnetite, respectively) and coercivity (2.73 and 2.36 Oe), verifying their superparamagnetic nature (Figure 2.2b). The heating profiles for the two fractions were virtually identical (Figure 2.2c), further verifying their similar magnetic properties.

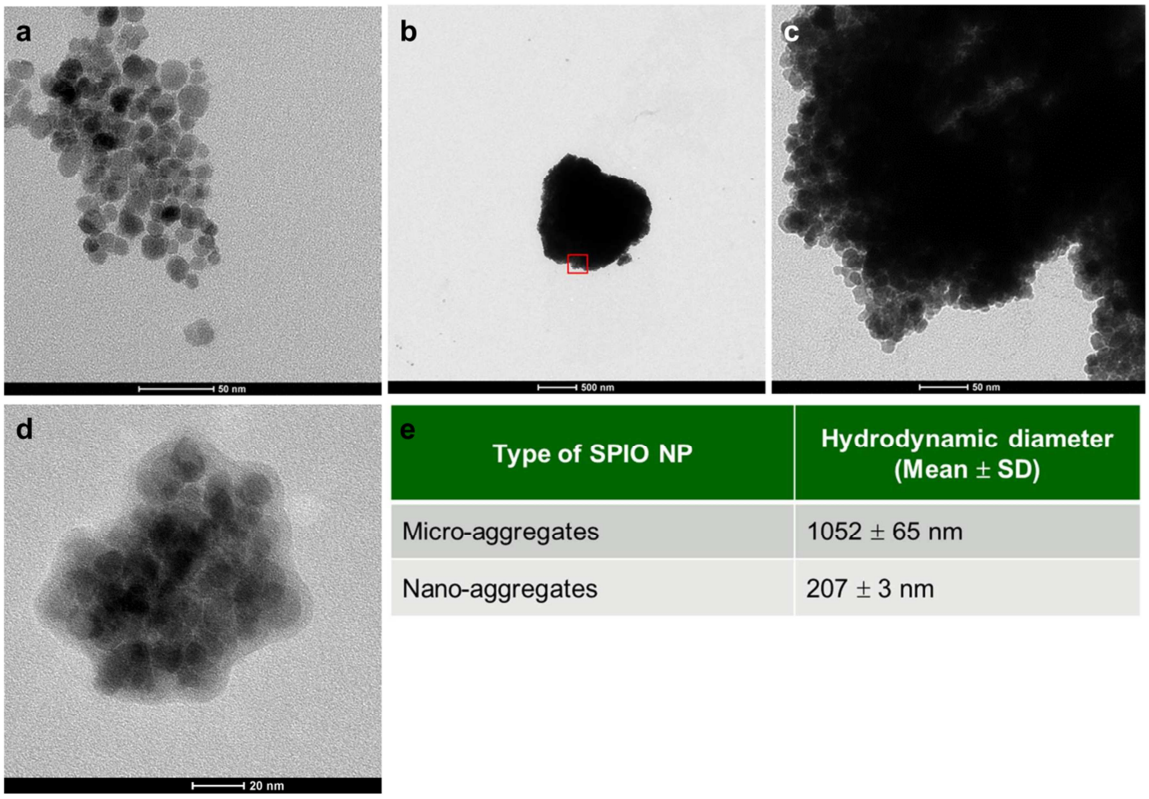

e

Type of SPIO NP	Hydrodynamic diameter (Mean ± SD)
Micro-aggregates	1052 ± 65 nm
Nano-aggregates	207 ± 3 nm

Figure 2.1 Size of SPIO aggregates. **(a)** Representative TEM image of SPIO nano aggregate showing a 100-200 nm aggregate composed of 12 ± 3 nm SPIO core (average Feret's diameter of 100 different SPIO cores measured using ImageJ software). Scale bar, 50 nm. **(b)** TEM image of micro aggregates showing a large electron dense particle (about 1.5 µm in size). Scale bar, 500 nm. **(c)** Higher magnification image of the boxed area of (B) demonstrating that the micro aggregates are also composed of the smaller SPIO cores tightly packed together to form the larger structure. Scale bar, 50 nm. **(d)** TEM image of uranyl acetate counterstained SPIO nano aggregates showing that the SPIO cores are enveloped by myristic acid/pluronic F127 coating to form stable aggregates. The size of micro aggregates interfered with the visualization of coating on them. **(e)** Average hydrodynamic diameter of nano and micro aggregates measured by DLS. Data shown is mean ± SD of five individual size measurement runs, with each run recording 150 size events.

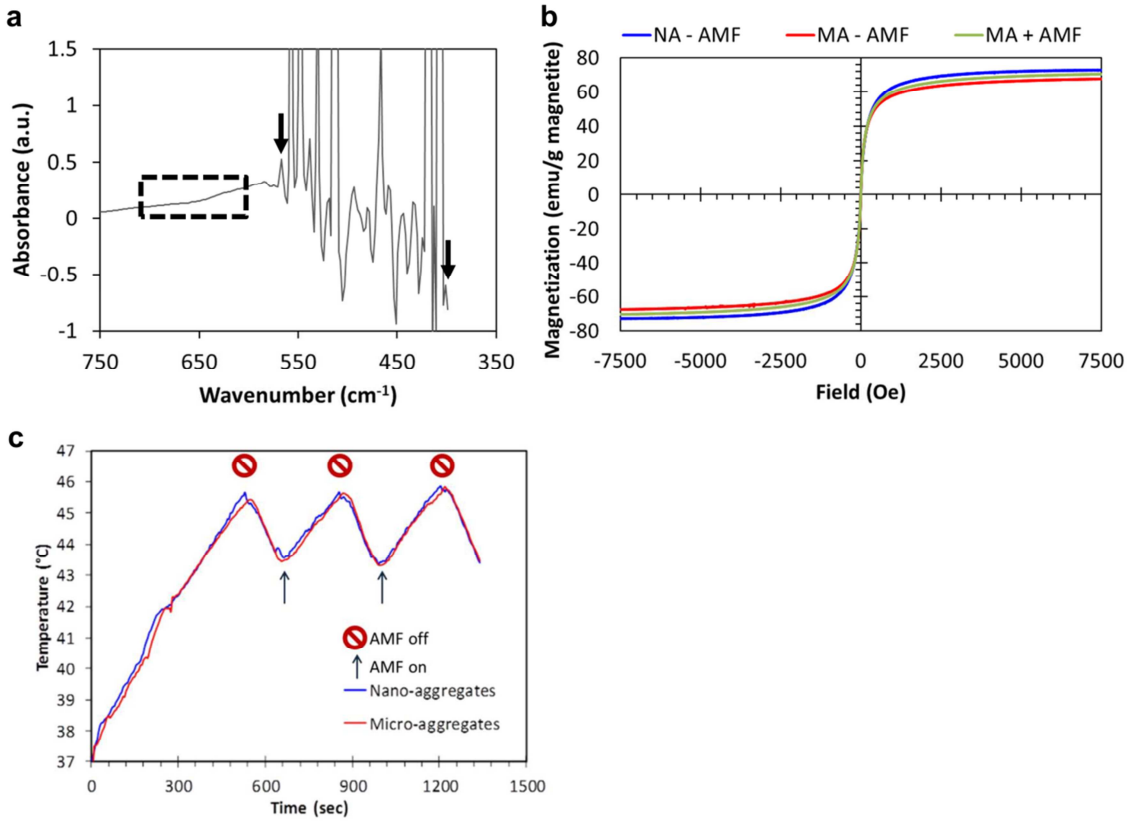

Figure 2.2 Characterization of SPIO aggregates. **(a)** FT-IR spectrum of SPIO nanoparticles. Presence of characteristic magnetite bands at 570 cm^{-1} and 400 cm^{-1} (arrow) and absence of maghemite bands at 700 cm^{-1} and 630-660 cm^{-1} (box) indicate that the primary form of iron oxide is magnetite[1]. **(b)** Magnetization curves of nano aggregates (NA) and micro aggregates (MA) recorded on a vibrating sample magnetometer. The curve was normalized to the weight of magnetite added to obtain saturation magnetization per gram of magnetite. The sigmoidal curve is characteristic of superparamagnetic substances. The data shows that the saturation magnetization of nano and micro aggregates was similar (~70 emu/g magnetite). Additionally, exposure of micro aggregates to AMF did not alter their saturation magnetization or superparamagnetic properties. **(c)** Heating rates of nano and micro aggregates dispersed in an alternating magnetic field of 6 kA/m and operating at a frequency of 386 kHz. The initial temperature was equilibrated to 37°C, and temperature of the SPIO NP dispersion was sampled at 5 second intervals using a fluoroptic probe following the application of magnetic field. The magnetic field was stopped when the temperature reached about 45.5°C and restarted at 43.5°C. The graph shows the similarity in the heating profiles of nano and micro aggregates during the three AMF on/off cycles.

Nano aggregate-mediated hyperthermia resulted in a time-dependent decrease in cell survival. The lactate dehydrogenase (LDH) release was not significantly increased at two hours following MH treatment (Figure 2.3a); however, less than 10% of the treated cells survived at 24 hours (Figure 2.3b). Similar inefficient early LDH release and higher cell death at 24 hours was also observed in cells subjected to conventional hyperthermia or MH using a commercial well-dispersed 100-nm SPIO nanoparticle formulation (Nanomag®). This was not surprising, given that hyperthermia has been shown to induce apoptotic cell death, a slow process that takes several hours [164-166]. Both Nanomag®-mediated MH and conventional hyperthermia resulted in PARP1 cleavage (Figure 2.4), confirming the induction of apoptosis with these treatments. However, nano aggregate induced MH resulted in a decrease in the levels of intact 116 kDa PARP1 protein (Figure 2.4, Figure 2.5a), without a concomitant increase in levels of the cleaved PARP1 fragment (89 kDa) (Figure 2.4, Figure 2.5b), a marker for caspase-dependent apoptosis [167,168]. The lysosomal enzyme cathepsin, which is released after lysosomal rupture such as during autophagy [169], can cleave PARP1 into fragments of different sizes (44, 55, 62 and 74 kDa) [170], and thereby decrease PARP1 levels without a detectable increase in the 89 kDa fragment. Expression of LC3B-II (Figure 2.4), an autophagy marker [171], further points to autophagy as the primary cell kill mechanism with nano aggregate-mediated MH.

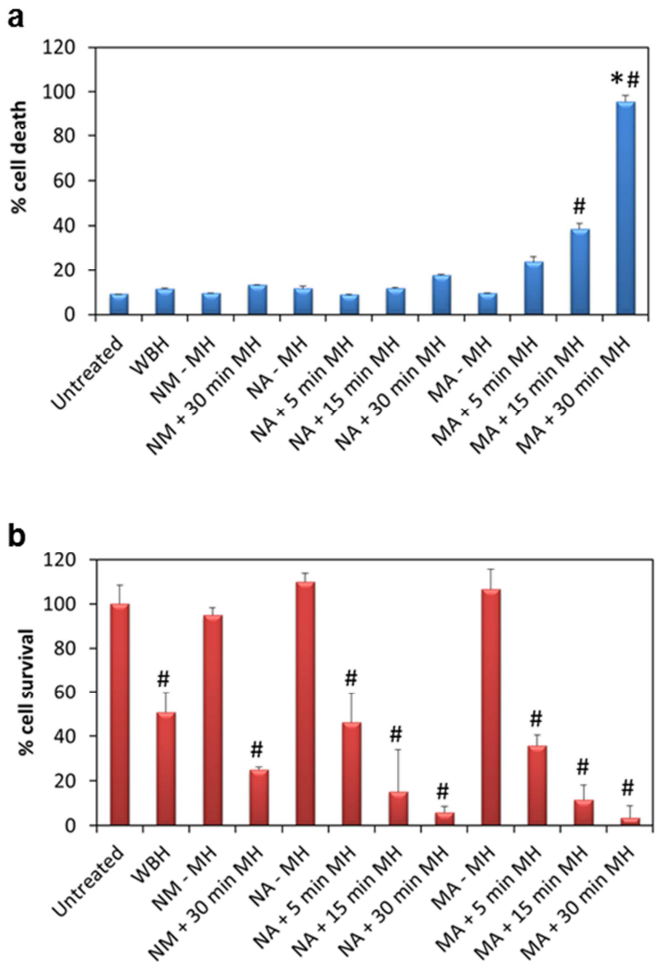

Figure 2.3 Effect of SPIO nanoparticle aggregate size on the mechanism of cell kill by MH. Effect of nano aggregate (NA), micro aggregate (MA) and commercial nanoparticle (Nanomag®; NM)-mediated MH and conventional hyperthermia (WBH) on **(a)** cell death quantified by LDH release from the cells 2 hours after treatment and **(b)** cell survival 24 hours after treatment measured by MTS assay. A549 cell suspension containing different SPIO formulations were subjected to 5 min, 15 min or 30 min of AMF after the suspension temperature reached 43°C. Untreated cells or cells incubated with SPIO formulations without AMF exposure (-MH) were used as controls. Conventional hyperthermia involved maintaining cells at 46°C for 30 min on a water bath. Data shown is mean ± S.D., n = 3. * $P < 0.00001$ vs. cells exposed to 30 min heating with different treatment; # $P < 0.001$ vs. corresponding unheated control.

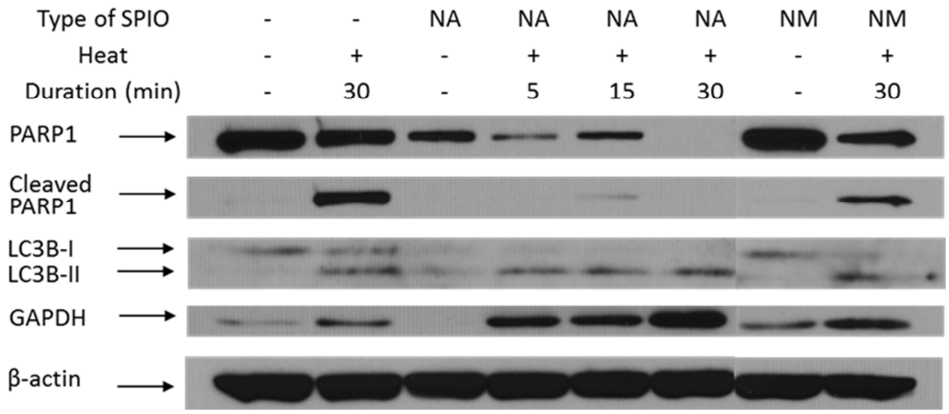

Figure 2.4 Western blotting. Western blotting analysis of expression of PARP1 (116 kDa), cleaved PARP1 (89 kDa), LC3B-I (16 kDa), LC3B-II (14 kDa), GAPDH (37 kDa) and beta actin (44 kDa) 24 hours after MH treatment as in Figure 2.3a and 2.3b.

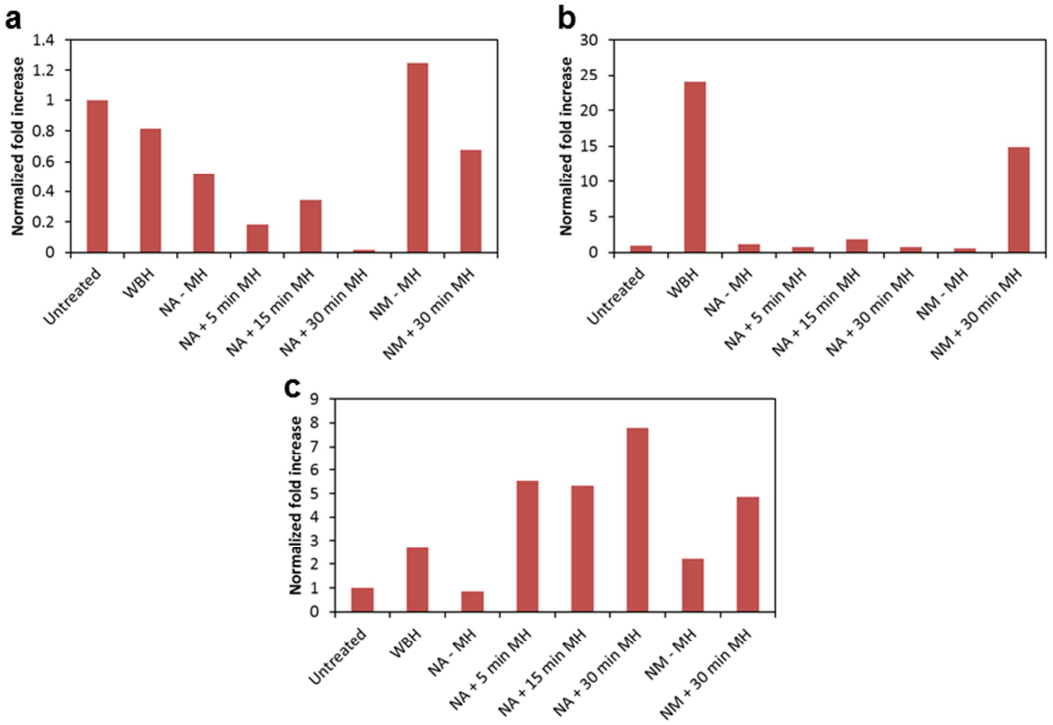

Figure 2.5 Quantitation of the western blot (Figure 2.4). Band intensity of **(a)** PARP1, **(b)** cleaved PARP1 and **(c)** GAPDH after different treatments. The band intensity was normalized to the levels of beta actin in the cell lysate. NA = nano aggregates, MA = micro aggregates, NM = Nanomag® and WBH = conventional hyperthermia.

Autophagy is a form of programmed cell death mediated by the lysosomal machinery and intracellular membrane rearrangement, leading to massive degradation of cellular components [172]. Autophagy involves sequesteration of cytoplasmic components in a membrane vesicle called autophagosome, which then fuses with the lysosome to form an autolysosome. Proteases within the autolysosome degrade the sequestered cytoplasmic components. Oxidative stress has been shown to play an important role in inducing autophagy [173-175]. We determined the level of reactive oxygen species (ROS) produced by cells subjected to different treatments. The ROS levels remained unchanged after conventional hyperthermia and Nanomag®-induced MH. However, nano aggregates resulted in elevated cellular ROS levels (Figure 2.6). One of the effectors of oxidative stress is GAPDH [176], which causes an elevation of cellular glycolysis and drives autophagy [177]. MH using SPIO nanoparticle formulations resulted in elevated GAPDH protein levels, and this increase was greatest in cells subjected to nano aggregate-mediated MH (Figure 2.4, Figure 2.5c).

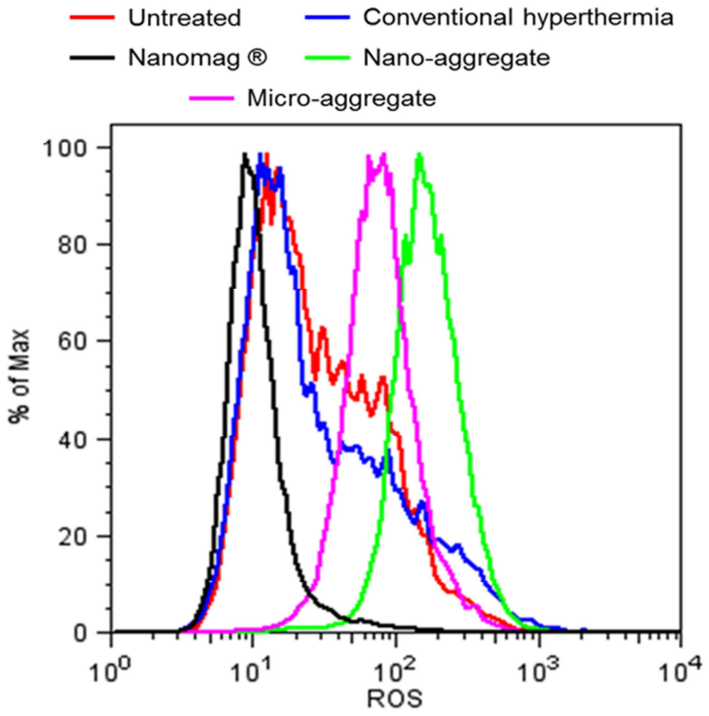

Figure 2.6 ROS generation after different treatments. CM-H_2DCFDA was added to A549 cells immediately before exposure to alternating magnetic field and after 2 hours, the cells were analyzed by flow cytometry to determine ROS levels. The graph shows a representative ROS profile of cells after treatment. Neither conventional hyperthermia nor Nanomag® mediated MH resulted in the elevation of ROS production relative to that in untreated cells. However, both nano and micro aggregate mediated MH led to an elevation of ROS levels in the cells.

With micro aggregates, we observed significant LDH release from treated cells at 2 hours following MH treatment (~90% cell kill with 30 min of MH, Fig. 1a). Acute LDH release with micro aggregates indicated that the cell membrane was compromised rather quickly, pointing to a necrotic cell death mechanism [178]. We hypothesized that rotational/oscillatory movement of micro aggregates in alternating magnetic field (AMF)

caused acute mechanical cell damage and LDH release. Such a mechanism would be temperature-independent, since the particle movement is dependent only on the strength of the magnetic field. To probe for this possibility, cells incubated with SPIO aggregates were subjected to AMF at a low temperature (<5°C). Acute membrane damage induced by this treatment was determined by monitoring the 'instantaneous' propidium iodide (PI) uptake by treated cells [162]. Only the cells treated with micro aggregates demonstrated instantaneous PI uptake in the absence of temperature elevation (Figure 2.7a). Neither nano aggregates (Figure 2.7b) nor Nanomag® (Figure 2.8) was effective in inducing instantaneous PI uptake.

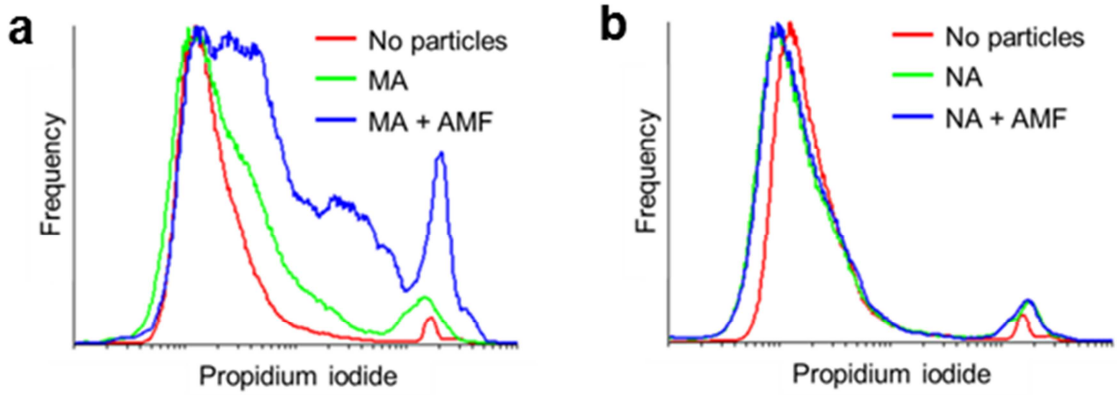

Figure 2.7 Instantaneous PI uptake. Flow cytometric analysis of instantaneous PI uptake by cells incubated with **(a)** micro aggregates and **(b)** nano aggregates and subjected to AMF under low temperature (<5°C). PI was added to the cell suspension immediately prior to AMF exposure (30 min), washed after treatment to eliminate the excess PI and analyzed by flow cytometry. Data shown is representative PI profile of the different treatments (n = 3). Micro aggregates showed an increase in PI positive population after AMF exposure.

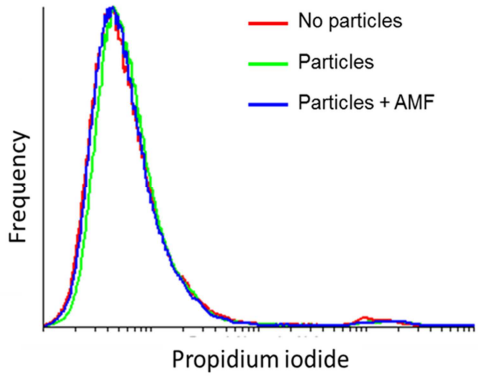

Figure 2.8 Instantaneous PI uptake. Flow cytometric analysis of instantaneous PI uptake by cells incubated with Nanomag® and subjected to AMF under low temperature (<5°C). PI was added to the cell suspension immediately prior to AMF exposure (30 min), washed after treatment to eliminate the excess PI and analyzed by flow cytometry. Data shown is representative PI profile of the different treatments (n = 3). No detectable difference in the PI profile was observed between the different treatments.

Additionally, while conventional hyperthermia and Nanomag® or nano aggregate-induced MH caused an elevation of heat shock protein 70 (Hsp70), micro aggregate-mediated MH showed no such increase (Figure 2.9a and 2.9b). This further verified the role of temperature elevation as the primary mechanism of cell death with sub-micron aggregates and a temperature-independent cell death mechanism with micro aggregates. Induction of Hsp70 expression also suggests the possibility of triggering Hsp70-mediated resistance to thermotherapy [179,180].

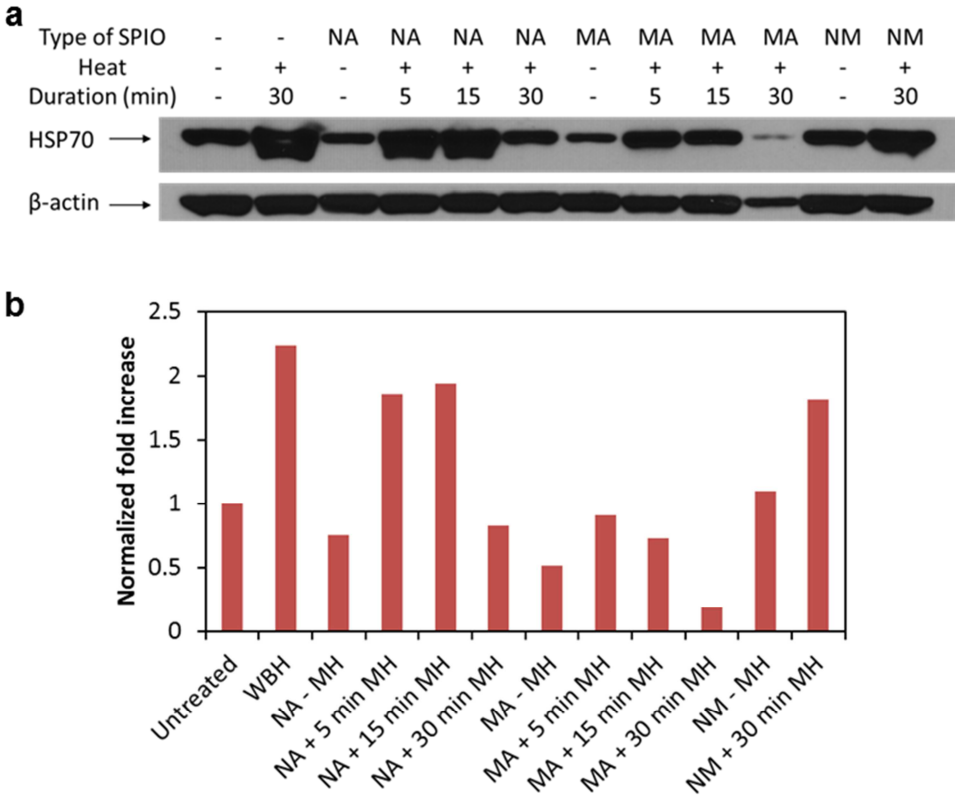

Figure 2.9 Western blotting of HSP70 and beta actin. **(a)** Western blotting analysis of expression of HSP70 (70 kDa) and beta actin (44 kDa), 24 hours after MH treatment (as in Figure 2.3a and 2.3b). **(b)** Quantitation of HSP70 levels from (A) normalized to beta actin. While conventional hyperthermia and nano aggregate or nanomag® mediated MH led to an increase in HSP70 expression in the cells, micro aggregate mediated MH did not elevate the protein level relative to that in untreated cells.

2.3.2. Micro aggregates cause membrane damage through direct membrane contact

To further study the mechanism of membrane damage induced by micro aggregates, we determined the cellular distribution of the aggregates. Coumarin-6 (a

lipophilic green fluorescent dye) was incorporated in SPIO nanoparticles to aid in visualization of particles [181]. Confocal microscopic images showed the presence of aggregates on cell surfaces and in the lysosomes (Figure 2.10a). In the absence of AMF, incubation with micro aggregates did not affect the cell membrane integrity (Figure 2.8b). Exposure to AMF caused blebbing of the membrane at points where the aggregates contacted the cell membrane (Figure 2.10b). The membrane blebs were large and characteristic of necrotic blebs [182]. Additionally, the blebbed cells also stained positive for PI, indicating the loss of membrane integrity in these cells (Figure 2.11).

We postulated that micro aggregates caused cell membrane damage through physical motion of the aggregates that are bound to cell membrane. Alternatively, cell membrane damage could also be the result of intense local heat generation by the aggregates [183,184]. To test these possibilities, solid iron oxide particles (iron oxide microparticles) were synthesized with similar dimensions as micro aggregates (Figure 2.12). These particles had ferromagnetic properties, characterized by a hysteresis loop in the induced field as a function of applied field and by a larger remanence than SPIO nanoparticles (Figure 2.13). Concentration of iron oxide microparticles used in cell culture experiments was adjusted to achieve an *in vitro* heating profile similar to that with micro aggregates. Despite similar temperature elevation as micro aggregates, iron oxide microparticles were ineffective in inducing tumor cell kill (7% vs 90% for micro aggregates) (Figure 2.14a).

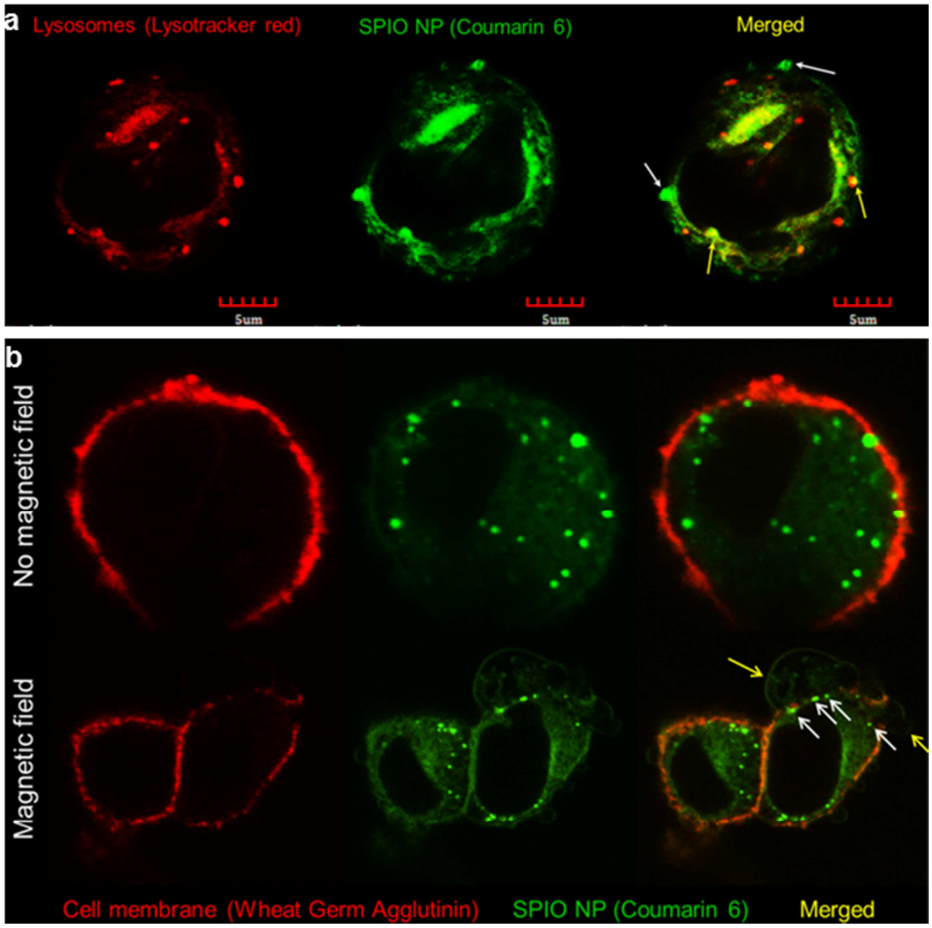

Figure 2.10 Micro aggregate mediated membrane damage through direct contact. **(a)** Confocal microscopic images of cells incubated with coumarin-6 labeled SPIO micro aggregates (green). Lysosomes were stained with Lysotracker red®. Representative images showing the location of lysosomes (left), micro aggregates (center) and their colocalization (right) are shown. The merged image shows aggregates on the surface of cells (white arrows) and in lysosomes (yellow arrows). Scale bar, 5µm. **(b)** Confocal microscopy of cells incubated with coumarin-6 labeled SPIO micro aggregates before (top) and after (bottom) AMF exposure at low temperature (<5°C). The cell membrane was labeled with Texas red® labeled wheat germ agglutinin (left). The coumarin-6 labeled SPIO micro aggregates (center) were present both on the cell membrane and inside the cells. The cell membrane was intact in cells incubated with particles in the absence of AMF (top right), indicated by the smooth cell membrane staining. Exposure to AMF resulted in cell membrane blebbing (bottom right, yellow arrows) at the sites where the aggregates contacted the cell membrane (white arrows).

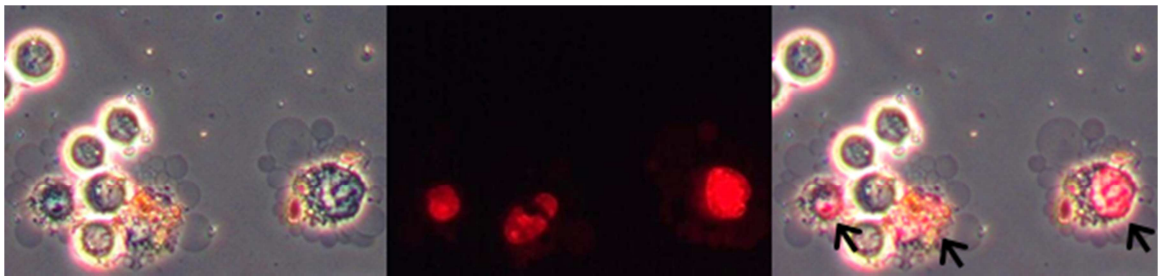

Figure 2.11 Micro aggregate mediated membrane damage through direct contact (PI uptake). Phase contrast (left) and fluorescence microscopic image (middle) of cells incubated with SPIO micro aggregates and PI and exposed to low temperature AMF. The merged image (right) shows PI positive, extensively blebbed cells (black arrows) and the healthy cells devoid of blebbing or PI staining.

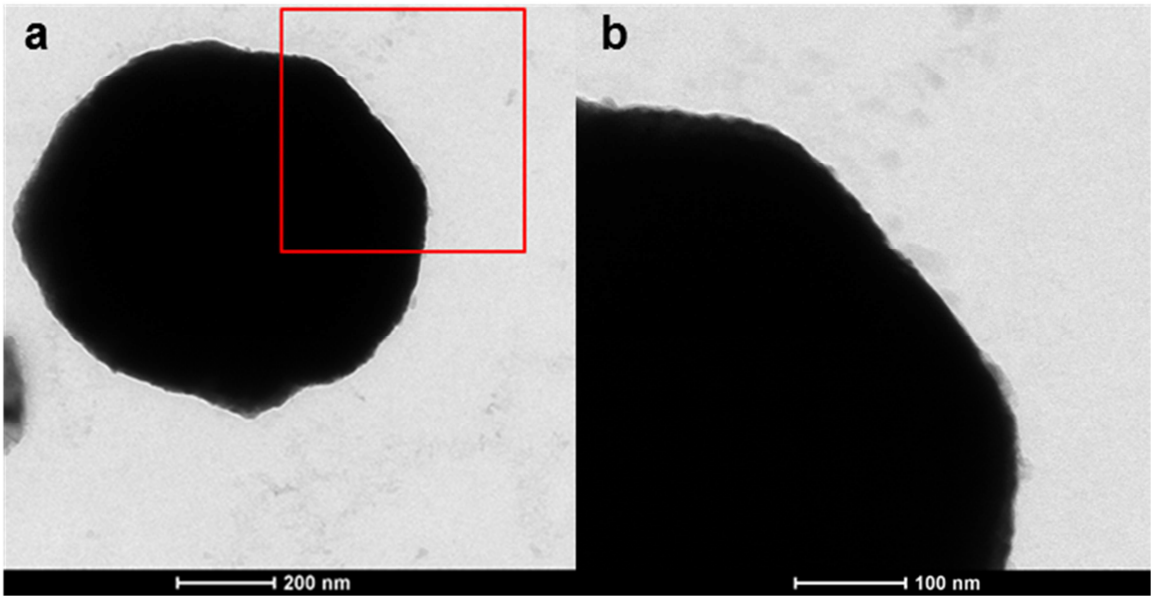

Figure 2.12 Characterization and in vitro effects of SPIO microparticles (TEM image). **(a)** Representative TEM image of iron oxide microparticles. The microparticles were spherical and about 1 µm in size. Scale bar, 200 nm. **(b)** The boxed area of (A) is magnified to show that unlike the micro aggregates (Figure 2.1), the microparticles were solid and not composed of smaller iron oxide cores. Scale bar, 100 nm.

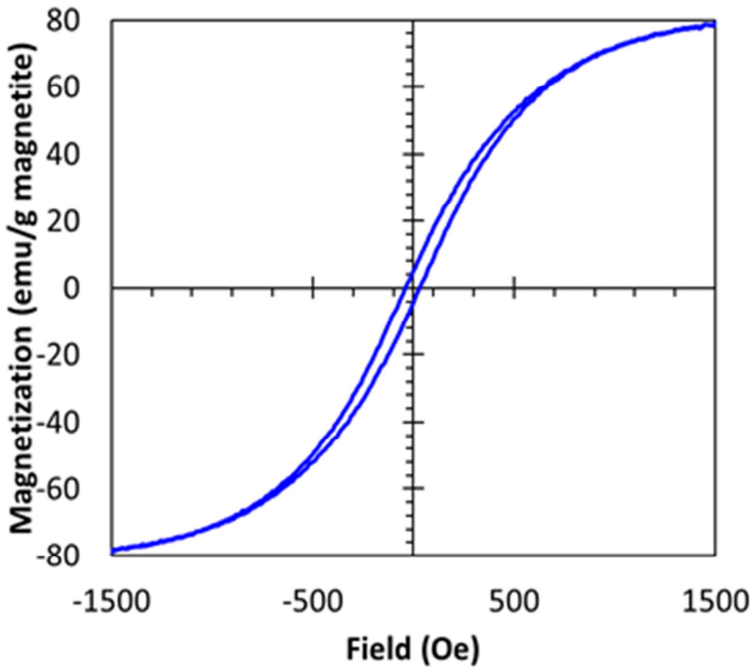

Figure 2.13 Characterization and in vitro effects of SPIO microparticles (Magnetization curve). Magnetization curve of iron oxide normalized to the weight of magnetite added to obtain saturation magnetization per gram of magnetite. The open hysteresis loop with higher remanence (6.08 emu/g magnetite) than the nano and micro aggregates (1.64 and 1.44 emu/g of magnetite, respectively) verified that the iron oxide microparticles were not superparamagnetic in nature and generated heat predominantly by hysteresis heating rather than by relaxation phenomena when placed in an AMF.

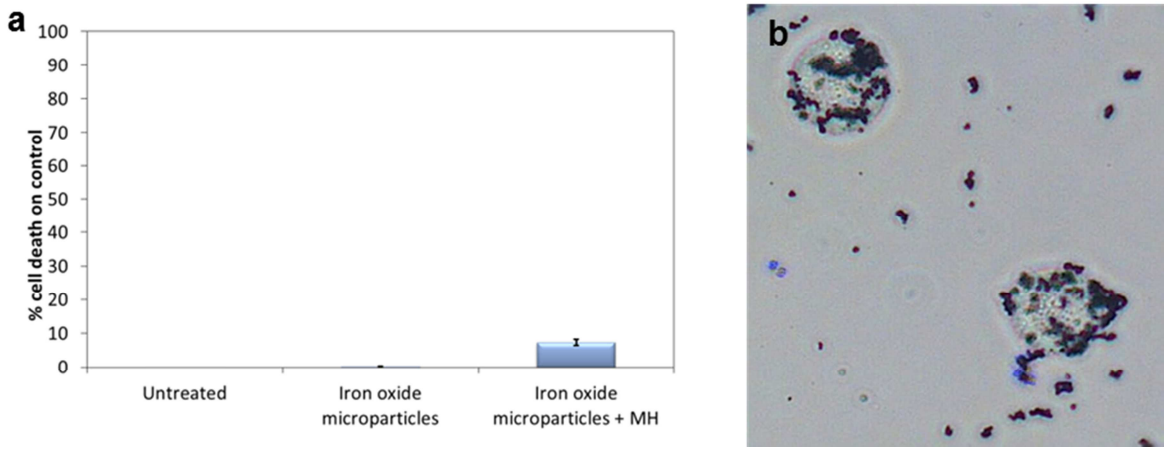

Figure 2.14 Characterization and in vitro effects of SPIO microparticles (Cell death). **(a)** Effect of iron oxide microparticle mediated MH on cell death quantified by LDH release from the cells 2 hours after treatment. A549 cell suspension containing iron oxide microparticles was subjected to 30 min of MH. Untreated cells or cells incubated with microparticles without AMF exposure were used as controls. Though MH using iron oxide microparticles resulted in higher cell death than control, the increase was almost negligible compared to SPIO micro aggregate mediated MH (7% vs 90% respectively). **(b)** Microscopic image of iron oxide microparticles (black dots) associated with A549 cells. 400X magnification.

Due to their ferromagnetic nature, iron oxide microparticles do not rotate in AMF but instead undergo hysteresis heating [67]. Because their heating rates and sizes were similar to that of micro aggregates, the intensity of local heat produced is also expected to be similar. However, the ineffectiveness of these particles in killing cells despite their association with the cells (Figure 2.14b), suggests that intense local heating is not the likely mechanism of cell membrane damage with micro aggregates. Also, as noted above, micro aggregates induced cell membrane damage even when the cell suspension was maintained below 5°C; the cold medium should act as an effective heat sink, thereby

minimizing any local temperature elevation. Our results thus suggest that micro aggregates induce acute cell kill through mechanical disruption of cell membrane. Theoretical estimations show that while the energy requirements for creating a membrane pore are not easily overcome by 100 nm magnetic particles, the energetic restriction becomes less stringent with increasing particle size [185]. Thus, it is much more favorable for a rotating or oscillating micro aggregate to disrupt the cell membrane integrity than a nano aggregate. Quite recently, a similar membrane damaging effect (termed 'magnetoporation' and 'magnetolysis') was described for polymer-coated carbon nanotubes that were subjected to a rotating magnetic field [162]. Interestingly, the polymer coated multi-walled carbon nanotubes formed aggregates (or 'bundles') that were in the same size range as micro aggregates used here.

To further determine the possibility of cell membrane damage induced by the motion of micro aggregates, we used the procedure described by Liu et al. [162], where cells incubated with nano or micro aggregates and PI were subjected to a rotating magnetic field. Only 3 min of rotating magnetic field exposure with micro aggregates resulted in a dramatic increase in the proportion of PI positive cells (Figure 2.15). This further substantiates the possibility that micro aggregates in motion can alter cell membrane integrity.

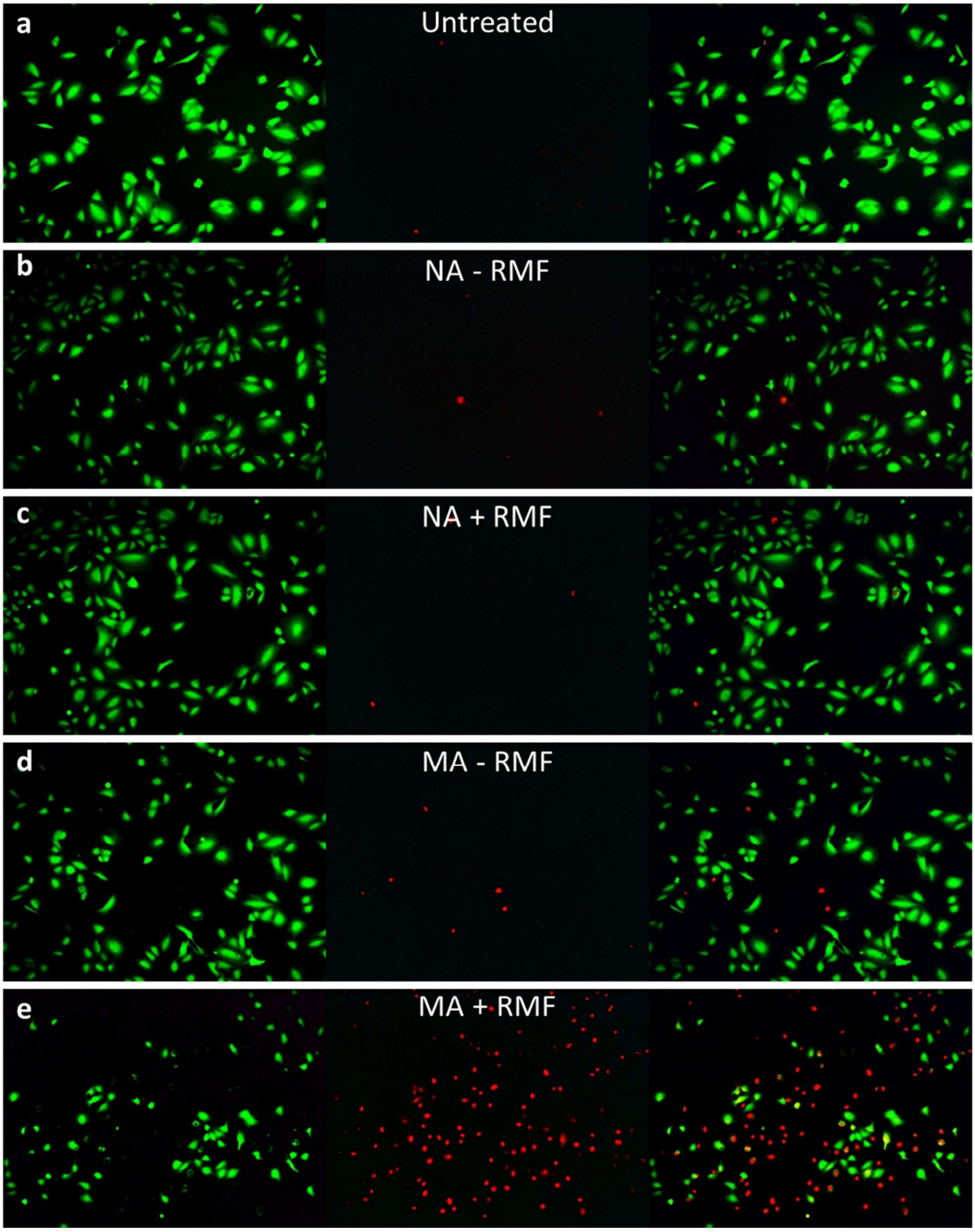
a
Untreated
b
NA - RMF
c
NA + RMF
d
MA - RMF
e
MA + RMF

Figure 2.15 Effect of rotating magnetic field (RMF) on instantaneous cell membrane damage and PI uptake. A549 cells were incubated with PI and **(a)** phosphate buffered saline, **(b)** nano aggregates without RMF, **(c)** nano aggregates subjected to 3 min of RMF, **(d)** micro aggregates without RMF exposure and **(e)** micro aggregates exposed to RMF for 3 minutes. Immediately after RMF exposure, the cells were washed with phosphate buffered saline, 0.1 μM calcein AM added to the cell media and imaged under fluorescent microscope. Calcein AM labels the live cells green (left) and PI labels the nucleus of the dead cells red (center). The merged image (right) shows that unlike the other treatments, micro aggregates subjected to a RMF was successful in disrupting the cell membrane integrity in a large number of cells.

2.3.3. Micro aggregate induced magnetic hyperthermia inhibits tumor growth in vivo

To determine whether differences in aggregate size affects *in vivo* therapeutic efficacy as well, we evaluated the anticancer efficacy of micro and nano aggregates in mice bearing subcutaneous A549 tumor xenografts. Animals receiving the aggregates without exposure to AMF served as control groups. Tumor temperatures were monitored using infrared thermometry and the magnetic field conditions were optimized to ensure that the tumor temperature did not increase beyond 46°C. The average tumor temperature was 43.5°C in both the micro and nano aggregate groups, with the highest temperature reached being 45.5°C and 45.7°C, respectively (Figure 2.16). Nano aggregate-mediated MH resulted in a moderate decrease in tumor growth rate ($p = 0.085$) relative to that in animals that received nano aggregates but were not exposed to AMF. Micro aggregate-mediated MH showed significant effectiveness ($p < 0.001$), with near complete inhibition

of tumor growth (Figure 2.17). The results from the bioluminescence imaging reinforced this finding, with micro aggregate-mediated MH being highly effective in decreasing the tumor-associated luminescence (Figure 2.18). Histological analysis of the tumor sections revealed that micro aggregate-mediated MH resulted in the formation of "hollow" tumors, with a large central acellular core and a small outer rim of cells (Figure 2.19, Figure 2.20). Immediately after exposure to AMF, cells surrounding the SPIO aggregates (confirmed by Prussian blue staining) were characterized by altered morphology, decreased cell volume, and increased nuclear density (Figure 2.21b,d). Tumor tissue sections from the control group (injected with micro aggregates but not exposed to AMF) showed no such changes in the cellular morphology around the SPIO aggregates (Figure 2.21a,c). Because all the experimental parameters (dose of SPIO, duration of AMF exposure and the temperature elevation) were similar for both nano and micro aggregates, the enhanced effectiveness of micro aggregates is likely due to temperature-independent membrane damage.

These *in vivo* results thus confirm that larger aggregates are more effective in killing tumor cells than smaller sub-micron size aggregates. Intravenous delivery of micro aggregates is likely not practical due to concerns of embolism [110,186] and because the particle size is too large to take advantage of the enhanced permeation and retention effect [146]. However, the particle size range of micro aggregates is particularly suitable for inhalation delivery [109] to treat lung tumors [187,188]. Alternately, an *in situ* aggregation approach can also be envisioned, where sub-micron size particles injected intravenously aggregate into micron size aggregates in the tumor microenvironment.

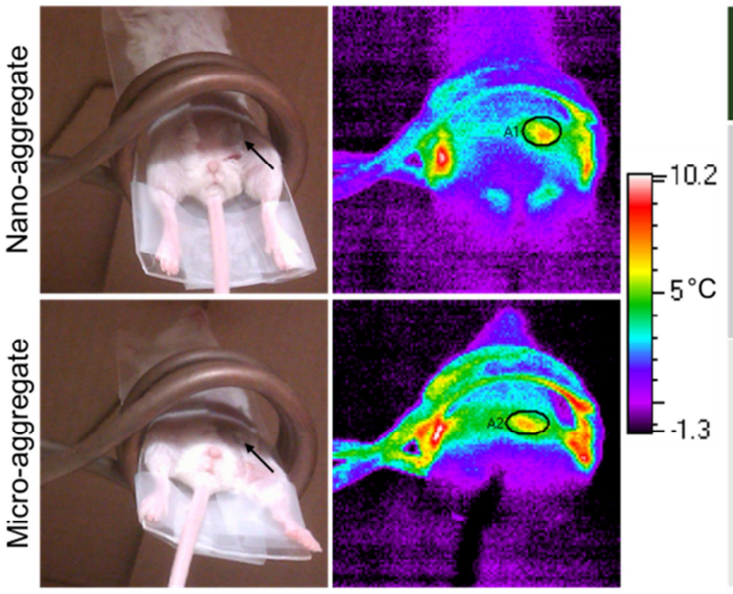

	NA	MA
Calculated temperature change [Average; (maximum)]	6.5°C; (8.7°C)	6.5°C; (8.5°C)
Actual tumor temperature [Average; (maximum)]	43.5°C; (45.7°C)	43.5°C; (45.5°C)

Figure 2.16 Tumor temperature monitoring using infrared camera. Representative photograph of a mouse placed in the radiofrequency coil (left) during nano aggregate (NA) (top) or micro aggregate (MA) (bottom) mediated MH. The black arrow indicates the location of the subcutaneous tumor xenograft. The temperature elevation during MH was measured using infrared thermometry. Infrared thermometric images of the temperature difference before and at the end of MH treatment is shown (right). The tumor temperature (black oval) was calculated for both nano and micro aggregate mediated MH (table). Note that the elevated temperature at the edges of the coil is due to the heating of the coil during AMF exposure.

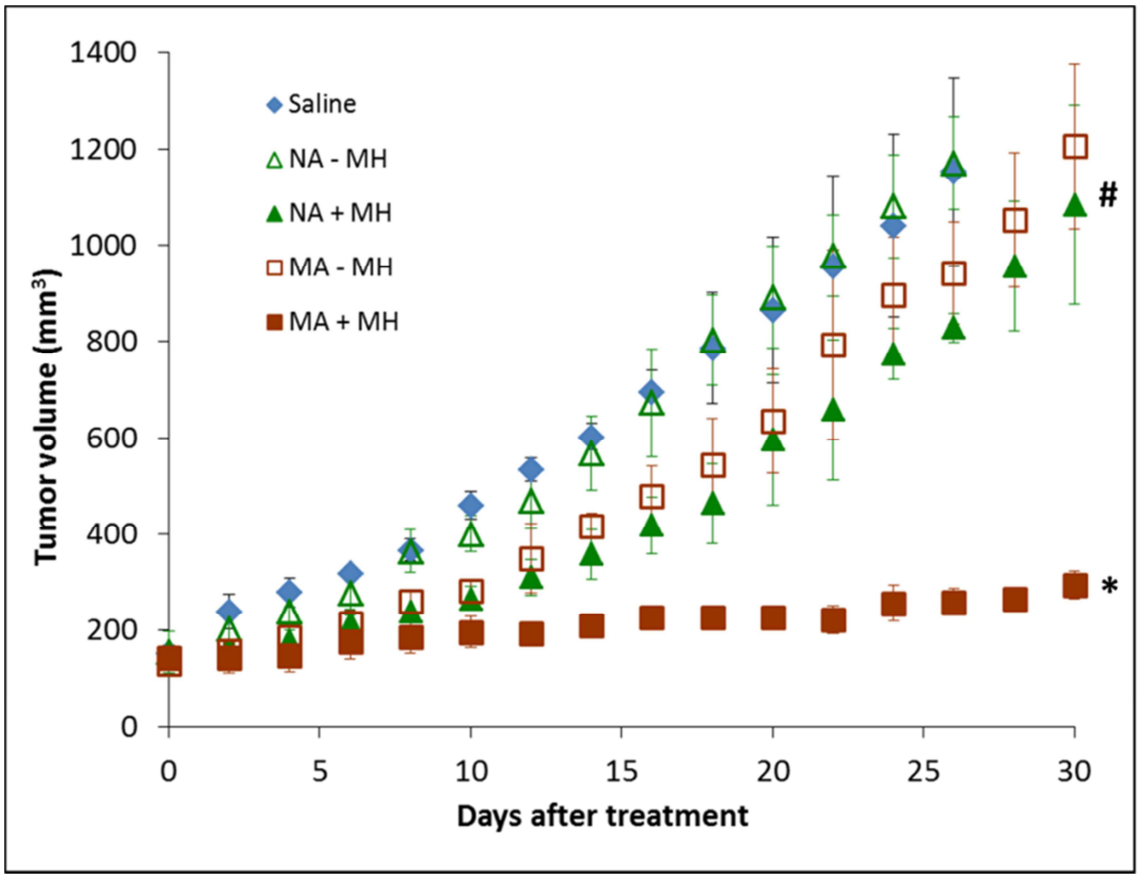

Figure 2.17 Effect of SPIO aggregate mediated MH on in vivo tumor growth. The tumor growth was monitored every alternate day after MH treatment. The graph shows the tumor growth with different treatments as a function of time after treatment. Data shown is mean ± S.D., n = 6. * $P < 0.001$ and # $P < 0.1$ vs. control.

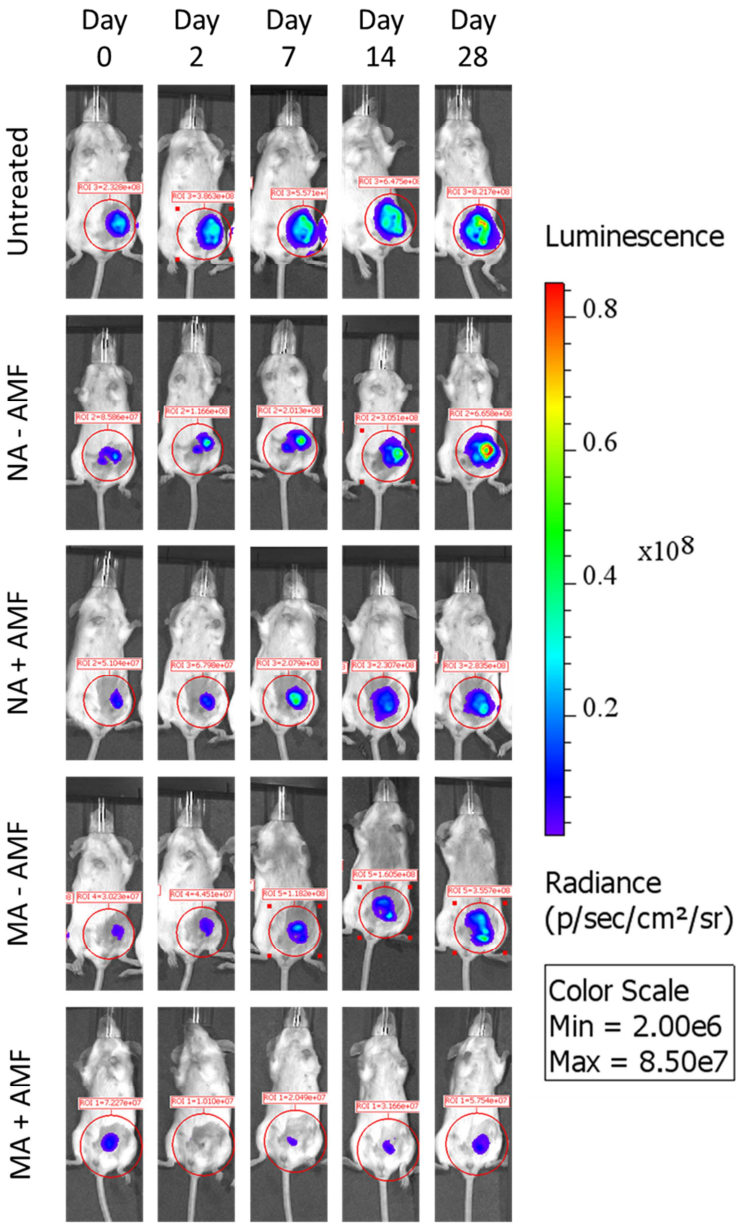

Figure 2.18 Bioluminescence imaging of mice. Mice were injected with **(a)** saline, **(b, c)** SPIO nano aggregates and **(d, e)** SPIO micro aggregates intratumorally when the tumor volumes reached 150 mm^3. After 24 hours, the **(c)** nano aggregate and **(e)** micro aggregate treated animals were subjected to magnetic hyperthermia for 30 minutes. Tumor bioluminescence was measured before MH treatment (Day 0) and on days 2, 7, 14, 21 and 28. The images are from an animal in each group monitored over 4 weeks after treatment. The bioluminescence intensity of all images are scaled as shown in the right.

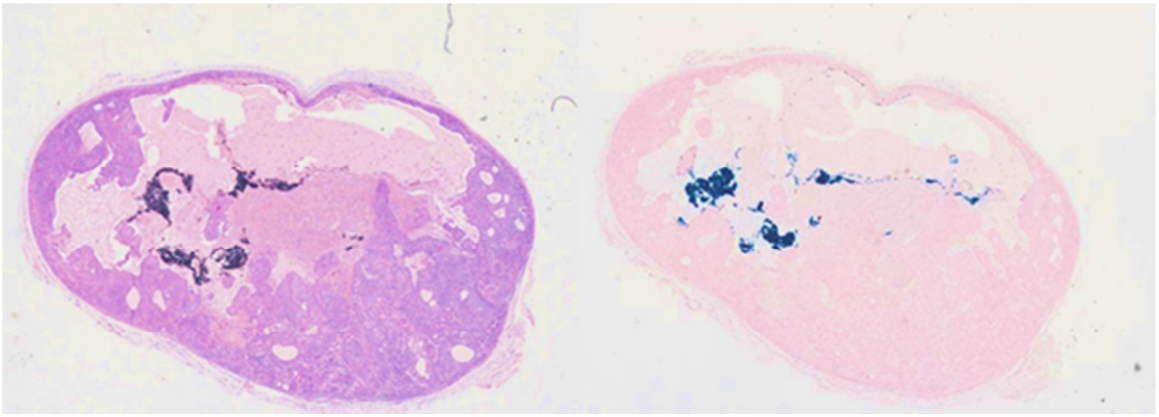

Figure 2.19 Histology of tumors exposed to MH treatment (micro aggregate). Hematoxylin and eosin (H&E) staining (left) of a tumor after 30 days of micro aggregate mediated MH. The tumor is partially acellular due to the MH treatment. Prussian blue staining (right) performed on the subsequent section (5µm apart) shows the presence of SPIO particles at the necrotic margins of the tumor.

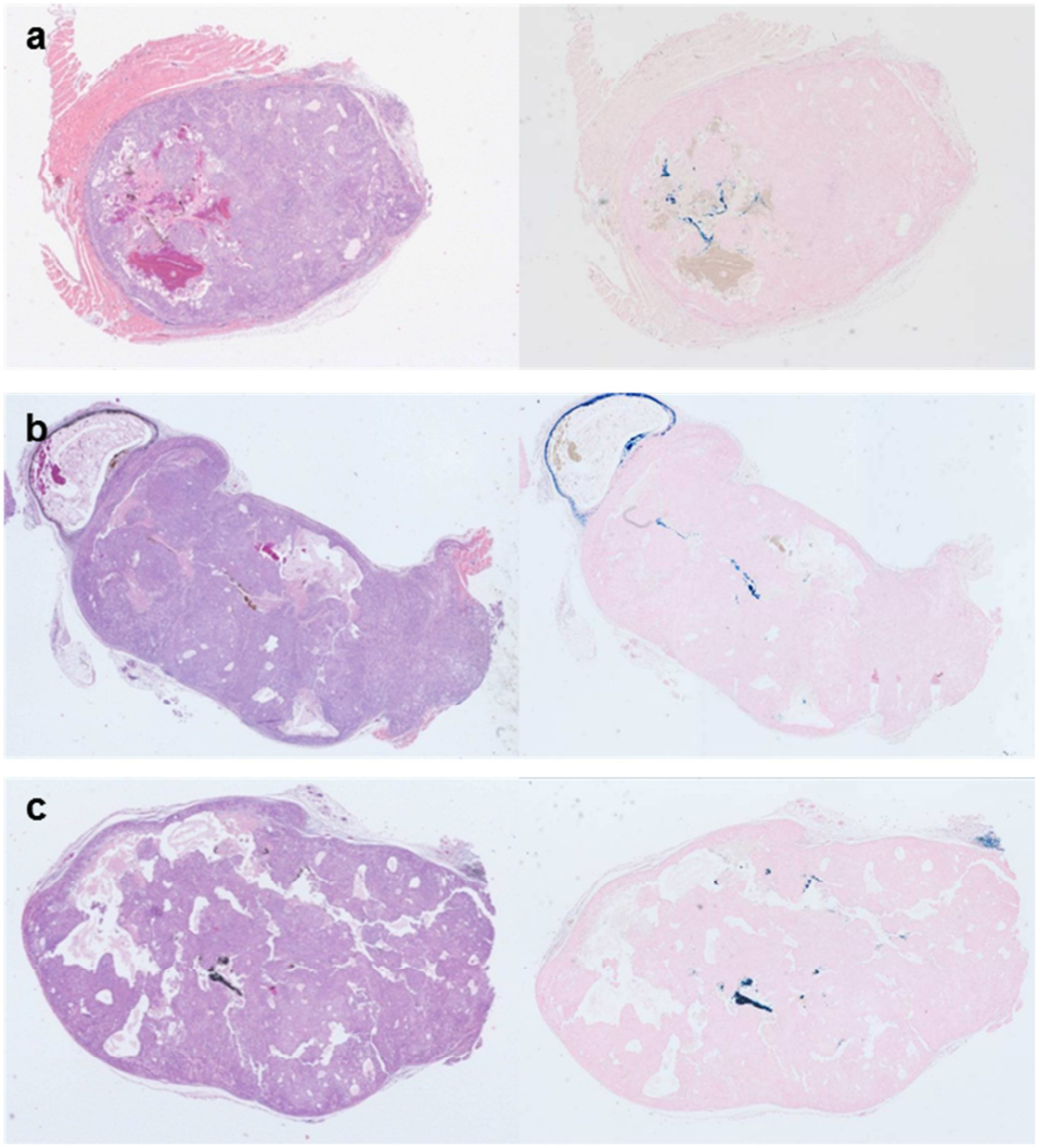

Figure 2.20 Histology of tumors exposed to MH treatment (controls). Hematoxylin and eosin staining (left) and prussian blue staining (right) performed on the subsequent section (5µm apart) of tumors collected at the end of the *in vivo* study. **(a)** nano aggregates without MH, **(b)** nano aggregates with MH and **(c)** micro aggregates without magnetic hyperthermia. All the tumors are highly cellular unlike the micro aggregate mediated MH treated tumors (Figure 2.16).

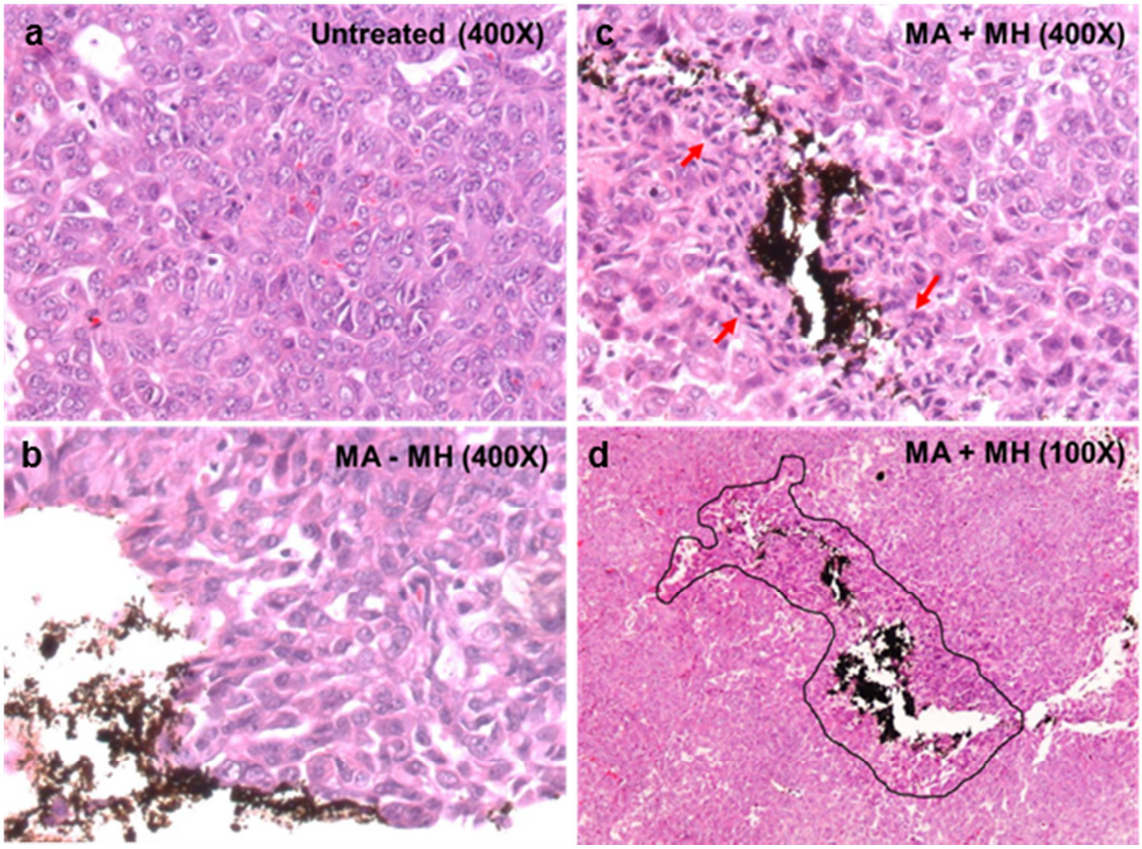

Figure 2.21 Histology of tumors exposed to MH treatment (cell damage). **(a)** H&E staining of a tumor section (400X magnification) from animals receiving no treatment. The tumor cells have a 'swollen' appearance with large lightly stained nucleus. **(b)** H&E staining (400X magnification) of a micro aggregate injected tumor that was not exposed to an AMF. The micro aggregates can be identified by their brown color. Cells adjacent to the particles have similar morphology as the untreated tumor (a). **(c)** H&E staining (400X magnification) of a tumor collected immediately after micro aggregate mediated MH. Cells around the particles have altered morphology characterized by cell shrinkage and denser nuclear stain. **(d)** Lower magnification (100X) of (c) showing a distinct region around the micro aggregates (black bordered area) where the cells have a different morphology compared to the rest of the tumor.

2.4. Conclusions

Inorganic nanoparticles have the propensity to aggregate when introduced into a biological milieu. Our studies showed that the particle size of aggregates affects the therapeutic performance of SPIO nanoparticles. Well-dispersed SPIO nanoparticles induce apoptosis, similar to that observed with conventional hyperthermia. Nanometer size aggregates, on the other hand, induce temperature-dependent autophagy through generation of ROS. Micron size aggregates caused rapid membrane damage and acute cell kill, likely due to physical motion of the aggregates in AMF. This novel mechanism of cell kill induced by micro aggregates translated into effective *in vivo* tumor growth inhibition. Overall this work highlights the potential for developing highly effective anticancer therapeutics through simple yet often overlooked modifications of delivery systems such as their state of aggregation.

Chapter 3

EFFECTIVE ELIMINATION OF CANCER STEM CELLS BY MAGNETIC HYPERTHERMIA

Tanmoy Sadhukha [a], *Lin Niu* [a], *Timothy Scott Wiedmann* [a] and *Jayanth Panyam* [a,b]

[a] Department of Pharmaceutics, University of Minnesota, Minneapolis, MN 55455

[b] Masonic Cancer Center, University of Minnesota, Minneapolis, MN 55455

Running Title: Magnetic Hyperthermia Effectively Eliminates Cancer Stem Cells

Keywords: Superparamagnetic iron oxide, Magnetic Hyperthermia, Cancer Stem Cells, Necrosis, Reactive Oxygen Species, Mammosphere, Clonogenicity, Tumorigenicity, Aldehyde Dehydrogenase

3.1. Introduction

A number of recent studies suggest that tumors consist of a minor population of stem-like cells (cancer stem cells; CSCs) that are capable of generating and maintaining a tumor in its entirety [189]. These cells have the capacity for asymmetric cell division, generating one identical daughter cell and another that is committed to a distinct differentiation pattern. The latter undergoes a series of divisions and differentiation steps that result in the generation of terminally differentiated cell populations. Cells in the intermediate states are referred to as progenitors, transit cells or transit amplifying cells [190]. All of these phenotypes, collectively termed tumor-initiating cells, have the potential to give rise to a complete tumor. CSCs are resistant to conventional chemotherapy and can initiate tumor recurrence following treatment [191]. CSCs possess several defense mechanisms including overexpression of efflux pumps that can eliminate cytotoxic drugs [192], increased expression of DNA-repair proteins that can counteract DNA damage [193], elevated anti-oxidant concentrations to defend against reactive oxygen species (ROS) [194], and low rate of cell division [195]. Tumors can become enriched in CSCs after conventional treatments [193,196], which could account for frequent tumor relapse observed in many cancers.

Hyperthermia, which utilizes elevated temperatures in the range of 41 – 46° C to kill tumor cells [36], has been shown to improve treatment response and survival when used in combination with radiotherapy, surgery and/or chemotherapy [46,197]. In mouse tumor models, addition of local hyperthermia significantly increased the sensitivity of CSCs to radiotherapy [198]. Magnetic hyperthermia is a related approach that utilizes

superparamagnetic iron oxide nanoparticles (SPIO NPs) placed in an alternating magnetic field to generate heat for a highly localized tumor cell kill [58]. Magnetic hyperthermia is currently in clinical trials in Europe for glioblastoma as well as prostate and pancreatic cancers [199]. While a number of previous studies have demonstrated the anticancer efficacy of magnetic hyperthermia [200-203], the effect of magnetic hyperthermia on CSCs has not been reported to date. Using various in vitro and in vivo assays, we evaluated the ability of SPIO NP-mediated magnetic hyperthermia to effectively eliminate CSCs.

3.2. Experimental Section

3.2.1. Materials

Ferrous chloride tetrahydrate, ferric chloride hexahydrate, myristic acid, Pluronic F127, ascorbic acid, potassium hydroxide, 1,10 phenanthroline and sodium acetate were purchased from Sigma (St. Louis, MO). Penicillin/streptomycin, fetal bovine serum, RPMI 1640, Dulbecco's phosphate buffered saline (DPBS), F-12K (Kaighn's modification), MEM, non-essential amino acids, sodium pyruvate and trypsin-EDTA solution were obtained from Invitrogen Corporation (Carlsbad, CA). Cytotox 96® non-radioactive cytotoxicity assay kit was purchased from Promega (Madison, WI).

3.2.2. Methods

3.2.2.1. Synthesis of water-dispersible SPIO NPs

A stable aqueous dispersion of SPIO NPs was prepared from iron chlorides as previously described [204]. In brief, 0.82 g of ferric chloride hexahydrate and 0.33 g of

ferrous chloride tetrahydrate were dissolved in 30 ml of degassed and nitrogen-purged water, and 3 ml of 5 M ammonium hydroxide was added drop-wise to this solution and stirred for 30 minutes. Iron oxide nanoparticles formed were washed three times with nitrogen-purged water (each wash followed by magnetic separation of nanoparticles), sonicated in a water bath sonicator for 2 min, and heated to 80°C. About 100 mg of myristic acid was added to the heated mixture and stirred for another 30 min. Particles were washed twice with acetone to remove excess myristic acid, followed by two additional washes with water to remove excess acetone. Myristic acid-coated particles were then suspended in 30 ml water, and 100 mg of pluronic F127 was added and the mixture was stirred overnight. The final dispersion was lyophilized (Labconco, FreeZone 4.5, Kansas City, MO) to obtain SPIO NPs. Every step of the synthesis was carefully conducted to minimize exposure to atmospheric oxygen.

3.2.2.2. Characterization of SPIO NPs

Dynamic light scattering was used to determine the hydrodynamic diameter of SPIO NPs. About 0.5 mg/ml of SPIO NPs dispersed deionized water was subjected to particle size analysis using a Delsa™ Nano C Particle Analyzer (Beckman, Brea, CA). Transmission electron microscopy (TEM) of SPIO NPs was performed using a JEOL JEM-1210 transmission electron microscope (Peabody, MA). A drop of an aqueous dispersion of SPIO NPs was placed on a Lacey carbon-coated copper grid (300 mesh, Ted Pella Inc. Redding, CA) and allowed to air-dry before imaging. Diameters of 100 different particles were measured from different TEM images using ImageJ software. The average diameter along the horizontal axis was determined as the mean Feret's diameter.

The mean crystallite size of SPIO NPs was calculated from their X-ray diffraction pattern. SPIO NPs were subjected to a Cu-Kα radiation (45 kV, 40 mA) in a wide-angle powder x-ray diffractometer (D5005, Siemens, Madison, WI). The instrument was operated in the step-scan mode in increments of 0.05° 2θ over an angular range of 10 to 100° 2θ with a dwell time of 1 second for each scan step. Data analysis was performed using OriginPro 8 software (OriginLab Corporation, Northampton, MA). Five highest peaks (at 30.1°, 35.5°, 43.1°, 57.1° and 62.7° 2θ) were fit using the pseudo-Voigt profile function, which is a linear combination of the Gaussian and Lorentzian components of the diffraction peaks. The Scherrer equation was utilized to determine the mean particle size of SPIO NPs [205].

Fourier-transformed infrared spectroscopy (FT-IR) of SPIO NPs was performed using Vertex 70 FT-IR spectrophotometer (Bruker Optics Inc., Billerica, MA). About 5 mg of SPIO NPs were added to the FT-IR stage and scanned from 4000 cm^{-1} to 400 cm^{-1}. Each spectrum was obtained as an average of 16 interferograms at a resolution of 2 cm^{-1} and analyzed using OPUS software (Bruker Optics Inc., Billerica, MA). Magnetic properties were determined using a vibrating sample magnetometer (Micromod Model 3900, Princeton, NJ) operating at room temperature. Accurately weighed samples of SPIO NPs was sprinkled on a lightly greased silicon wafer and their magnetization curves were recorded in magnetic fields ranging from -1 T to 1 T, at increments of 0.002 T. Saturation magnetization per gram of magnetite was calculated from the magnetization curves normalized to the weight of magnetite added. The composition of SPIO NPs was estimated using 1,10 phenanthroline-based iron assay [160]. About 5 mg of SPIO NPs were

dissolved in 12 N hydrochloric acid and then diluted with distilled water to obtain a final acid concentration of 0.2 N. 10 mg/ml ascorbic acid, 22.4 mg/ml potassium hydroxide, 123 mg/ml sodium acetate and 1.2 mg/ml 1,10 phenanthroline were added to the SPIO NP solution in a volume ratio of 1:1:5:1:1. Absorbance at 490 nm was recorded using a microplate reader (ELx800 Absorbance Microplate Reader, Biotek, Winooski, VT) and the iron content was analyzed using ferric chloride (hexahydrate) solutions in 0.2 N hydrochloric acid as standards.

3.2.2.3. Magnetic heating rate

SPIO NPs were dispersed in 1 ml of Hank's F-12K medium or in 1 ml of molten 3% agarose, which was then allowed to form a gel in 10 mm X 75 mm disposable borosilicate glass cell culture tubes. Magnetic heating was performed using an induction heating system (1 kW Hotshot, Ameritherm Inc., Scottsville, NY) by placing the suspension at the center of a multiturn copper coil that generated the alternating magnetic field (nominal magnetic field strength of 6 kA/m and frequency of 386 kHz). The temperature change was measured using a fluoroptic® probe (Lumasense Technologies, Santa Clara, CA). Samples were thermally equilibrated to 37°C before exposure to the field.

3.2.2.4. Cell culture studies

A549 (human lung adenocarcinoma) and MDA-MB-231 (human mammary adenocarcinoma) cells were used in the study. A549 cells were propagated using F-12K medium supplemented with 10% fetal bovine serum (FBS) and 1% antibiotic solution.

MDA-MB-231 cells were grown in MEM supplemented with 10% FBS, 1% non-essential amino acids, 1% sodium pyruvate and 1% antibiotic solution. Both cell lines were maintained at 37°C and in 5% carbon dioxide.

3.2.2.5. Effect of magnetic hyperthermia on CSCs

3.2.2.5.1. Side population determination

Following magnetic hyperthermia, A549 cells were centrifuged and resuspended in prewarmed 1 ml DMEM with 2% FBS and 10 mM HEPES. Hoechst 33342 dye was added at a concentration of 5 μg/ml. In each treatment group, one sample was pretreated with 2 μM tariquidar, an inhibitor of Hoechst efflux. Cells were then incubated at 37°C for 90 min with occasional shaking. Cells were then washed with chilled HBSS with 2% FBS and 10 mM HEPES buffer and resuspended in chilled buffer. 7AAD was added to the sample tubes before flow cytometric analysis to gate for live cells. Flow analysis was carried out on a FACSDiva (BD Biosciences); Hoechst 33342 dye was excited at 357 nm and the fluorescence was measured at 402-446 nm (blue) and 650-670 nm (red) wavelengths [206].

3.2.2.5.2. Mammosphere assay

Following magnetic hyperthermia, MDA-MB-231 cells were washed and resuspended in cell culture medium. About 3000 live cells (counted by trypan blue exclusion) were plated in ultra-low adhesion 6-well plates with 2 ml mammosphere formulation (Dulbecco's modified Eagle's medium/F-12 medium supplemented with 10 ng/ml human-fibroblast growth factor, 20 ng/ml recombinant human epidermal growth

factor, 0.4% bovine serum albumin, 5 μg/ml insulin and 1% antibiotics). The number of mammospheres formed was counted under a light microscope 5 days after treatment [207].

3.2.2.5.3. Aldehyde dehydrogenase assay

Thirty million MDA-MB-231 cells were sorted based on their levels of aldehyde dehydrogenase (ALDH) enzyme using the ALDEFLUOR® kit (STEMCELL Technologies Inc., Vancouver, Canada) [208]. Prior to sorting, 5 μl of the activated reagent was added to each milliliter of the cell suspension (1 million cells/ml), mixed well, and 500 μl of the suspension was immediately transferred to another tube containing 5 μl of diethylaminobenzaldehyde (DEAB) reagent in 95% ethanol. The tubes were incubated for 45 min at 37°C, following which the cells were centrifuged in cold, and redispersed in cold ALDEFLUOR® assay buffer and stored on ice. Cells were then sorted using BD FACSVantage (BD Biosciences) cell sorter. Cells incubated with DEAB reagent were used to gate for cells having low ALDH level ($ALDH_{low}$), and cells to the right of the gate were sorted as $ALDH_{high}$ population. Around 3 – 4% of MDA-MB-231 cells were $ALDH_{high}$. ALDH-sorted cells were subjected to 30 min of magnetic hyperthermia. Cells incubated with or without SPIO NP and not exposed to alternating magnetic field were used as controls. Treated cells were evaluated for clonogenicty as described above.

3.2.2.5.4. Tumorigenicity assay

The study was carried out in compliance with protocol approved by the Institutional Animal Care and Use Committee at the University of Minnesota. Female BALB/c-nude mice (C.Cg/AnNTac-*Foxn1*^{nu} NE9; Taconic Farms), four to six weeks of

age, were used for the studies. Mice received either 5000 or 50,000 live A549 cells (trypan blue exclusion) that were previously subjected to 30 min of magnetic hyperthermia. Animals that received similar number of untreated cells or cells treated with SPIO NPs but not exposed to alternating magnetic field served as controls. Animals were observed once every three days for the appearance of palpable tumors [206]. Tumor dimensions were also measured using a digital calipers, and the tumor volume (V) was calculated using the formula $V = 0.5(L \times W^2)$, where L and W are the longest and shortest diameters, respectively. Development of 100 mm^3 tumors or 60 days after cell injection (whichever came first) marked the end of the study for each animal.

3.2.2.6. Cytotoxicity studies

3.2.2.6.1. Cell death after magnetic hyperthermia

About 1 million cells were suspended in 500 µl of RPMI (without phenol red and with 5% FBS). 500 µl of 5 mg/ml SPIO NP dispersion in the same medium was added to the cell suspension placed in an alternating magnetic field (6 kA/m, 386 kHz) for 5, 15 or 30 min. The cell suspension temperature was carefully maintained between 43 and 46°C (Figure 3.1). Cells with or without SPIO NPs and not exposed to alternating magnetic field were used as controls. In addition, cells incubated in a water bath at 46°C for 30 min, with or without SPIO NPs, served as conventional hyperthermia controls. Following treatment (after 2 hours), the cells were pelleted down and the amount of lactate dehydrogenase (LDH) released by the cells in the supernatant was analyzed. LDH released by the untreated control was used to normalize for the background cell death and

LDH released by equal number of freeze-thaw lysed cells was used to calculate 100% cell death.

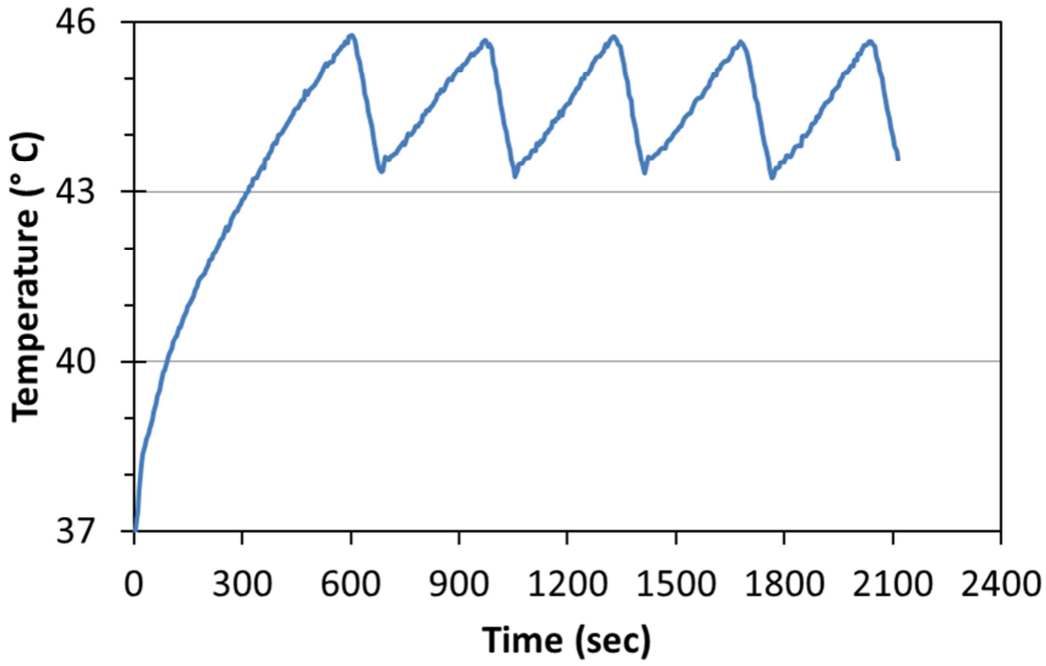

Figure 3.1 Temperature profile during magnetic hyperthermia. Treatment tubes that were pre-equilibrated to 37°C were placed in alternating magnetic field and the temperature was monitored. The magnetic field was turned off when the temperature reached 45.5°C and restarted at 43.5°C to maintain the temperature within a narrow range. The duration of magnetic hyperthermia was defined as the period when the temperature was between 43 and 46°C.

To evaluate the induction of apoptosis by magnetic hyperthermia, treated cells were gently dispersed in medium containing 10% FBS, and plated in 6-well plates. After another 10 hrs, cells were examined for apoptosis/necrosis by a flow-cytometry-based annexin-V FITC/propidium iodide (PI) assay. Briefly, cells were trypsinized and then

centrifuged at 1000 rpm for 8 min. The cell pellets were stained with FITC-conjugated annexin-V and PI according to manufacturer's instructions (BD Pharmingen™, San Jose, CA) and then immediately analyzed using a flow cytometer (BD FACSCalibur™, BD Biosciences, San Jose, CA). FITC and PI fluorescence emissions were detected in FL-1 (515 - 545 nm) and FL-3 (670 long-pass) modes, respectively. Data from at least 10,000 cells were analyzed using Cyflogic software (Cyflo Ltd., Turku, Finland).

3.2.2.6.2. Clonogenicity

Clonogenicity was used as a measure of the proliferative potential of cells subjected to magnetic hyperthermia [209]. Following treatment, 200 live cells (identified by trypan blue exclusion assay) from each group were plated in 10 cm culture dish and allowed to form colonies. After 2 weeks (about 12 – 15 cell doubling times [210, 211]), the plates were washed with DPBS and fixed with 5% formalin in DPBS for 3 min. Colonies were further washed with DPBS and then stained with 0.05% crystal violet for 30 min. Plates were then washed gently with water, air-dried, and the number of colonies formed in each treatment groups was counted. Colonies were counted prior to and after washing and staining steps to account for the loss of colonies during the processing steps.

3.2.2.6.3. Instantaneous cell death during magnetic hyperthermia

Following incubation of cells with SPIO NPs, 2 mM 7-aminoactinomycin-D (7AAD), a cell viability stain, was added to the cells prior to exposing them to magnetic field. Cells not exposed to alternating magnetic field, with or without SPIO NPs, and

cells exposed to 30 min of conventional hyperthermia were used as controls. Following treatments, cells were immediately washed by centrifugation, resuspended in RPMI (without phenol red) and subjected to flow cytometry. 7AAD fluorescence was detected in the FL-3 channel. Data from 20,000 cells in each group were analyzed using Cyflogic software.

3.2.2.7. Reactive oxygen species (ROS) generation after magnetic hyperthermia

Immediately prior to magnetic hyperthermia treatment, 5-(and-6)-chloromethyl-2',7'-dichlorodihydrofluorescein diacetate, acetyl ester (CM-H_2DCFDA) (7.5 μM) and PI (10 μM) were added to A549 cell suspension. Cells were subjected to magnetic hyperthermia and then to flow cytometric analysis. The deacetylated and oxidized product, 2',7'-dichlorofluorescein, formed due to ROS generation in the cells, was detected in the FL-1 channel while PI fluorescence was detected in the FL-3 channel.

To determine the role of ROS in inducing cell death, cells were pretreated with 10 mM N-acetyl cysteine for 1 hr before adding CM-H_2DCFDA and then subjected to 5 min of magnetic hyperthermia. Cells treated with 5 mM hydrogen peroxide with and without N-acetyl cysteine pretreatment served as additional controls.

3.2.2.8. Statistical analysis

Statistical analyses were performed using one-way ANOVA by Bonferroni-Holm method for comparison between individual groups. A probability level of $P < 0.05$ was considered significant.

3.3. Results

3.3.1. Characterization of SPIO NPs

The physico-chemical properties of SPIO NPs used in this study are summarized in Table 3.1. The particles were composed of 74 ± 2% w/w iron oxide, coated with 10 ± 3% w/w myristic acid, and stabilized by 16 ± 2% w/w Pluronic F127. TEM studies indicated that the mean Feret's diameter of the iron oxide core was 12 ± 3 nm (Figure 3.2A). This result was confirmed by the mean particle size calculated from XRD data (12 ± 1 nm) (Figure 3.3). SPIO NPs had an average hydrodynamic diameter of 185 nm, suggesting that particles in aqueous media existed as small aggregates rather than as individual SPIO NPs. FTIR spectroscopy showed the presence of characteristic magnetite bands at 570 cm^{-1} and 400 cm^{-1} and the absence of maghemite bands at 700 cm^{-1} and 630-660 cm^{-1}, indicating that the primary form of iron oxide in SPIO NPs was magnetite (data not shown) [1]. SPIO NPs had a high saturation magnetization of 60.5 emu/g of magnetite, with negligible remanence and coercivity, verifying their superparamagnetic nature (Figure 3.2B). The heating rate of SPIO NPs was concentration-dependent and was similar in both cell culture medium and in agarose gel (Figure 3.2C, D). Based on the heating rates, a concentration of 2.5 mg/ml of SPIO NPs (equivalent to 1.85 mg/ml of magnetite) was found to be optimal for inducing magnetic hyperthermia *in vitro*.

Table 3.1 : SPIO NP characterization	
Composition	
Form of iron oxide	Magnetite
Iron oxide content	74 ± 1.6 %
Myristic acid coating	10 ± 2.7 %
Pluronic F127 coating	16 ± 1.6 %
Particle size	
Particle size (TEM)	12 ± 3 nm
Crystallite size (XRD)	12 ± 1 nm
Hydrodynamic diameter (DLS)	185 nm
Polydispersity	0.22
Magnetic parameters	
Saturation magnetization	60.5 emu/g magnetite
Remanence	1.6 emu/g magnetite
Coercivity	1.37 Oersted

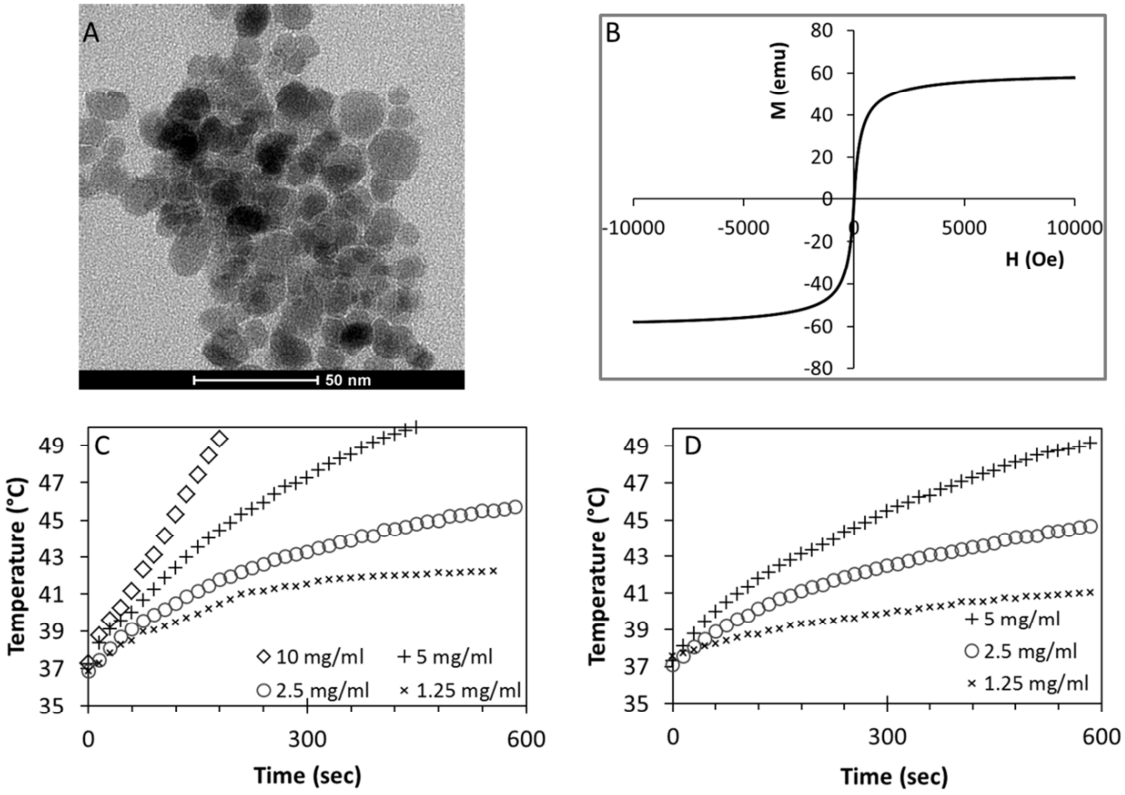

Figure 3.2 Characterization of SPIO NPs. (A) Representative TEM image of SPIO NPs. A drop of aqueous NP suspension was placed on a TEM grid and air-dried before observing under an electron microscope. Scale bar, 50 nm. **(B) Magnetization.** Magnetization curves were recorded on a vibrating sample magnetometer. The curve was normalized to the weight of magnetite added to obtain saturation magnetization per gram of magnetite. The sigmoidal curve is characteristic of superparamagnetic substances. **Heating rates of SPIO NPs dispersed in (C) cell culture medium and (D) agarose gel.** SPIO NP dispersions in a borosilicate glass tube were placed in an alternating magnetic field of 6 kA/m and operating at a frequency of 386 kHz. The initial temperature was equilibrated to 37° C, and the temperature of SPIO NP dispersion was sampled at 15 second intervals using a fluoroptic probe following the application of alternating magnetic field.

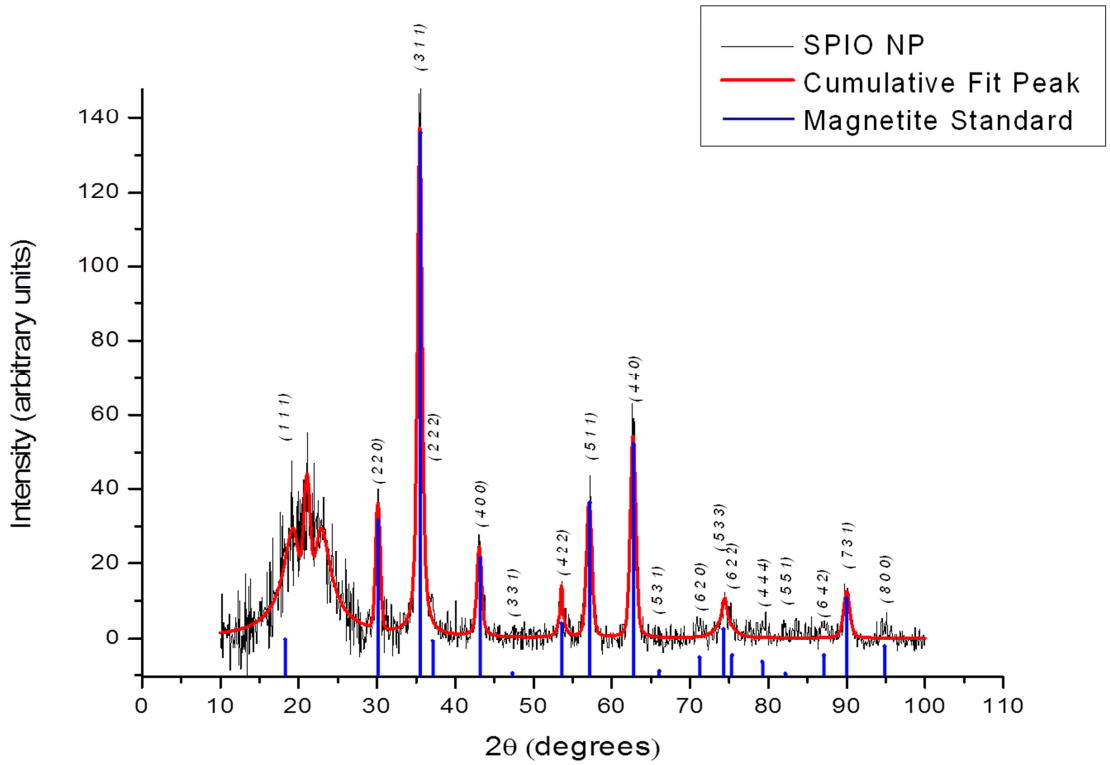

Figure 3.3 XRD pattern of SPIO NP. The XRD pattern (black) is overlaid on the cumulative peak fit data (red) calculated from the summation of the individual peak fit based on the pseudo-Voigt function. Blue bars indicate the standard peak profile of pure magnetite.

3.3.2. Effect of magnetic hyperthermia on CSCs

3.3.2.1. Side population in A549 cells

The side population phenotype, characterized by overexpression of efflux transporters, is believed to be rich in CSCs [206]. Hoechst 33342 is a substrate of both P-glycoprotein (P-gp) and Breast Cancer Resistance Protein (BCRP), and the assay is therefore considered a direct correlate of transporter expression. The difference in the fraction of Hoechst 33342-negative cells with and without the dual efflux inhibitor tariquidar is considered the side population. Interestingly, magnetic hyperthermia resulted in a considerable decrease in the side-population (~12% in magnetic hyperthermia group vs. 20% in the non-hyperthermia SPIO NP control) (Figure 3.4A).

3.3.2.2. Mammosphere assay

Mammospheres are clusters of mammary tumor cells growing in an anchorage-independent fashion and have been shown to be a quantitative indicator of the CSC sub-population [212]. We observed a significant reduction ($P < 0.01$ vs. untreated cells) in mammosphere formation in MDA-MB-231 cells following magnetic hyperthermia (Figure 3.4B). Untreated cells or cells subjected to conventional hyperthermia formed rigid mammospheres, whereas magnetic hyperthermia treated groups formed smaller spheres (Figure 3.5). While 5 min and 15 min of magnetic hyperthermia resulted in 63% and 90% reduction in mammosphere formation respectively, there was a complete absence of mammosphere formation after 30 min of magnetic hyperthermia.

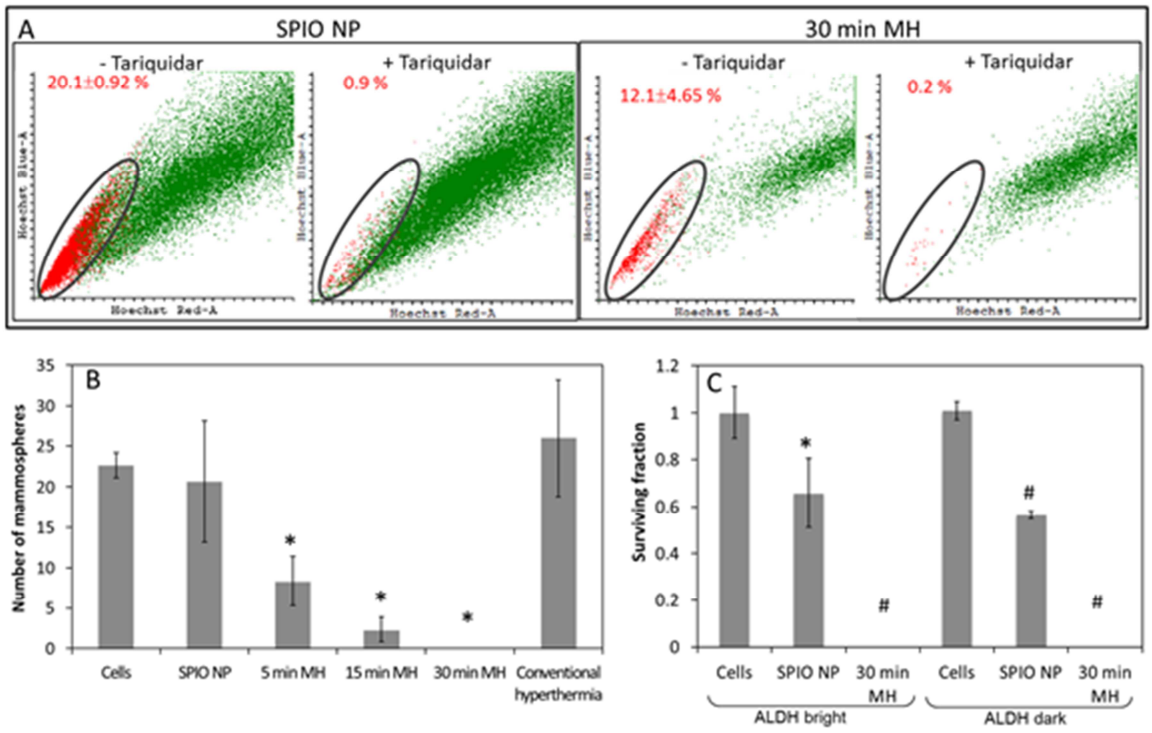

Figure 3.4 Effect of magnetic hyperthermia on CSCs. **(A) Side population assay.** Following magnetic hyperthermia, A549 cells were incubated with Hoechst 33342 dye at 37°C for 90 min followed by flow cytometric analysis of Hoechst 33342 fluorescence in blue and red channels. Cells pretreated with tariquidar (a dual P-gp and BCRP efflux inhibitor) were used as controls. The flow images shown are representative Hoechst profiles of cells treated with SPIO NPS with (left) and without (right) heating. Side population is shown circumscribed within the oval area. The average percent (± S.D.) of side population is shown for each group, n = 3. (**B) Mammosphere formation.** After magnetic hyperthermia, 3000 live cells (counted by trypan blue exclusion) were plated in ultra-low adhesion 6-well plates with mammosphere medium and left undisturbed at 37°C. The number of mammospheres formed was counted using a light microscope on day 5 after treatment. Data shown is mean ± S.D., n = 3. * $P < 0.01$ vs. untreated cells. (**C) Clonogenicity of $ALDH_{high}$ and $ALDH_{low}$ MDA-MB-231 cells.** MDA-MB-231 cells were sorted based on ALDH enzyme levels and then subjected to 30 min of magnetic hyperthermia. Post-treatment, 200 live cells were plated for clonogenicity assessment. The graph shows the relative survival fraction compared to untreated cells. Data shown is mean ± S.D., n = 3. * $P < 0.05$; # $P < 0.001$ vs. untreated cells.

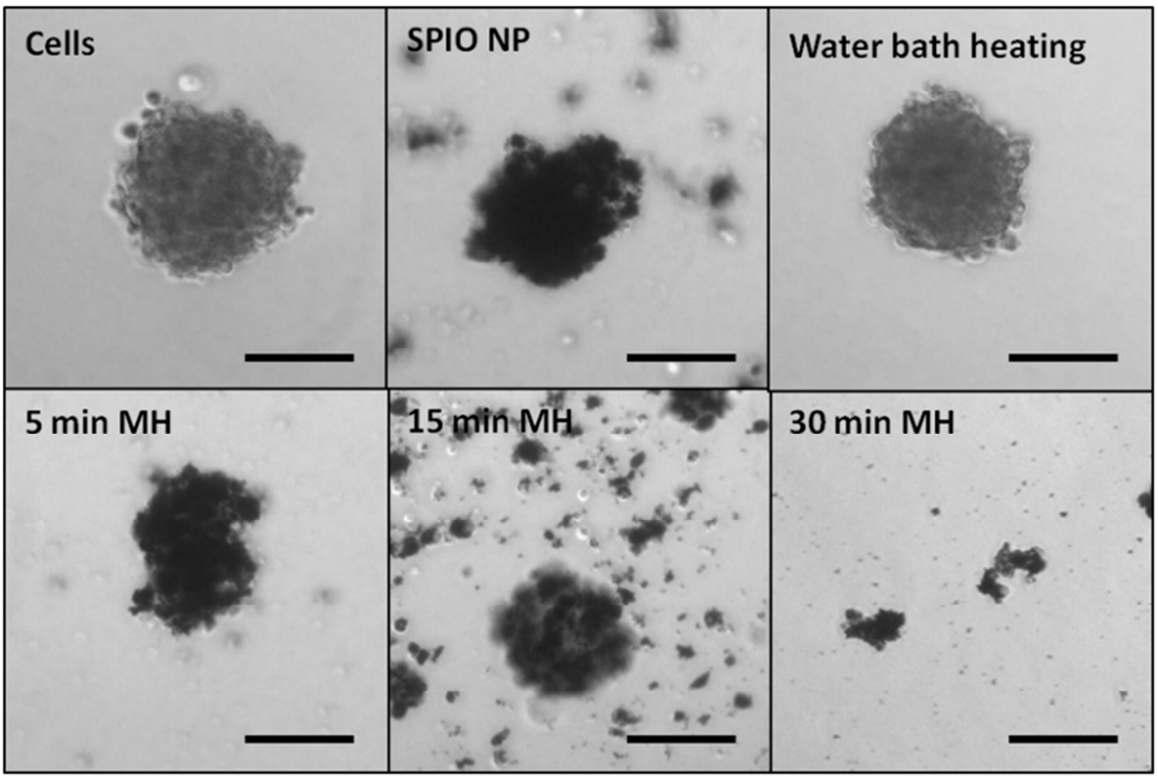

Figure 3.5 Microscopic images of mammospheres formed. The images shown are representative higher magnification images of mammospheres formed in each treatment group referred to in Figure 3.4B. Remaining SPIO aggregates can be seen in all groups that were treated with NPs. Scale bar, 100 µm.

3.3.2.3. ALDH assay

High levels of ALDH have been reported for normal and cancer precursor cells [208,211]. To determine the effect of magnetic hyperthermia on cells with differential ALDH expression, MDA-MB-231 cells were sorted based on the overall levels of the ALDH enzyme. Clonogenicity studies revealed that both $ALDH_{high}$ and $ALDH_{low}$ cells were equally susceptible to magnetic hyperthermia, with a complete absence of colony formation following magnetic hyperthermia in either population (Figure 3.4C). Treatment with SPIO NP also caused a smaller but significant ($p < 0.05$) reduction in clonogenicity of both $ALDH_{high}$ and $ALDH_{low}$ cells.

3.3.2.4. Tumorigenicity assay

A characteristic feature of CSCs is their ability to initiate a tumor in xenotransplantation assays [213]. *In vivo* tumor initiation study performed in nude mice showed a significant delay in tumor initiation with magnetic hyperthermia-treated cells compared to the corresponding controls. While most control animals developed a tumor within 15 days of cell injection, the first tumor appeared in magnetic hyperthermia-treated groups at 21 days (50,000 cell injection) or 36 days (5000 cell injection) post-injection (Figure 3.6A). Furthermore, 40% of the animals that received magnetic hyperthermia-treated tumor cells did not develop tumors even at 60 days post cell injection (Figure 3.6B).

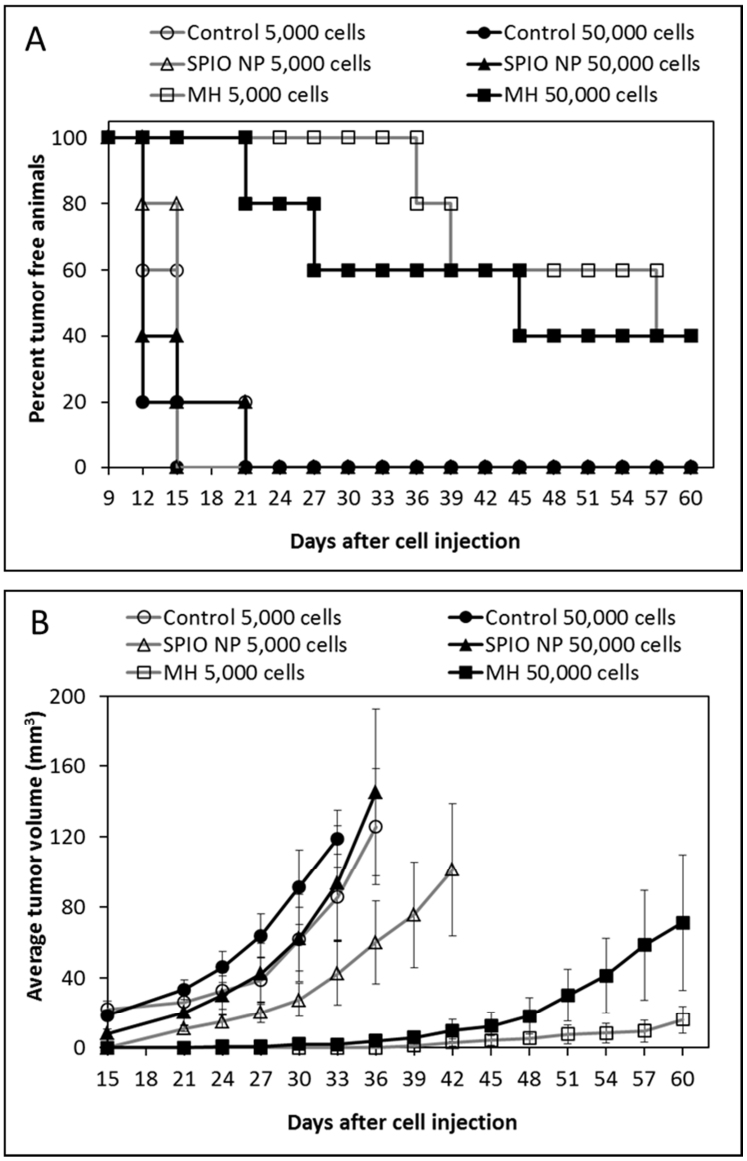

Figure 3.6 In vivo tumorigenicity of magnetic hyperthermia treated cells. A549 cells subjected to magnetic hyperthermia were injected subcutaneously into BALB-nude mice at a cell density of 5000 or 50,000 live cells per animal. Untreated cells or cells incubated with SPIO NPs but not exposed to alternating magnetic field were used as controls. A tumor size of 100 mm^3 or 60 days post cell injection (whichever came first) marked the end of the study. **(A)** Percent tumor-free animals and **(B)** average tumor volumes plotted as a function of days after cell injection. Data shown is mean ± S.D., n = 5.

3.3.3. Cell kill after magnetic hyperthermia

LDH released by cells was used as a quantitative indicator of cell death [214]. Magnetic hyperthermia effectively induced cell death in both A549 and MDA-MB-231 cells (Figure 3.7A), and the efficacy of cell kill was found to increase with increasing duration of exposure to magnetic hyperthermia. Prolonged (30 min) treatment resulted in 88% and 90% cell death in A549 and MDA-MB-231 cells, respectively. Conventional hyperthermia for 30 min was much less effective in killing cancer cells compared to magnetic hyperthermia.

Induction of apoptosis after magnetic hyperthermia was determined using Annexin-FITC/PI assay. The overall percent of healthy cells decreased with increasing duration of treatment (Table 3.2). The proportion of early apoptotic cells was higher for 5 and 15 min magnetic hyperthermia but was lower for 30 min treatment compared to SPIO NP-treated cells. However, there was a higher percent of late apoptotic/necrotic cells in the group exposed to 30 min of magnetic hyperthermia. Conventional hyperthermia was much less effective than magnetic hyperthermia in inducing apoptosis (2% early apoptotic cells and 6% late apoptotic cells).

Clonogenicity assay showed that magnetic hyperthermia resulted in a decrease in the proliferative ability and survival of both A549 and MDA-MB-231 cells (Figure 3.7B). Notably, cells subjected to 30 min of magnetic hyperthermia did not form any colonies in either cell line.

Instantaneous 7AAD uptake was used as a measure of acute cell kill during magnetic hyperthermia. As can be seen from Figure 3.8, magnetic hyperthermia induced instantaneous 7AAD uptake in the treated cells. The 7AAD profile (30%, 47% and 73%

after 5 min, 15 min and 30 min of magnetic hyperthermia, respectively) was comparable to the LDH profile (Figure 3.7A). No significant 7AAD uptake was observed in cells exposed to conventional hyperthermia.

Table 3.2 : Induction of apoptosis and necrosis determined by annexin-V/PI assay

	(PI-/A-) (Healthy)	**(PI-/A+) (Early apoptotic)**	**(PI+/A+) (Late apoptotic)**	**(PI+/A-) (Necrotic)**
Untreated cells	97	1	1	0.4
SPIO NP	97	0.6	2	0.7
5 min magnetic hyperthermia	92	2	6	0.4
15 min magnetic hyperthermia	81	3	14	2
30 min magnetic hyperthermia	62	2	33	3
Conventional hyperthermia	93	2	6	0.2

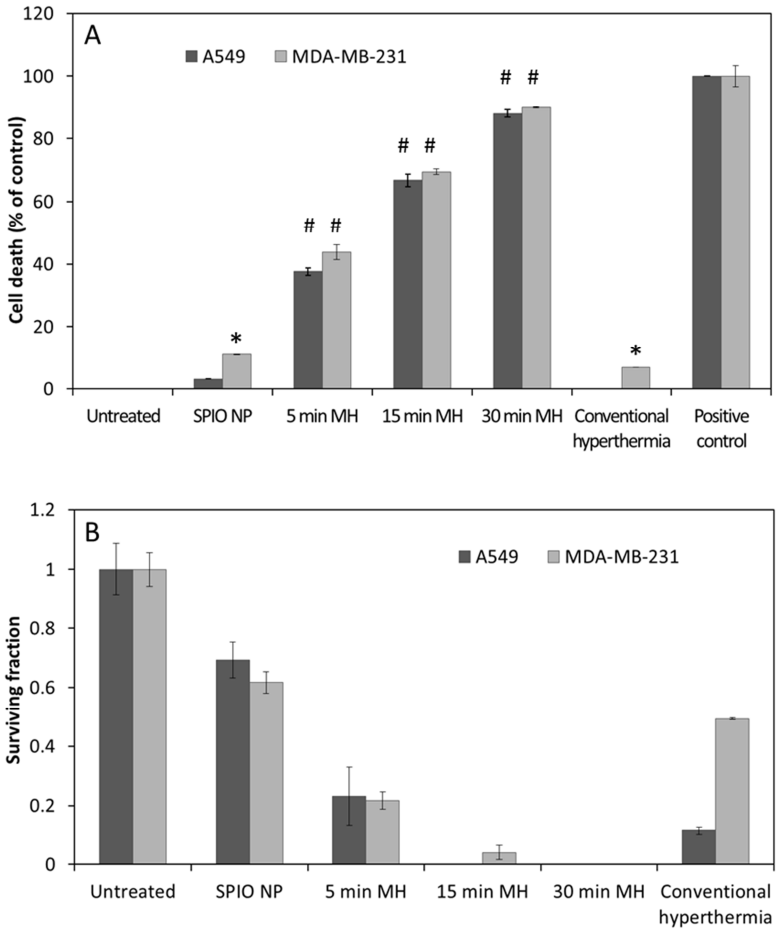

Figure 3.7 Effect of magnetic hyperthermia on tumor cell kill. **(A) LDH release.** Cells were subjected to magnetic hyperthermia for 5, 15 or 30 min, following which the supernatant medium was assayed for the amount of LDH released. SPIO NP-treated cells (without exposure to AMF) and cells subjected to 30 min of conventional hyperthermia at 46 °C were used as controls. Equal numbers of freeze-thaw lysed cells were used to determine LDH release from 100% cell death while untreated cells were used to determine background LDH release. Data shown is mean ± S.D., n = 3. * $P < 0.05$; # $P < 0.01$ vs. untreated cells. **(B) Clonogenicity.** About 200 live cells from each treatment group were plated in a 10 cm tissue culture plate and observed for colony formation. The number of colonies formed was counted 2 weeks later. Data shown is mean ± S.D., n = 3. All treatments resulted in statistical significant ($P < 0.01$) decrease in surviving fraction.

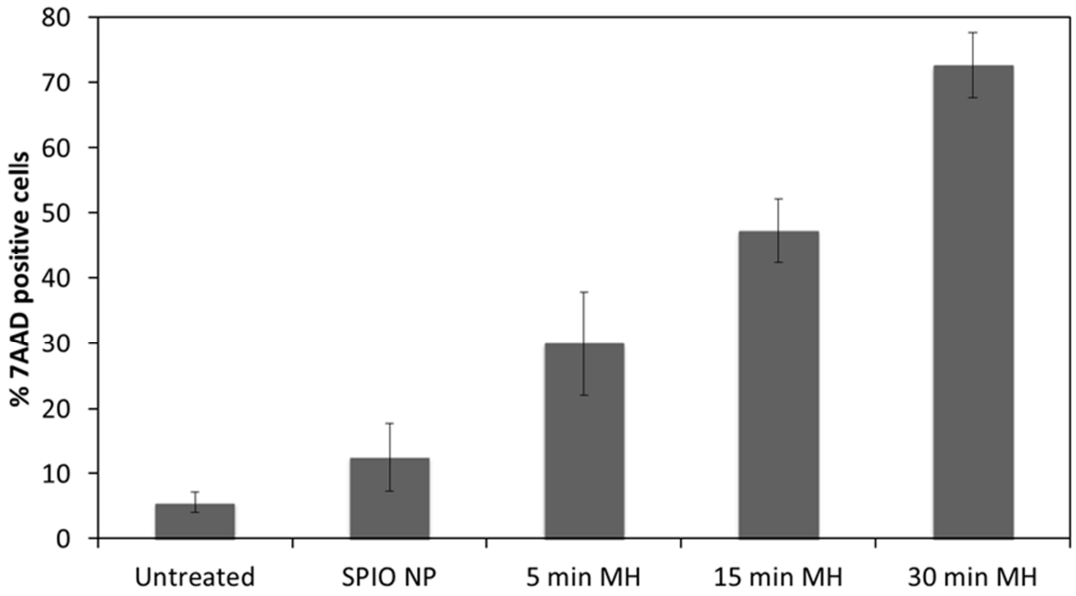

Figure 3.8 Instantaneous 7AAD uptake during magnetic hyperthermia. 7AAD was added to each treatment tube immediately prior to magnetic hyperthermia. After treatment, the cells were washed to eliminate excess 7AAD and subjected to flow cytometric analysis. Data shown is mean ± S.D., n = 3. All hyperthermia treatments resulted in statistical significant ($P < 0.01$) increase in 7AAD uptake.

3.3.4. ROS generation during magnetic hyperthermia

ROS generation increased with increased duration of magnetic hyperthermia (Figure 3.9). Conventional hyperthermia did not affect ROS levels compared to untreated cells. Following magnetic hyperthermia, ROS positive population appeared to become necrotic with time, as evidenced by the migration of ROS^{high}/PI^{low} population to ROS^{high}/PI^{high} quadrant (Figure 3.10). Addition of N-acetyl cysteine, an antioxidant [215], inhibited ROS generation (not shown) and decreased the fraction of cells becoming PI

positive without affecting the initial population of cells that took up PI instantaneously (Figure 3.11). Interestingly, though ROS production and PI uptake by cells that underwent conventional hyperthermia was comparable to that by untreated cells, cells subjected to conventional hyperthermia in the presence of SPIO NPs demonstrated greater ROS production compared to those that received only SPIO NPs (Figure 3.12).

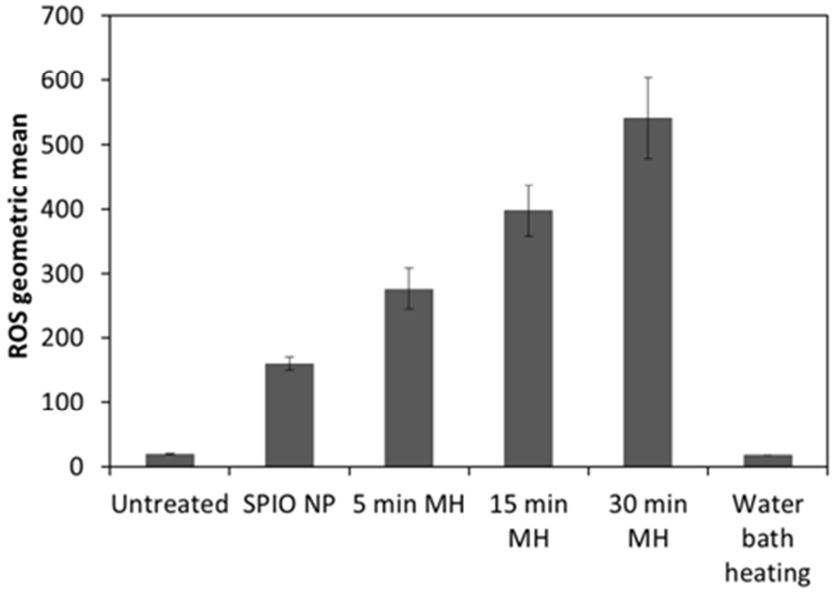

Figure 3.9 ROS generation immediately after treatment. CM- H_2DCFDA was added to A549 cells immediately before exposure to alternating magnetic field, followed by flow cytometric analysis to determine ROS levels. The graph shows the effect of treatments on geometric mean intensity of fluorescence, an indicator of ROS levels in the cells. Data shown is mean ± S.D., n = 3. All treatments resulted in statistical significant ($P < 0.01$) increase in the geometric mean intensity of ROS fluorescence.

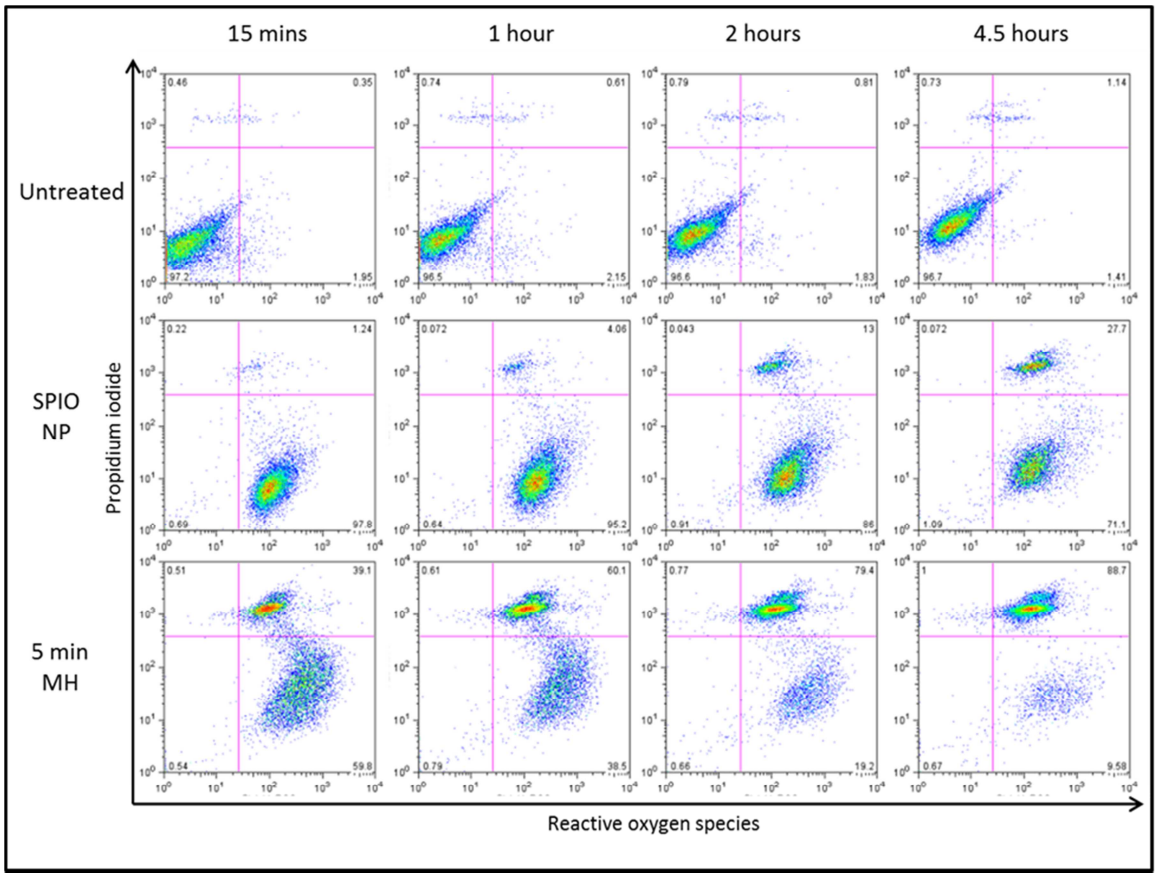

Figure 3.10 Kinetic study to monitor ROS levels and PI uptake by cells subjected to magnetic hyperthermia. Cells were first treated with CM- H_2DCFDA and PI and then subjected to 5 min of magnetic hyperthermia. Fluorescence from ROS generation and PI uptake by the cells were monitored by flow cytometry. The change in the flow profile of untreated (top), cells treated with SPIO NPs (middle) and cells treated with magnetic hyperthermia (bottom) are shown at different times after treatment.

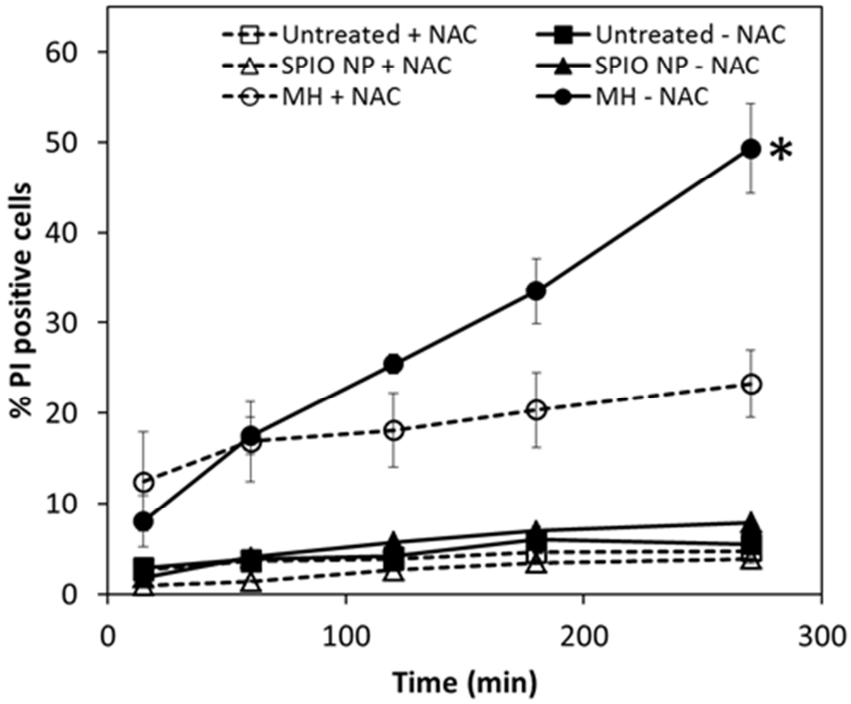

Figure 3.11 Effect of ROS scavenging on PI uptake by magnetic hyperthermia treated cells. Prior to SPIO NP or CM-H_2DCFDA addition and exposure to alternating magnetic field, cells were pretreated with N-acetyl cysteine (NAC) to scavenge free radicals. The percent of PI positive cells at different time point are plotted for the treatment groups. Data shown is mean ± S.D., n = 3. * $P < 0.001$ vs. all other groups.

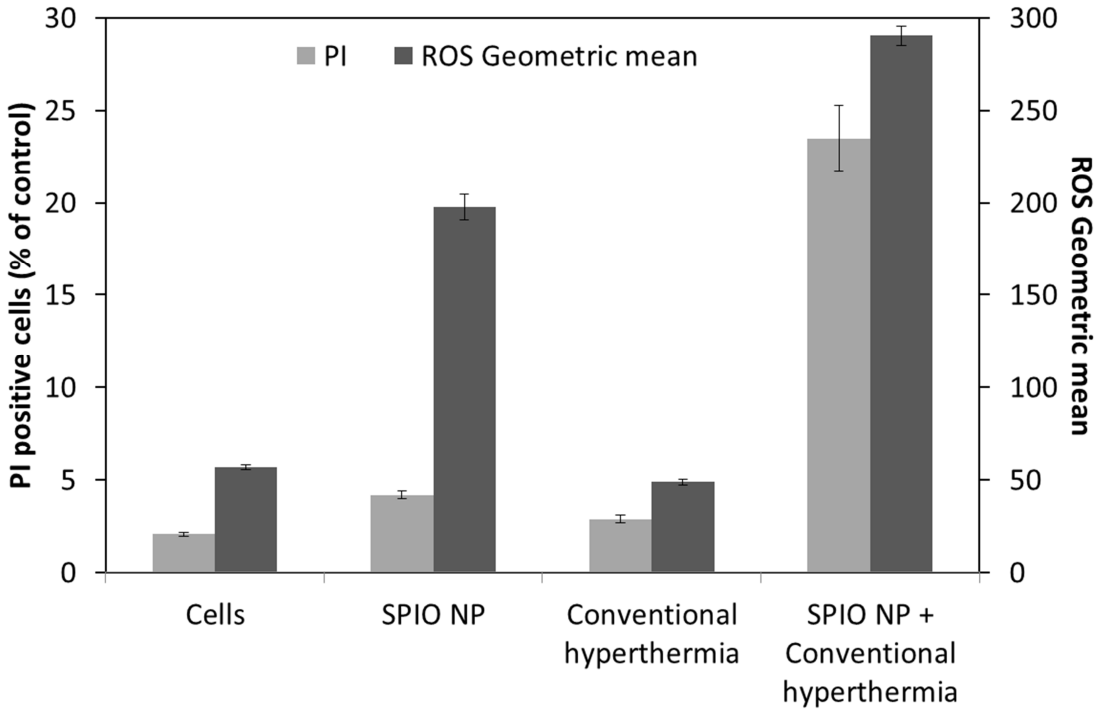

Figure 3.12 ROS generation and PI uptake by cells treated with conventional hyperthermia in the presence of SPIO nanoparticles. CM-H_2DCFDA and PI was added to cells immediately before hyperthermia treatment. Fluorescence from ROS generation and PI uptake by the cells were measured 2 hrs after treatment by flow cytometry. The graph plots PI positive cells (light gray bars) in the primary axis and the geometric mean intensity (which is proportional to ROS levels in cells) (dark gray bars) in the secondary axis. An increase in ROS levels and cell death (PI uptake) is observed in cells incubated with SPIO NP while being subjected to conventional hyperthermia. Data shown is mean ± S.D., n = 3. All treatments resulted in statistical significant ($P < 0.01$) difference in the geometric mean intensity of ROS fluorescence and the percent PI positive cells compared to untreated cells.

3.4. Discussion

Magnetic hyperthermia, a technique involving the use of SPIO NPs subjected to AMF to generate heat [58], has been studied for treating tumors as early as 1957 [59]. The main advantage of magnetic hyperthermia is that the heating rate can be well controlled by adjusting particle size and shape of SPIO NPs as well as by modulating the properties of the alternating magnetic field [60]. There are several magnetic materials that can be used for inducing magnetic hyperthermia. However, most studies have focused on magnetic iron oxides, Fe_3O_4 (magnetite) [61,62] and γ –Fe_2O_3 (maghemite) [63,64], which have been proved to be well tolerated in clinical studies [65]. The core size of SPIO NPs dictates the primary mechanism of heat generation – Brownian relaxation and/or Néel relaxation [68,67]. The predominant mechanism of heat generation by 12 nm SPIO NPs used in our studies is through Néel relaxation, a mechanism of heat generation unaffected by suspending medium viscosity. This was confirmed from the similar heating rates observed for SPIO NPs in liquid and gel media. This data suggests that heat production by these particles will not likely be affected by the presence of dense extracellular matrix found in solid tumors [216]. Additionally, higher saturation magnetization of magnetic substances is more desirable, because this translates to higher heating rate per unit mass. SPIO NPs used in our studies were composed of magnetite, which possesses higher saturation magnetization than maghemite [217]. Optimum size and properties of synthesized SPIO NPs, along with their high saturation magnetization and iron content, allowed for effective induction of magnetic hyperthermia in our studies.

A number of preclinical studies have demonstrated the potential use of magnetic hyperthermia as an effective anticancer treatment modality [58]. In addition, magnetic hyperthermia is in clinical trials for different cancers [199,218]. However, there are no reports on the effect of magnetic hyperthermia on CSCs, a sub-population that is thought to be responsible for tumor drug resistance and relapse [219]. Since no single assay is confirmatory with regard to the effect of treatments on CSCs, we evaluated the effect of magnetic hyperthermia on multiple biomarkers and functional properties of CSCs. Hoechst 33342 efflux [206] and ALDH [220] assays are functional assays identifying CSC-rich population, while mammosphere formation and tumorigenicity assays are based on the growth and proliferative properties unique to CSCs [221]. All of these assays indicated that magnetic hyperthermia reduced or, in some cases, eliminated the CSC sub-population in treated cells.

Magnetic hyperthermia was effective in reducing CSC population in both long-term assays such as mammosphere formation as well as in short-term studies such as side population assay. The short-term effects of magnetic hyperthermia could be attributed to the induction of acute cell death, which was evident from high LDH release immediately after the treatment. The increased number of 7AAD positive cells immediately after treatment further points to the possibility of acute necrosis induced by magnetic hyperthermia. Lack of significant acute cell kill with conventional hyperthermia suggests that necrosis brought about by magnetic hyperthermia was likely temperature-independent. CSCs have been shown to be resistant to induction of apoptosis [222], a slow programmed process of cell death. Necrosis is a more violent and acute cell death, most

often mediated by mechanical damage to cell membrane and/or other vital cellular organelles [223]. If magnetic hyperthermia indeed caused necrosis, it is unlikely that CSCs will have resistance mechanisms to tolerate this acute cell death pathway [213].

Exposure of cells to 30 min of magnetic hyperthermia resulted in the induction of apoptosis/necrosis in only about 35% of cells 20 hrs after treatment, suggesting that a majority of the cells are viable and healthy. However, these cells did not form any colonies in the clonogenicity assay. This implies that in addition to acute necrosis, there is a pronounced long-term effect of magnetic hyperthermia on CSCs. A mechanism postulated for the resistance of CSCs against DNA damage is decreased basal levels of ROS generation in CSCs [194]. Since SPIO NPs have been reported to induce ROS [224], we investigated ROS generation as a possible mechanism of cell kill with magnetic hyperthermia. Immediately after magnetic hyperthermia, ROS levels were higher than in controls, and this appeared to be followed by a slow increase in the number of dying cells. Inhibition of ROS generation using an antioxidant suppressed this transition. These results suggest that magnetic hyperthermia induces ROS generation, which results in additional cell death after some latency. Similar increase in ROS production and cell death was observed in cells incubated with SPIO NPs and subjected to conventional hyperthermia but not in those subjected to either conventional hyperthermia alone or SPIO NP treatment alone. Overall, our studies suggest that ROS generation by magnetic hyperthermia is mediated by the presence of SPIO NPs and is amplified by higher temperatures. One possibility is that SPIO NPs generate ROS, which would normally be

scavenged efficiently by CSCs [225]; however, generation of heat could decrease the ability of CSCs to scavenge ROS and thereby increases their susceptibility to ROS.

3.5. Conclusions

CSCs are considered to play important roles in tumor drug resistance and recurrence. Our studies show that CSCs and non-CSCs are equally susceptible to cell death induced by magnetic hyperthermia. Further, magnetic hyperthermia induces both acute necrosis and a slower, ROS-mediated cell-death in treated cells. Some of the cell kill events appear to be temperature-independent, although elevated temperatures appear to amplify those effects. Overall, these results suggest the potential for effective CSC eradication by magnetic hyperthermia. Future studies will investigate the effect of magnetic hyperthermia on *in vivo* tumor growth and tumor recurrence.

Chapter 4

INHALABLE MAGNETIC NANOPARTICLE MEDIATED TARGETED MAGNETIC HYPERTHERMIA FOR LUNG CANCER THERAPY

Tanmoy Sadhukha,[a] Timothy S. Wiedmann [a] and Jayanth Panyam[a,b]

[a] Department of Pharmaceutics, [b] Masonic Cancer Center, University of Minnesota, Minneapolis, MN 55455

Running Title: Targeted Magnetic Hyperthermia for Lung Cancer Therapy

Keywords: superparamagnetic iron oxide, magnetic hyperthermia, EGFR targeting, inhalation delivery, lung cancer

4.1. Introduction

Lung cancer is the leading cause of cancer-related deaths in the United States [2]. Surgical resection is the primary choice of treatment, followed by radiation and/or chemotherapy [226]. Despite earlier diagnosis and the availability of new molecularly-targeted drugs, the five-year survival rate has not changed significantly over the last several years [2]. Metastatic and locally advanced disease stages are not amenable to surgical resection, and importantly, a majority of patients who undergo surgery eventually experience relapse [227-229]. Poor response rates and survival with current treatments clearly indicate the urgent need for developing an effective means to treat non-small cell lung cancer.

Magnetic hyperthermia is a novel non-invasive approach for tumor ablation and is based on heat generation by magnetic materials, such as superparamagnetic iron oxide (SPIO) nanoparticles, when subjected to an alternating magnetic field (AMF) [156,157]. Depending on the size of SPIO nanoparticles and the frequency of AMF, heat is generated through either Néel or Brownian relaxation. The heat generated dissipates over short distances due to the high thermal conductivity of water and can, therefore, be used for highly focused heating [58,158]. However, inadequate delivery of magnetic nanoparticles to tumor cells can result in sub-lethal temperature change and induction of resistance [230]. Additionally, non-targeted delivery of these particles to the healthy tissues can result in heat damage to normal tissues.

In our studies, we developed epidermal growth factor receptor (EGFR)-targeted, inhalable SPIO nanoparticles for magnetic hyperthermia of non-small cell lung cancer

(NSCLC). EGFR overexpression has been observed in as many as 70% of NSCLC patients [140-142], in whom EGFR expression is elevated in epithelial sites within tumors than in sites adjacent to and distant from tumors. We examined the effect of EGFR targeting on accumulation and retention of inhaled SPIO nanoparticles in the tumor tissue and the effect of targeted magnetic hyperthermia therapy on tumor growth in an orthotopic lung tumor model.

4.2. Materials and Methods

4.2.1. Materials

Ferrous chloride tetrahydrate, ferric chloride hexahydrate, myristic acid, Pluronic F127, ascorbic acid, potassium hydroxide, 1,10 phenanthroline and sodium acetate were purchased from Sigma (St. Louis, MO). Penicillin/streptomycin, fetal bovine serum, RPMI 1640, Dulbecco's phosphate buffered saline, F-12K (Kaighn's modification) and trypsin-EDTA solution were obtained from Invitrogen Corporation (Carlsbad, CA).

4.2.2. Methods

4.2.2.1. Synthesis of carboxy-terminated pluronic F127 (CTP)

The synthesis of CTP involved the use of an acid anhydride, which is highly susceptible to the presence of moisture. Hence, all the solvents used in the reaction were anhydrous and the reaction environment was maintained as dry as possible. A mass of 2 grams of pluronic F127 was dissolved in 40 ml of anhydrous tetrahydrofuran. To the

solution, 100 mg of 4-dimethylaminopyridine, 72 µl of triethylamine and 800 mg of succinic anhydride were added, and the flask was sealed immediately. The mixture was stirred at room temperature for 48 hours under nitrogen atmosphere. After 2 days, the volatile solvent was removed by rotary evaporation, and the dry residue was dissolved in 40 ml of carbon tetrachloride. The undissolved, unconjugated succinic anhydride was removed by filtration. The remaining polymer solution was concentrated using a rotary evaporator, and CTP was precipitated by drop-wise addition of the solution in cold, dry diethyl ether [231]. The residue was filtered, dried in a vacuum oven at 40° C overnight and analyzed by proton NMR. The final yield of CTP was 1.74 g.

Completion of the reaction was confirmed by NMR. Around 25 mg of CTP was dissolved in 750 µl of deuterated water and analyzed using a 400 MHz NMR. The NMR spectrum of unmodified pluronic F127 was also obtained for comparison.

4.2.2.2. Conjugation of EGFR-targeting peptide or the isotype scrambled peptide to CTP

A mass of 42 mg of CTP was dispersed in 1.8 ml deionized water. To this solution, 10 mg of *N*-(3-Dimethyl aminopropyl)-*N′*-ethylcarbodiimide hydrochloride (EDC) and 14 mg of *N*-hydroxysulfosuccinimide sodium salt (sulfo-NHS) (each dissolved in 100 µl deionized water) were added and then stirred for 15 minutes at room temperature. The pH of the reaction mixture was 6 -7. The excess unreacted EDC was quenched by the addition of β-mercaptoethanol at a final concentration of 130 mM. 10 mg of either the EGFR targeted peptide (YHWYGYTPQNVI) or the scrambled peptide (HWPYAHPTHPSW) [143] was dissolved in 200 µl of deionized water and added to the

reaction mixture. 245 µl of 10X PBS was added to buffer the reaction and the pH was maintained around 7 – 8. The reaction mixture was stirred overnight at room temperature [232]. The solution was dialyzed against water for 48 hours using a 3500 Da molecular weight cutoff Slide-a-lyzer® dialysis cassette, and the final solution was lyophilized (Labconco, FreeZone 4.5, Kansas City, MO).

Conjugation of the peptides to CTP was confirmed by NMR. Around 25 mg of the conjugate was dissolved in 750 µl of deuterated water and analyzed by a 400 MHz NMR. NMR spectra of the free peptides were used for identification of the resonances corresponding to the peptide.

4.2.2.3. Synthesis of water-dispersible SPIO nanoparticles

SPIO nanoparticles were synthesized from iron chlorides by the addition of a strong base, followed by coating with a fatty acid to prevent oxidation and then with a surfactant to form a stable aqueous dispersion [204]. Specifically, 0.82 g of ferric chloride hexahydrate and 0.33 g of ferrous chloride tetrahydrate were dissolved in 30 ml of degassed and nitrogen-purged water, and 3 ml of 5 M ammonium hydroxide was added drop-wise to this solution, which was then stirred for 30 minutes. The resulting iron oxide nanoparticles were washed three times with nitrogen-purged water, sonicated in a water bath sonicator for 2 min, and then heated to 80°C. About 100 mg of myristic acid was added to the heated mixture and stirred for another 30 min. Excess myristic acid was removed by two washes with ethanol, followed by two additional washes with water to remove excess ethanol. Each wash was followed by magnetic separation of nanoparticles. Myristic acid coated particles were then suspended in 30 ml water using a water-bath

sonicator. Targeted or scrambled peptide conjugated pluronic, equivalent to 5% surface coverage of the peptide (5.5 mg and 11.7 mg of targeted and scrambled peptides, respectively), was mixed with pluronic F127 to yield a total mass of 100 mg, which was then added to the suspension and sonicated in a bath sonicator for 1 hour. Every step of the synthesis was conducted carefully to minimize exposure to atmospheric oxygen.

4.2.2.4. Characterization of SPIO nanoparticles

The average hydrodynamic diameter of SPIO nanoparticles was determined by dynamic light scattering. About 1 mg of SPIO nanoparticles was dispersed in 2 ml of deionized water by sonication and the dispersion was subjected to particle size analysis using a Delsa™ Nano C Particle Analyzer (Beckman, Brea, CA). The measurement was performed at 25°C and at a 165° scattering angle. Mean hydrodynamic diameter was calculated based on size distribution by weight, assuming a lognormal distribution. Five individual size measurement runs were performed, with each run recording 150 size events.

The iron content of the SPIO nanoparticles was measured using the 1,10 phenanthroline-based iron assay [160]. SPIO nanoparticles were first dissolved in12 N hydrochloric acid. The solution was then diluted with distilled water to obtain a final acid concentration of 0.2 N. To the acid solution of SPIO nanoparticles, 10 mg/ml ascorbic acid, 1.2 mg/ml 1,10 phenanthroline, 22.4 mg/ml potassium hydroxide and 123 mg/ml sodium acetate were added in a volume ratio of 1:1:1:1:5. Absorbance of the resultant solution was measured at 490 nm using a microplate reader (ELx800 Absorbance

Microplate Reader, Biotek, Winooski, VT). Ferric chloride (hexahydrate) solutions in 0.2 N hydrochloric acid was used as a standard.

4.2.2.5. Magnetic heating rate

SPIO nanoparticles were dispersed in 1 ml of Hank's F-12K medium in 10 mm X 75 mm disposable borosilicate glass cell culture tubes. Magnetic heating was performed using an induction heating system (1 kW Hotshot, Ameritherm Inc., Scottsville, NY) by placing the suspension at the center of a multiturn copper coil that generated AMF (nominal magnetic field strength of 6 kA/m and frequency of 386 kHz). The temperature change was measured using a fluoroptic® probe (Lumasense Technologies, Santa Clara, CA) at five second intervals. Samples were equilibrated to 37 °C using a water-bath before exposure to the field.

4.2.2.6. Aerosol generation and characterization

Aerosolization of SPIO nanoparticles was achieved by ultrasonic atomization [233]. A Pyrex glass baffle was constructed in-house and placed in a water bath, directly over a 1.7 MHz ultrasonic transducer [234]. About 13 ml of SPIO nanoparticle dispersion in 40% ethanol, containing 8 mg magnetite per ml was loaded into the baffle. Compressed air directed into the baffle at a flow rate of 0.5 L/min (as measured by an inline flow meter) entrained the aerosol droplets containing the SPIO nanoparticle dispersion and carried the particles into a subsequent drying assembly. The iron oxide output in the aerosol was measured by collecting the aerosolized and dried SPIO particles for a predetermined period of time on Whatman quartz microfiber filters suitable for air sampling [235]. The

filters were assayed using the above procedure and the iron oxide output rate was calculated as iron oxide amount collected per unit time.

The aerosol particle size distribution was determined with a Mercer style seven-stage Intox cascade impactor operating at a sample flow rate of 0.5 L/min. The aerosol generated was passed through a heated drying column before passing through the cascade impactor. Aerosol particles deposited at each stage of the cascade impactor was collected and analyzed by iron assay to obtain the particle size distribution. The mass median aerodynamic diameter (MMAD) and associated geometric standard deviation (GSD) were calculated from linear regression of an X– probability plot of the cumulative undersized mass as a function of logarithm of the impactor stage cutoff diameter using OriginPro 8 software (OriginLab Corporation, Northampton, MA) [235].

4.2.2.7. Cell culture studies

A549 (human lung adenocarcinoma) and A549-Luc (luciferase-transfected A549) cells were used in the study. Both cell lines were propagated using F-12K medium supplemented with 10% fetal bovine serum (FBS) and 1% antibiotic solution and maintained at 37 °C and in 5% carbon dioxide.

4.2.2.8. Demonstration of role of EGFR in tumor cell uptake of functionalized nanoparticles

A549 cells were plated in a 6-well plate 4 hours before the start of the study. Cells were washed with phosphate buffered saline (PBS) to remove non-adherent cells and 1 mg (magnetite equivalent) of targeted SPIO particles, scrambled peptide-conjugated particles, particles without any peptide, or targeted particles with excess free targeting

peptide were added to the cells in a total volume of 2 ml of cell culture medium containing 5% FBS. The plates were incubated on ice for 30 minutes, washed thrice with PBS and incubated at 37°C for an additional 45 minutes. At the end of the incubation, cells were lysed with 400 µl of RIPA buffer and assayed for total cell protein content and iron content [160] (by iron assay procedure described before).

To evaluate EGFR targeting on the effectiveness of magnetic hyperthermia, plated A549 cells were incubated with targeted or non-targeted particles for 30 minutes at 4°C, washed three times with PBS, incubated at 37°C for 45 minutes and then subjected to AMF (6 kA/m at 386 kHz frequency). Following AMF exposure, 10 µM propidium iodide was added to the cells and observed under a fluorescent microscope immediately and at 24 hrs after AMF exposure.

4.2.2.9. Orthotopic lung tumor model

All animal studies were carried out in compliance with protocol approved by the Institutional Animal Care and Use Committee at the University of Minnesota. Female Fox Chase SCID® Beige mice (CB17.Cg-*Prkdc*^{scid}*Lyst*$^{bg-J}$/Crl) four to five weeks of age, were obtained from Charles River Laboratories.

A mouse orthotopic lung tumor model [236] was used in the studies. Lung tumor cells that have been stably transfected with fire-fly luciferase were used to facilitate the visualization of tumor cells in live animals using bioluminescence imaging. A549-luc-C8 Bioware® Cell Line (Caliper Lifesciences) is a luciferase expressing cell line derived from A549 human lung squamous carcinoma cells by stable transfection of the North American Firefly Luciferase gene expressed from the CMV promoter. Intravenous

injection of 1 X 10^6 A549-luc-C8 cells led to detectable increase in bioluminescence in the lungs by 2 weeks.

4.2.2.10. Lung delivery of SPIO nanoparticles

4.2.2.10.1. Tracheal instillation

The mice were anesthetized and placed on a rodent intubation stand, supported by their incisors. The tongue was rolled out using a sterile cotton swab and held between the fingers. A fiber-optic light and stylus (BioLite, BioTex, Inc., TX) connected to an endotracheal tube was used to visualize the tracheal opening and to carefully insert the attached endotracheal tube into the trachea. An inflation bulb was used to confirm the proper insertion of the endotracheal tube by monitoring the inflation of the thoracic region on gently pushing in air through the tube. Targeted or non-targeted SPIO particles (50 µl, 10 mg/ml iron oxide equivalent) were instilled through the endotracheal tube. The mice were kept upright for a minute to prevent back-flow of the liquid and then placed on a heating pad to assist in faster recovery from anesthesia [237].

4.2.2.10.2. Inhalation

The aerosol was generated as described above, but the dried SPIO aerosols were directed through the drying assembly into an animal chamber, which was comprised of a 4-port double-walled chamber. The dried aerosol stream entered the top inlet into a stirred chamber. The animals were placed into each port with their nose exposed to the aerosol stream in the stirred chamber. The exhaust tube was connected to the space between the two walls, thus ensuring that the mice underwent a “nose-only” exposure for

30 minutes. Filter collections were made three times both before and after the exposure to measure the aerosol output. The aerosol stream was also passed through a 7-stage Intox cascade impactor before each exposure to determine the aerosol particle size distribution (MMAD and GSD) [235].

4.2.2.11. Distribution of SPIO nanoparticles following instillation and inhalation delivery

Targeted or scrambled peptide conjugated SPIO nanoparticles were administered to tumor bearing animals (n = 6 per time point per group) by the two routes of administration described above. The animals were euthanized at 1 hour, 1 day or 1 week after SPIO administration. The lungs, liver, spleen, kidney, heart, stomach and blood were collected to analyze the distribution of SPIO particles. Additionally, lungs of treated animals were also sectioned, stained with hematoxylin and eosin (H & E staining) and Prussian blue (for iron) [238] and imaged after the last time point to visualize the distribution of SPIO particles. Basal level of iron in each organ was determined in six healthy mice.

4.2.2.12. In vivo efficacy of targeted magnetic hyperthermia after inhalation delivery of SPIO nanoparticles

Fox Chase SCID® Beige mice were injected A549-luc cells intravenously to facilitate the development of tumors in the lungs. Once the lung bioluminescence reached about 0.5 X 10^6 photons/sec, animals were administered SPIO nanoparticles by inhalation. After 7 days, some of the treated animals were subjected to 30 minutes of magnetic hyperthermia. Untreated animals and animals receiving the particles without

exposure to AMF served as controls. Lung bioluminescence was monitored three times weekly for 4 weeks. At the end of the study, animals were euthanized, and the lungs and trachea were removed and weighed. Assuming little variability between the lung weights of individual mice, the differences in lung weights were attributed to the variable mass of lung tumors.

4.2.2.13. Statistical analysis

Statistical analyses were performed using one-way ANOVA, followed by Bonferroni-Holm method for comparison between individual groups. A probability level of $P < 0.05$ was considered significant.

4.3. Results

4.3.1. Characterization of inhalable SPIO nanoparticles

Conversion of the hydroxyl end group of pluronic F127 into a carboxyl group was confirmed using NMR spectroscopy and the conversion efficiency was almost 100% (Figure 4.1). Presence of targeted or scrambled peptides could be detected in the NMR spectra of the modified polymer (Figure 4.1). The conjugation efficiency of EGFR-targeted peptide and scrambled peptide to CTP was 90.4 ± 10.5% and 42.8 ± 4.6 % respectively. SPIO nanoparticles were composed of 74 ± 2% w/w iron oxide, coated with 10 ± 3% w/w myristic acid, and stabilized by 16 ± 2% w/w Pluronic f127. The hydrodynamic diameter of unconjugated (pluronic COOH terminated) SPIO nanoparticles was 309 ± 24 nm while that of targeted peptide and scrambled peptide

conjugated particles were 369 ± 34 nm and 365 ± 45 nm, respectively. The heating rate of SPIO nanoparticles was concentration-dependent, and was similar for both targeted and non-targeted SPIO nanoparticles (Figure 4.2).

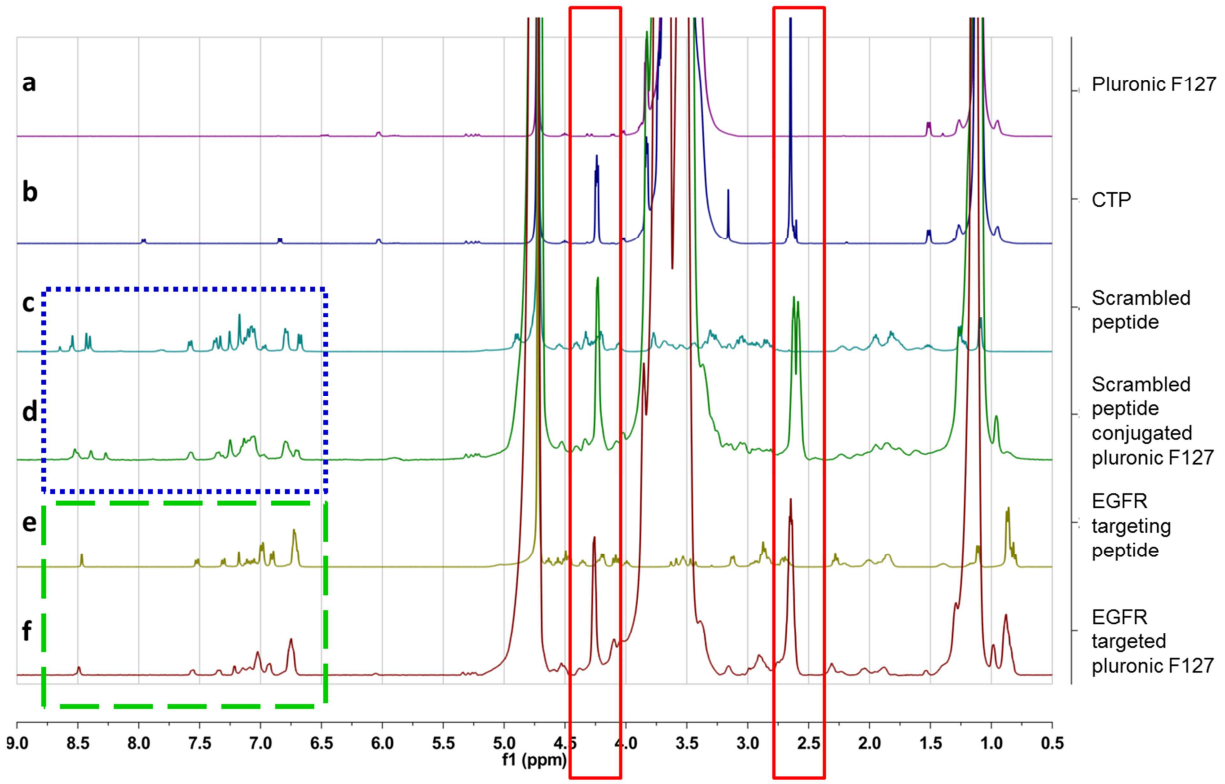

Figure 4.1 NMR spectra of modified pluronic f127. Pluronic F127 has a characteristic NMR peak at 1.02 ppm and multiple peaks between 3 and 4 ppm. Conjugation of carboxy end group can be detected by the appearance of new peaks at 2.6 and around 4.2 ppm (solid box). NMR spectrum of the EGFR targeting peptide is different from the scrambled peptide with the most visible difference between 6 – 9 ppm. Peptide conjugation to the carboxy terminated pluronic (CTP) can be verified from the presence of both carboxy modification peaks (solid box) and EGFR targeting peptide (dotted box) or scrambled peptide (dashed box) peaks.

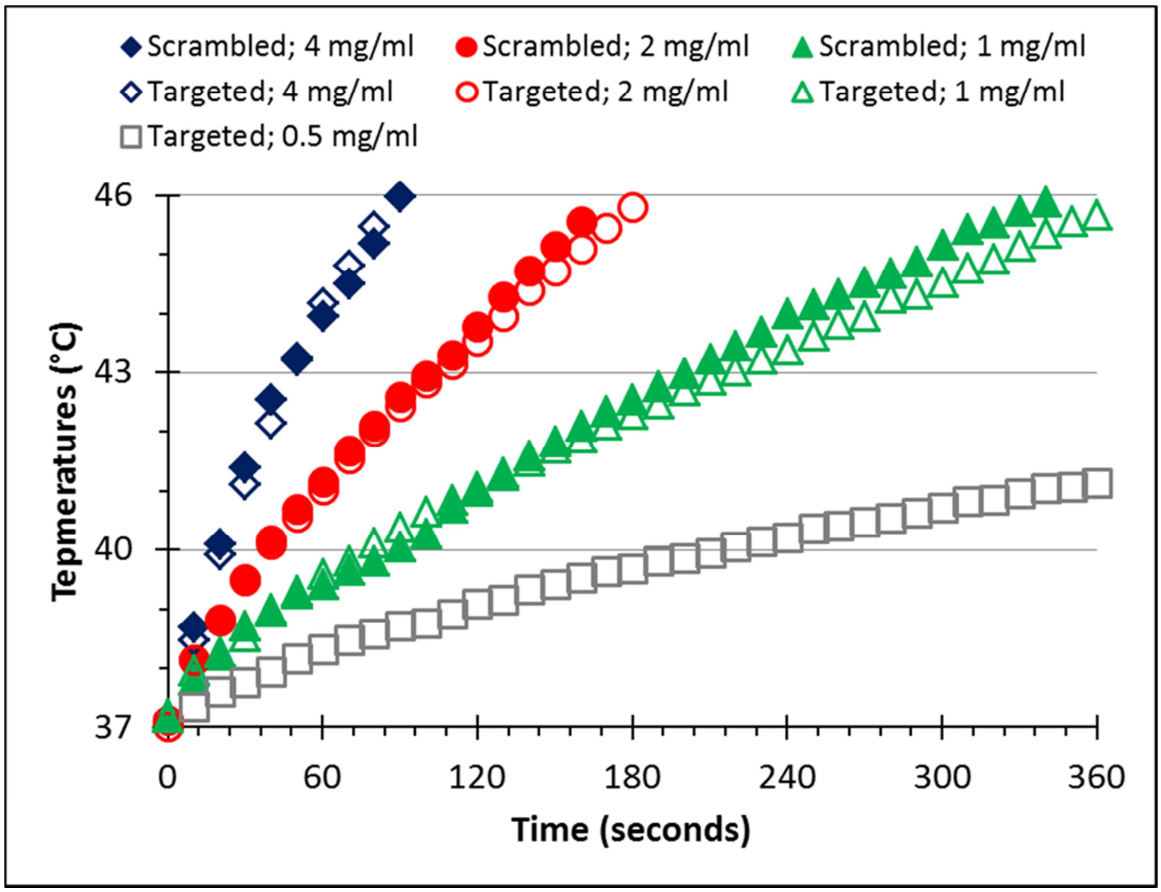

Figure 4.2 Heating rates of targeted and non-targeted SPIO nanoparticles. SPIO nanoparticles dispersions were placed in an alternating magnetic field of 6 kA/m and operating at a frequency of 386 kHz. The initial temperature was equilibrated to 37°C, and the temperature of SPIO NP dispersion was measured at 10 second intervals using a fluoroptic probe following the application of alternating magnetic field.

4.3.2. In vitro cell uptake and cell kill efficiency of targeted SPIO nanoparticles

Non-specific uptake of SPIO nanoparticles in A549 cells was determined as a function of time of incubation, concentration of serum in the culture medium and the incubation temperature. From these studies, an incubation time of 30 minutes and low

serum concentration were found to be optimal for minimizing the non-specific uptake of SPIO nanoparticles (Figure 4.3). Using these optimized parameters, an *in vitro* study was performed to determine the effect of EGFR targeting on cellular uptake of SPIO nanoparticles. Nanoparticle uptake into cells was 4.5-fold higher for the EGFR targeted formulation than that for the non-targeted control. Conjugation of scrambled peptide did not result in enhancement of particle uptake into cells, and the presence of excess targeting ligand decreased the cellular uptake of targeted nanoparticles, showing the specific role of EGFR in tumor cell uptake of targeted nanoparticles (Figure 4.4).

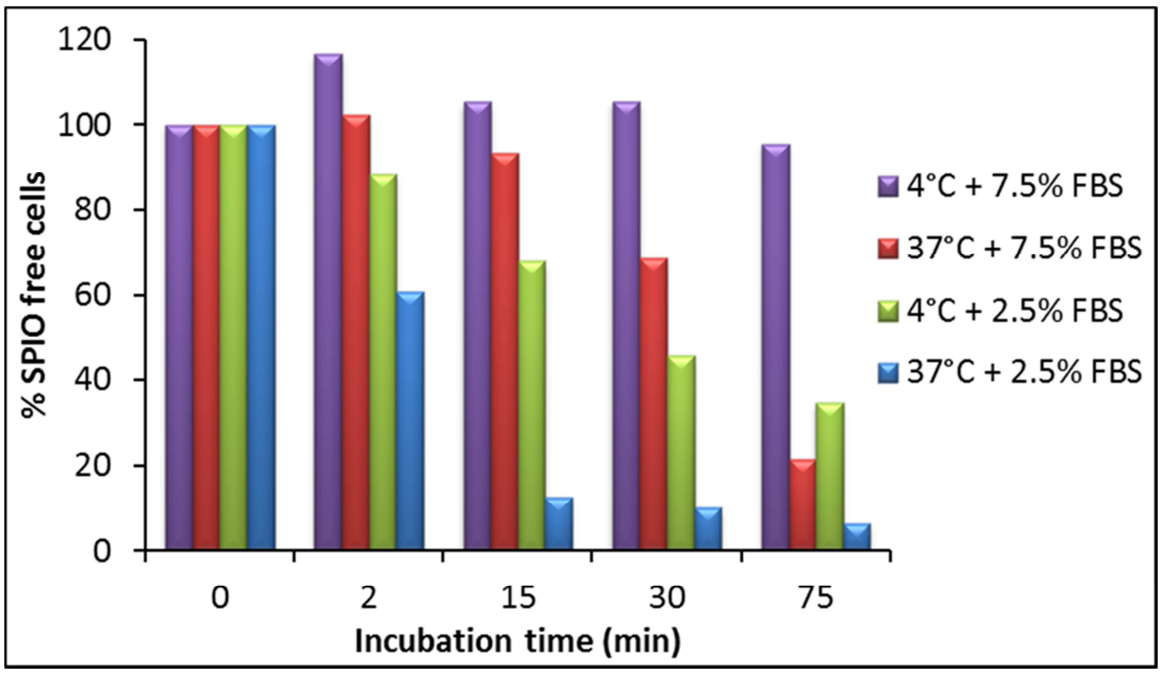

Figure 4.3 Non-specific uptake of SPIO nanoparticles by A549 cells. SPIO nanoparticles were incubated with A549 cells in medium containing 2.5% or 7.5% FBS at 4°C or 37°C for different durations. SPIO nanoparticle free cells were separated from the particle loaded cells by magnetic separation and assayed by MTS to determine the relative percent of particle free cells.

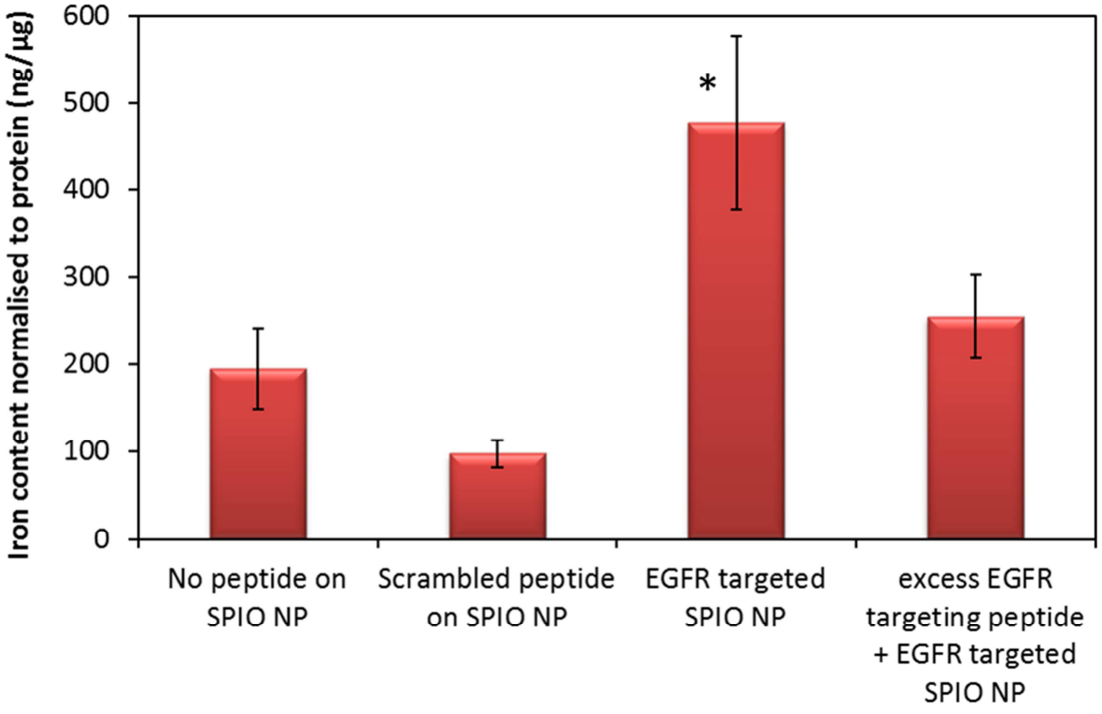

Figure 4.4 In vitro cell uptake study. SPIO nanoparticles bearing EGFR targeting peptide, scrambled peptide or no peptide on their surface were incubated with A549 cells at 4°C for 30 minutes, washed with PBS and further incubated at 37°C for 45 minutes. The specific role of EGFR in enhanced accumulation was confirmed by adding excess EGFR targeting peptide to competitively inhibit adhesion of targeted SPIO nanoparticles onto the cells. Iron content of the lysed cells were used to estimate cell uptake of SPIO nanoparticles. n = 3. * $p<0.05$.

To determine the effect of EGFR targeting on the effectiveness of magnetic hyperthermia, plated A549 cells were incubated with targeted or non-targeted SPIO nanoparticles, washed and subjected to AMF. Enhanced cellular accumulation of EGFR targeted SPIO nanoparticles could be visualized under the microscope as dark spots on the cells (Figure 4.5). Magnetic hyperthermia with targeted nanoparticles resulted in

greater number of cells taking up propidium iodide, indicating enhanced cell death with targeted SPIO nanoparticles (Figure 4.5).

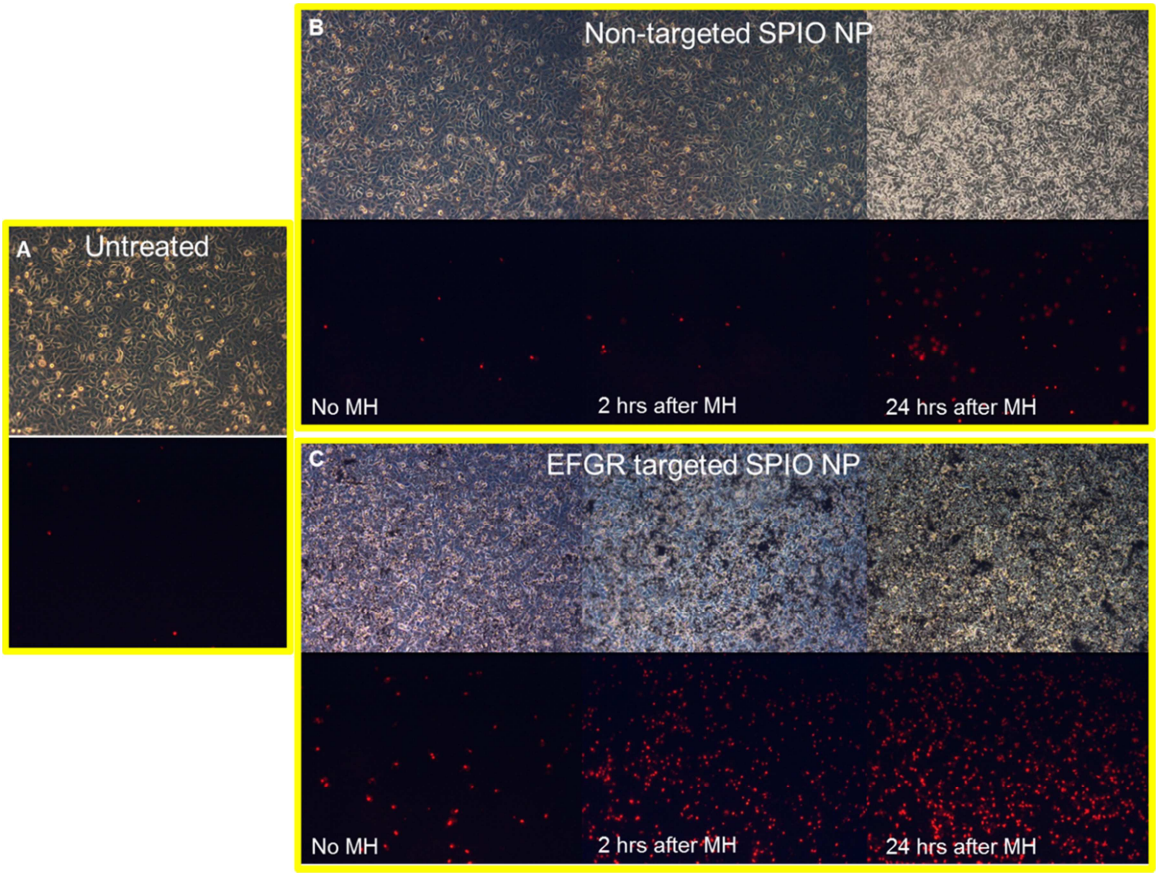

Figure 4.5 Effect of targeted magnetic hyperthermia on in vitro cell kill. Plated A549 cells were incubated with **(A)** no particles, **(B)** targeted or **(C)** non-targeted SPIO nanoparticles (similar to Figure 4.4) and subjected to magnetic hyperthermia (MH) for 30 min. PI was added immediately before MH treatment and the cells were imaged during different interval. The top pictures in each subpanel are the phase contrast microscopic image and the lower pictures are fluorescent microscopic images of PI positive cells. The cells in **(B)** and **(C)** were imaged before MH (left) (after particle incubation), 2 hours after MH (middle) and 24 hours after MH (right). Enhanced cellular concentration of SPIO nanoparticles (black dots in phase contrast mages) and increased PI positive population in EGFR targeted MH indicates the effectiveness of EGFR targeting on MH mediated cell kill.

4.3.3. In vivo lung deposition and retention after inhalation delivery

Ultrasonic atomization of SPIO nanoparticle dispersions resulted in aerosols with a MMAD of 1.1 ± 0.1 μm and GSD of 1.9 ± 0.1 (Figure 4.6). The iron oxide output rate was determined to be 270 ± 70 μg/min. The high iron oxide output and the MMAD size range point to the possibility of a high deposition of these aerosol particles in the mouse lung even with a relatively short exposure time.

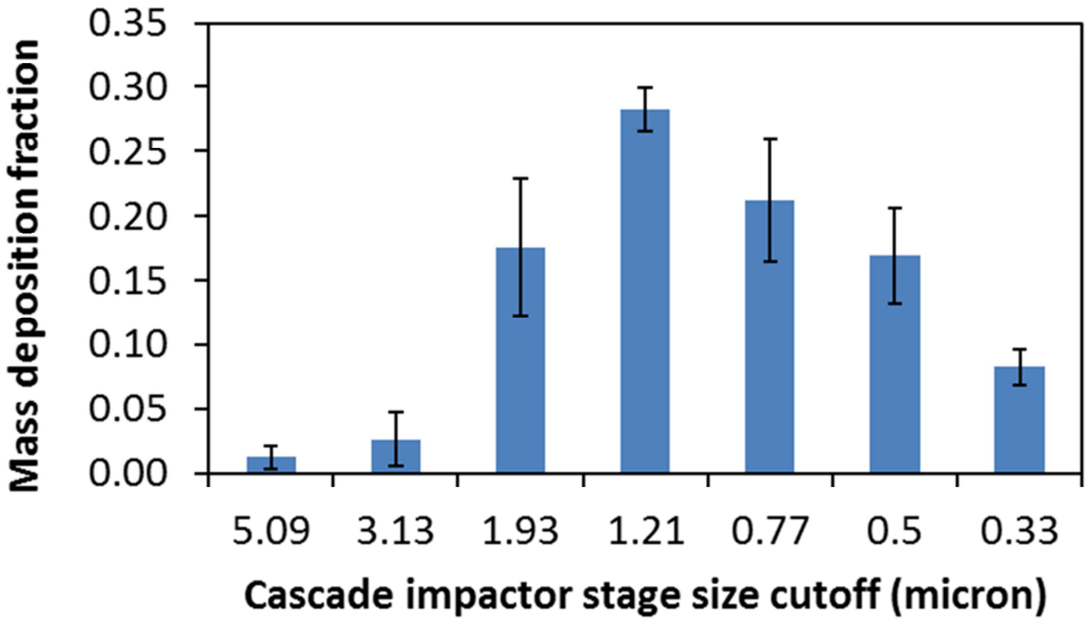

Figure 4.6 Inhalable SPIO particle aerodynamic size distribution. SPIO nanoparticle suspension was atomized by ultrasonic atomization technique, dried and passed through a seven stage cascade impactor. The mass of iron oxide deposited in stage was used to calculate the MMAD and GSD of the aerosol formulation.

Following aerosol exposure, iron oxide concentration in the lungs at 1 hour (Figure 4.7) was similar for targeted and non-targeted SPIO nanoparticles in tumor bearing lungs as well as for blank SPIO particles in healthy lungs, showing that the

presence of tumor did not affect the total deposition of particles. It also suggested that targeting does not affect the lung concentration immediately after the administration of particles. However, one week following inhalation, the lung concentration of non-targeted particles decreased while the level of targeted particles was almost constant, demonstrating the effectiveness of EGFR targeting in improving particle retention within tumor-bearing lungs.

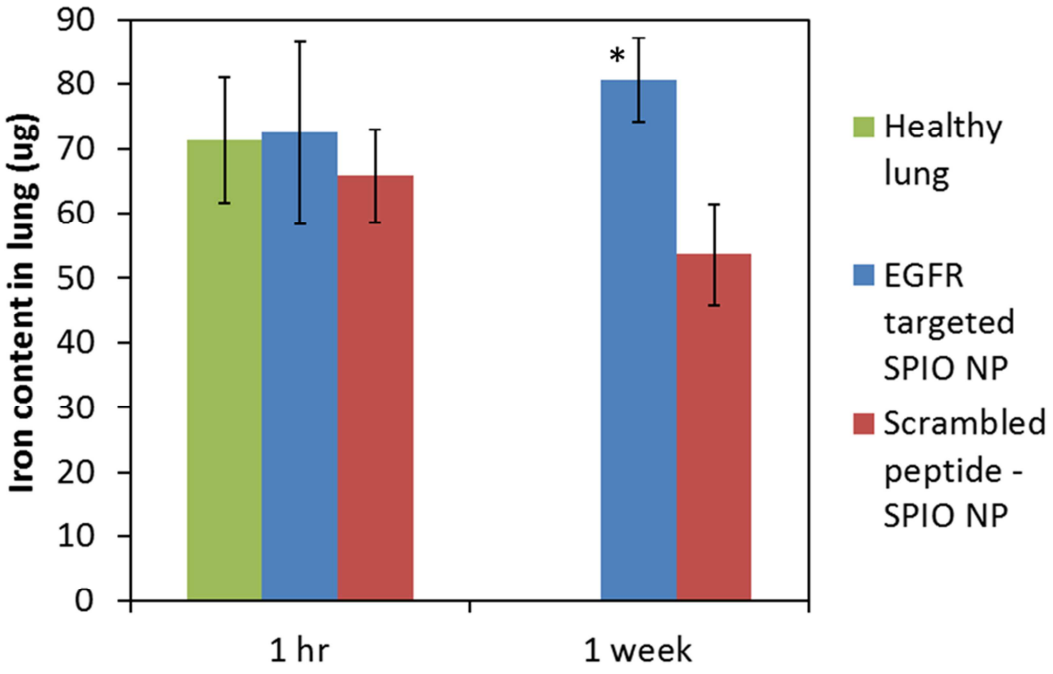

Figure 4.7 In vivo lung deposition and retention of SPIO nanoparticles after inhalation delivery. Healthy or A549 orthotopic tumor bearing mice were allowed to inhale the targeted or non-targeted SPIO nanoparticles for 30 minutes. The animals were euthanized 1 hour and 1 week after inhalation delivery and the lungs were assayed for their iron content. n = 4. * $P < 0.01$ compared to iron content in non-targeted group at 1 week after inhalation.

Inhalation delivery resulted in a homogenous distribution of SPIO nanoparticles throughout the lung (Figure 4.9). One week after inhalation, a significantly higher amount of Prussian blue staining was observed in the mice that received targeted particles compared to those that received non-targeted particles (Figure 4.8). In the former, the staining was observed in and around tumor cells, with near complete absence of particles from the healthy parts of the lung. In contrast, the latter group did not display much staining in either the tumor or the healthy regions of the lung (not shown).

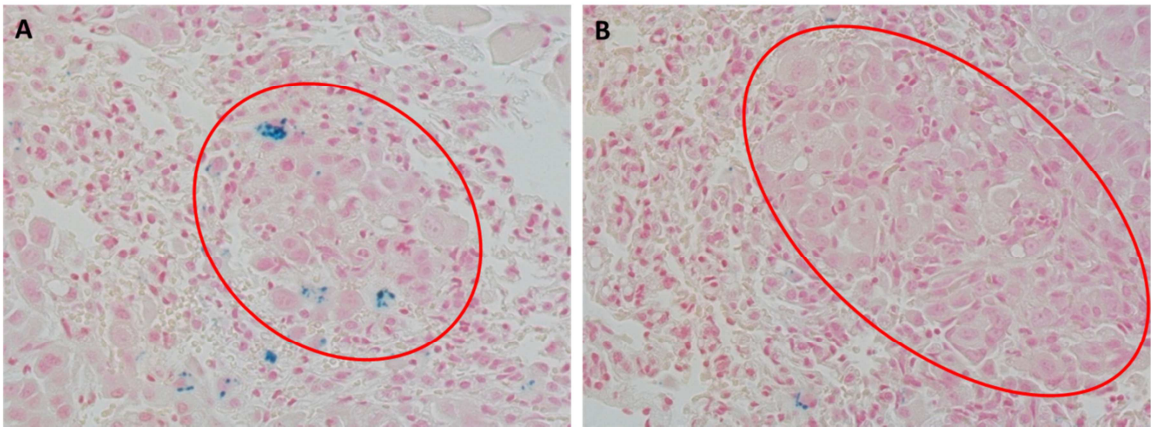

Figure 4.8 Prussian blue staining of lung tumor section after SPIO nanoparticle inhalation. One week after inhalation of **(A)** targeted or **(B)** non-targeted SPIO nanoparticles, mice were euthanized, lung collected, sectioned and stained with Prussian blue. Prussian blue binds with free iron to form a blue colored complex. The sections (100X magnification) show the presence of lung tumor nodules (red ovals) and SPIO nanoparticles in the tumor in EGFR targeted group.

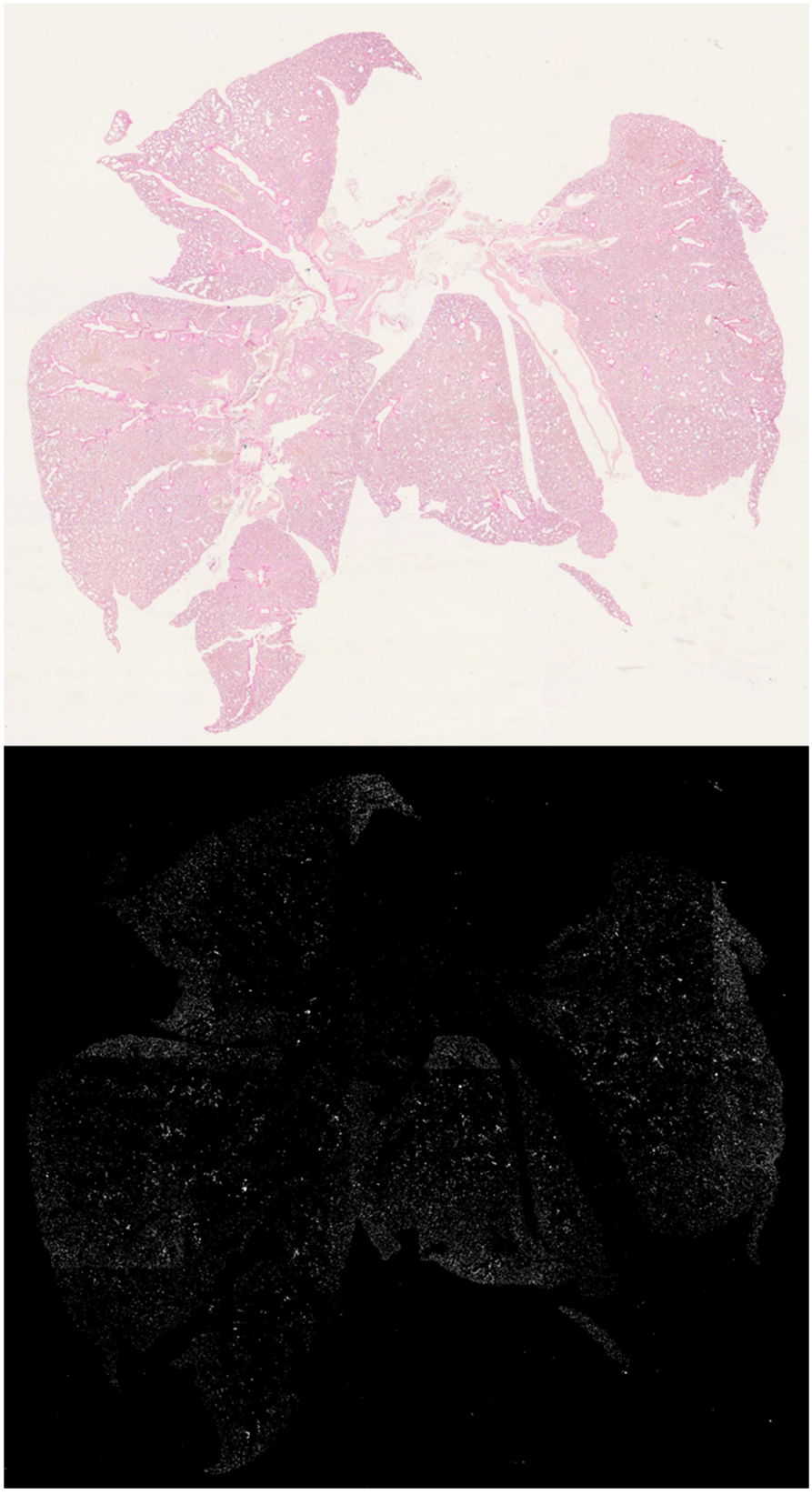

Figure 4.9 Distribution of SPIO nanoparticle in mouse lung after inhalation. One hour after inhalation of SPIO nanoparticles, animals were euthanized, lung collected, sectioned and stained with Prussian blue. Due to the difficulty in visualizing the Prussian blue staining in the top picture of the entire mouse lung, an image processing software (Image Pro Plus) was used to pseudo-color the Prussian blue stain white against a black background (bottom). The pseudo-color image demonstrates the homogenous distribution of SPIO nanoparticles post inhalation.

4.3.4. Biodistribution of SPIO nanoparticles after high dose instillation into lungs

To study the effect of elevated lung dose of SPIO nanoparticles on the overall body distribution, we used tracheal instillation. Unlike inhalation delivery, which restricts the dose deposited in mouse lungs to 72.5 ± 14.1 µg of magnetite, tracheal instillation allows for a higher dose (386 ± 95 µg of magnetite) to be delivered.

Following instillation, SPIO particles were mostly observed in the lungs after 1 hour, although some particles were also present in the stomach, due to the mucociliary clearance from the lung. There was no significant difference between the levels of targeted and non-targeted particles in the different organs 1 hour or 1 day after instillation. The concentration of both particles in blood and other organs (except lung) decreased 1 week after instillation compared to 1 hour or 1 day time points (Figure 4.10). On the contrary, while the lung concentration of non-targeted particles decreased over the period of 1 week, the level of targeted particles was fairly constant over 1 week. The final concentration of targeted particles was significantly higher (60%) than non-targeted particles one-week post instillation (Figure 4.11). In contrast to the high lung

concentration, the amount iron in the other tissues was virtually unchanged throughout the duration of the study and was not significantly different from the basal level of iron in the tissues of untreated animals (not shown). Overall lung concentration of SPIO nanoparticles, 1 week post-instillation, was significantly higher than any other tissue (Figure 4.12). This data suggested that pulmonary delivery of targeted SPIO nanoparticles can circumvent non-specific distribution into organs such as liver and spleen, which commonly receive the highest dose of intravenously administered therapeutics [239].

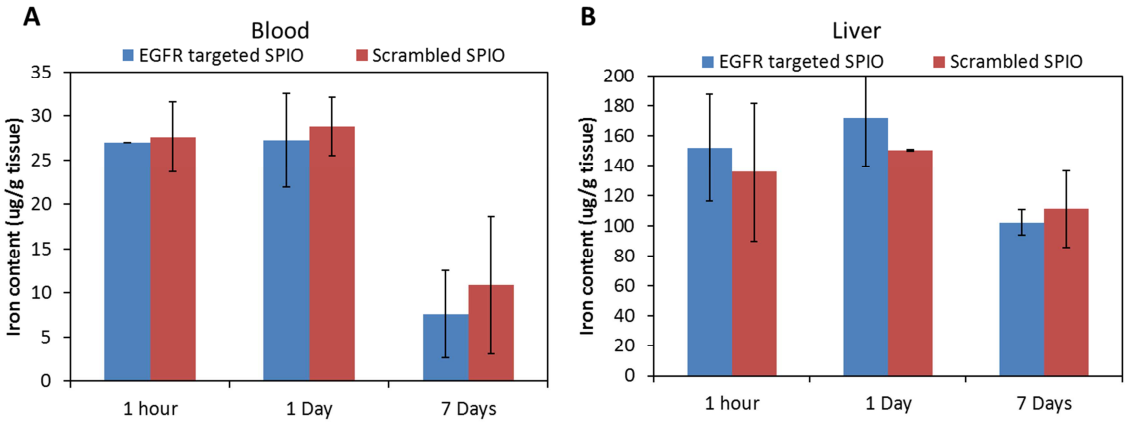

Figure 4.10 Iron content in tissues at different duration after SPIO nanoparticle instillation. Iron content in **(A)** blood and **(B)** liver after 1 hour, 1 day or 1 week after instillation of targeted or non-targeted SPIO nanoparticles. Iron concentration remained steady atleast till a day after instillation and decreased after a week. There was no significant effect of targeting on the iron levels in blood and liver. n = 4.

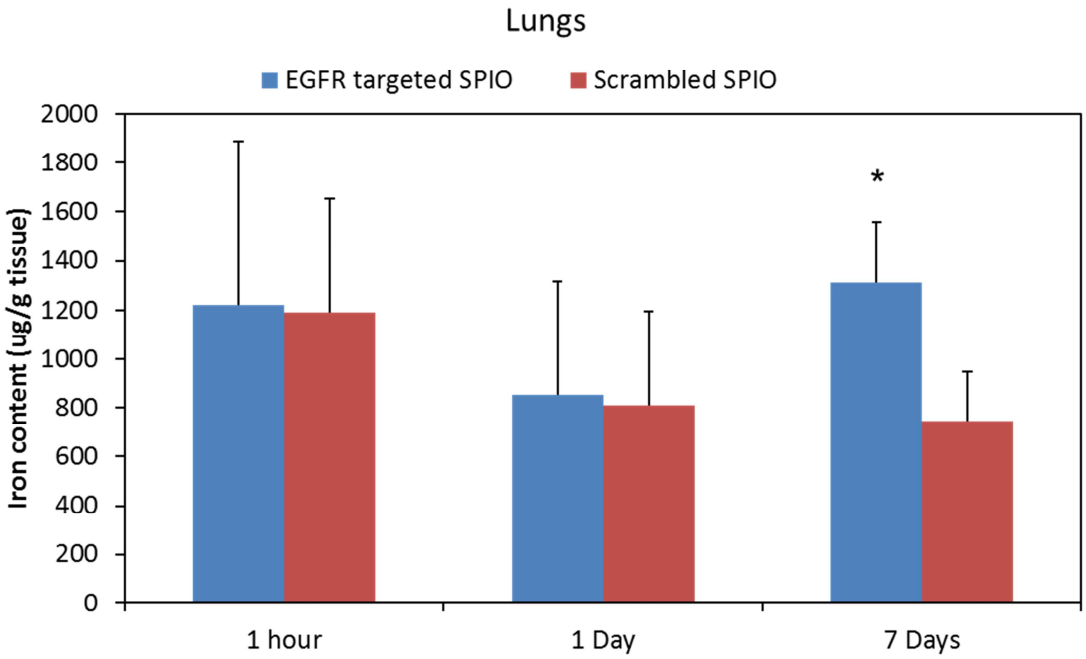

Figure 4.11 Iron content in the lungs at different duration after SPIO nanoparticle instillation. Iron content in lungs after 1 hour, 1 day or 1 week after instillation of targeted or non-targeted SPIO nanoparticles. EGFR targeting enhanced lung retention of SPIO nanoparticles over a week. n = 4. * $P < 0.05$

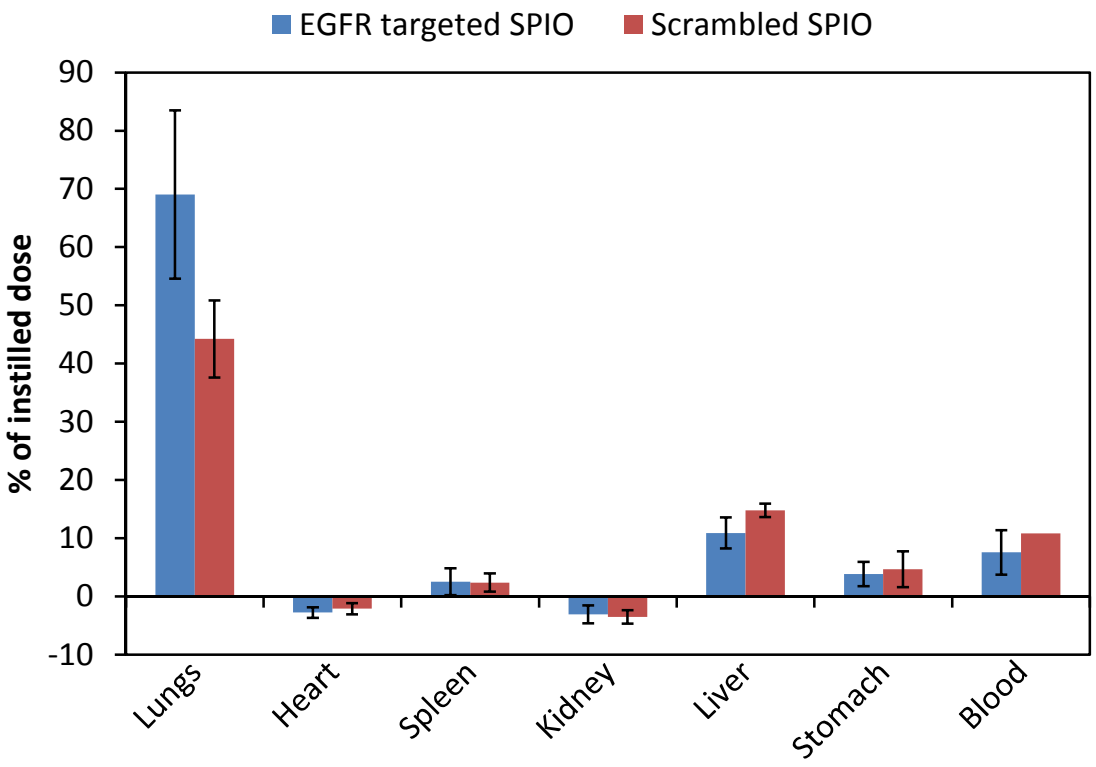

Figure 4.12 Distribution of SPIO nanoparticles 1 week post-instillation. Iron content in lungs, heart, spleen, kidneys, liver, stomach and blood are shown as a percent of instilled dose. Overall levels of iron in the organs were low except for the lungs. EGFR targeting enhanced lung retention of SPIO nanoparticles over a week. n = 4.

While both instillation and inhalation resulted in a significant increase in lung concentration of particles with EGFR targeting, the absolute amount of SPIO particles in the two cases were different. The lung iron content after instillation was 4.5 to 5-fold higher than that after inhalation (400 vs 80 µg for EGFR-targeted SPIO nanoparticles, Figure 4.7 and 4.11). This is likely due to the higher dose of particles delivered to the lung through instillation. However, aerosol delivery is a more convenient route of administration in humans than instillation. Additionally, inhalation resulted in a more

even distribution of the SPIO nanoparticles throughout the lungs at the time of administration (Figure 4.9) compared to instillation (Figure 4.13), where most of the instilled dose resided near the major airways, with almost no particles reaching the periphery.

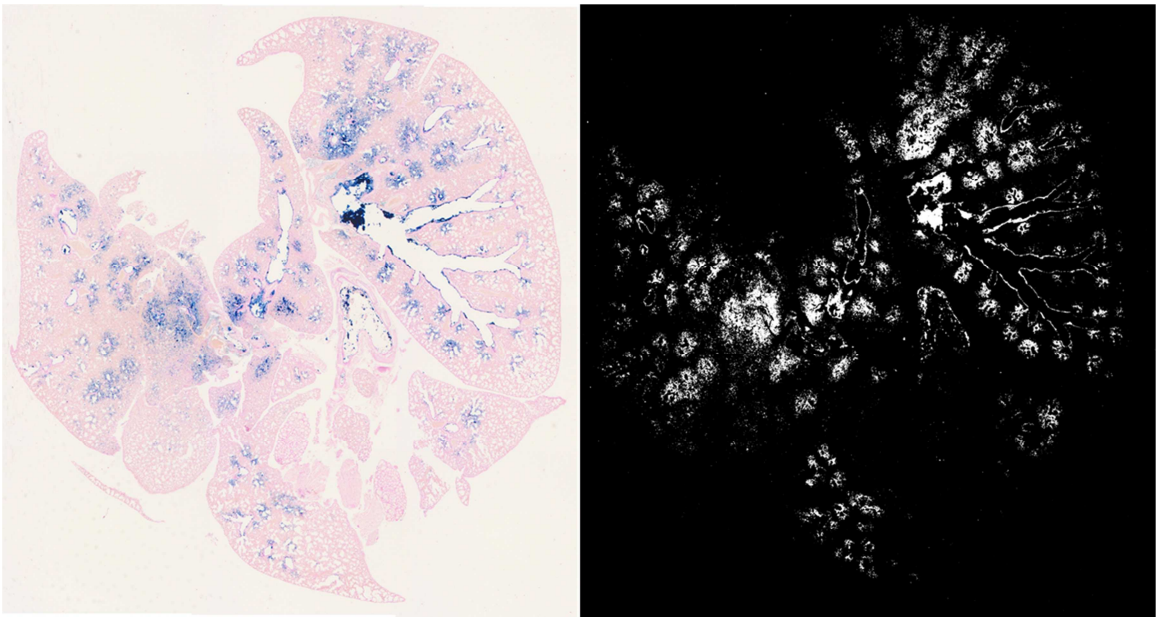

Figure 4.13 Distribution of SPIO nanoparticles in mouse lung after instillation. One hour after instillation of SPIO nanoparticles, animals were euthanized, lung collected, sectioned and stained with Prussian blue. Left figure shows the Prussian blue stained section of the entire lung and the right figure is a pseudo-color image of the Prussian blue stain (white) against a black background (right). The particles are deposited primarily along the major airways and the peripheral regions of the lungs are almost entirely devoid of SPIO staining.

4.3.5. In vivo efficacy after inhalation

Magnetic hyperthermia using non-targeted SPIO particles resulted in an insignificant decrease in lung tumor bioluminescence ($p > 0.05$) relative to that in animals

that received the same particles but were not exposed to AMF. Targeted SPIO nanoparticles mediated hyperthermia showed significantly lower lung tumor bioluminescence ($p < 0.05$) (Figure 4.14). The lung weights at the end of the study agreed with the bioluminescence data; magnetic hyperthermia with targeted particles resulted in a significantly lower final lung weight compared to the other groups (Figure 4.15).

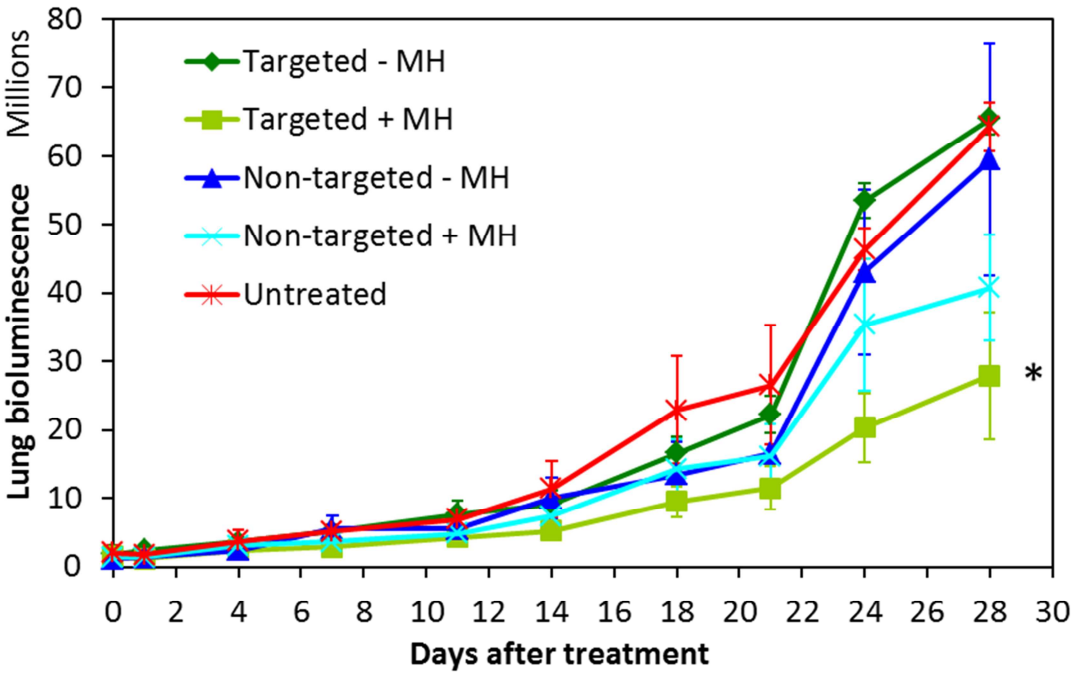

Figure 4.14 In vivo efficacy of targeted magnetic hyperthermia in an orthotopic lung tumor model. Orthotopic lung tumor bearing mice were allowed to inhale targeted or non-targeted SPIO nanoparticles. After 1 week, 6 animals from each group were subjected to magnetic hyperthermia (MH) for 30 minutes. Lung tumor bioluminescence was monitored over a period of 1 month. Data shown = mean ± SD. n = 6. * $P < 0.05$

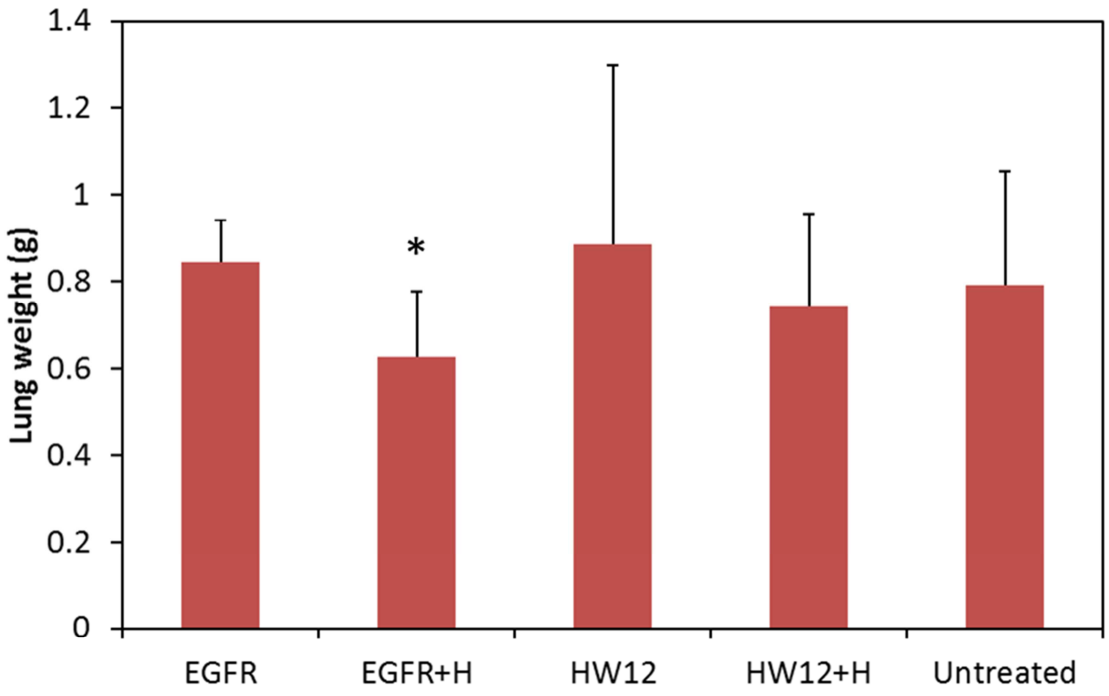

Figure 4.15 Lung weight at the end of efficacy study (Figure 4.14). Lungs were collected at the end of the efficacy study (1 month after magnetic hyperthermia) and weighed. Data shown = Mean ± SD. n = 6. $P < 0.05$ compared to unheated control.

These *in vivo* results thus confirm that EGFR targeting enhances the tumor concentration of SPIO nanoparticles, which translated into more effective tumor cell kill. In addition, the treated mice showed no signs of distress over the duration of the study (30 days after magnetic hyperthermia treatment), suggesting that this procedure does not result in acute systemic toxicity or damage to healthy lung tissue. Additionally, the dose of particles that could be delivered to the tumor by inhalation was limited by the small lung volume and the obligate nose-breathing of mice [240]. A similar approach can be

expected to be more effective in humans, because a higher deposition can be achieved with inhalation through the oral cavity and control of the respiration.

4.4. Discussion

Magnetic hyperthermia, which involves the use of superparamagnetic substances to generate heat through application of an external AMF, is a non-invasive approach for lung tumor ablation. The relatively inert nature of the magnetic substances in the absence of magnetic field and their efficacy in the presence of AMF makes this technique highly suitable for achieving an on-demand response. Magnetic hyperthermia is particularly suitable for the treatment of lung cancer since unlike the abdomen, the thoracic region, where the external AMF can be easily focused, is only inhabited by the lungs and the heart. Additionally, lungs are filled with air, which act as a poor conductor of heat. Thus, the heat generated by the particles in the lungs is less likely to affect the surrounding organs such as the heart. Finally, studies have shown that normal, non-malignant cells are more resilient to heat damage than tumor cells [241], thereby minimizing the chances of damage to healthy lung tissue. Recent reports have suggested that magnetic hyperthermia is effective in murine subcutaneous lung tumor models [242,243]. However, in spite of the promise of a highly effective treatment option, no studies have so far assessed the effectiveness of magnetic hyperthermia in an orthotopic lung tumor model.

Although the lung is a highly perfused organ, intravenous delivery of anticancer therapeutics targeted to the lung results in broad, non-specific distribution of the therapeutic agents to normal organs, resulting in severe systemic side effects [244]. While

many solid tumors are not amenable to local delivery, lung tumors of the epithelial origin can potentially be accessed by inhalation route. This allows for maximizing the concentration of the therapeutic agent in the target organ, i.e., the lungs, while minimizing exposure to other normal organs. Lung clearance of particulates into systemic circulation is primarily attributed to the alveolar macrophages, which leads to a lower blood concentration of the therapeutics than through intravenous administration. Several reports have shown that pulmonary delivery improves retention of therapeutic agents in the lungs while limiting their concentration in the blood thereby reducing their levels in the healthy organs [239,245]. Our studies show that lung delivery through either instillation or inhalation results in therapeutically effective concentrations of SPIO nanoparticles in lungs with minimal exposure to other organs. An hour after instillation of SPIO nanoparticles, the average lung concentration of iron oxide was 1.2 mg/g of tissue. In contrast, the average liver and blood concentration were 130 µg/g and 27 µg/g of tissue, respectively. The other organs including spleen, kidney and heart contained less than 2% of the instilled dose. This demonstrates that inhalation delivery is an effective means to enhance local concentration of therapeutics into the lungs.

Following inhalation delivery, it is expected that nanoparticles would be distributed to both the malignant and healthy regions of the lungs. The presence of targeting ligand on the surface is expected to enable nanoparticles to bind to the tumor cells, allowing for greater retention in the tumor tissue. Thus, greater retention within the tumor tissue and clearance from normal tissue is expected to eventually result in relatively higher levels of nanoparticles in the tumor. Application of AMF during this

window would allow for tumor-specific induction of hyperthermia. In our studies, tumor cell specificity was achieved by targeting SPIO nanoparticles to EGFR, which is overexpressed in NSCLC tumors [140-142]. Monoclonal antibodies against EGFR (cetuximab) and EGFR tyrosine kinase inhibitors are clinically used for lung cancer. Thus, EGFR is an attractive target in lung cancer. We used a previously reported 11-residue peptide ligand for targeting EGFR [246]. This peptide binds specifically and efficiently to EGFR (dissociation constant of ~20 nM), but has much lower mitogenic activity than EGF [143]. We found that EGFR targeting enhanced the *in vitro* accumulation of targeted SPIO nanoparticles into A549 cells by 450% compared to non-targeted particles. Aerosolized SPIO particles were directed to the periphery of the lung by controlling the aerodynamic size of SPIO aggregates. One hour after inhalation, the amount of the targeted or non-targeted particles was similar in tumor-bearing or healthy lungs (about 70 µg iron oxide). However, following muco-ciliary clearance from the lung (1 week after inhalation delivery), the level of non-targeted SPIO nanoparticles was significantly lower than that of targeted particles. This difference could be attributed to the presence of tumor targeting ligand on the surface. Thus, by combining receptor targeting with inhalation delivery, superior tumor selectivity can be achieved.

There are several challenges in the design of an effective inhalation system, which can deposit a high dose to the peripheral regions of the lung. Mice are obligatory nose breathers, with a small inhalation volume (~24.5 ml/min). This restricts the rate of delivery of therapeutics into the lungs. The dose delivered can, however, be controlled by changing the concentration of the aerosol generated (mass of aerosol/ volume of air) and

the aerodynamic diameter of the aerosol. An MMAD of 1 µm has been shown to result in the highest concentration of the therapeutic agents in all lobes of mouse lungs [122], yielding a deposition percent (ratio of mass deposited in the lungs to total mass inhaled) of about 10 % [123,124]. In our studies, we obtained a deposition of nearly 15 % (Supp fig.) with the 1.1 µm MMAD SPIO nanoparticles. The elevated deposition fraction was probably attributed to pre-acclimatization of the mice to the inhalation chambers and the prolonged exposure (30 min), which prevented undue stress and uneven breathing pattern caused by short aerosol exposures. This fraction is amenable to further enhancement by using magnetic deposition [124] or micro-spraying technique [125], which can increase the deposition fraction of SPIO nanoparticles by several folds.

The effectiveness of targeted magnetic hyperthermia was evaluated in an orthotopic mouse lung tumor model. Intravenous injection of A549 cells led to the development of lung tumors, whose bioluminescence scaled with the size of the tumor. Lung tumors could be identified at a bioluminescence level of 1 X 10^5 photons/second and the tumor burden reached 90% of the lung volume at 5 X 10^8 photons/sec. Using an optimized aerosol formulation of targeted SPIO nanoparticles, we could achieve therapeutic doses of SPIO nanoparticles in the tumors. A single magnetic hyperthermia regimen was effective in reducing the tumor growth rate over a month compared to the non-targeted or non-treated control. In addition, the treated mice showed no signs of distress over the duration of the study (30 days after magnetic hyperthermia treatment), suggesting that this procedure does not result in acute systemic toxicity or damage to healthy lung tissue.

Due to their epithelial nature, lung tumors fill up the alveolar region and thus, most tumors are not exposed to the circulating airways. This poses a challenge to the success of the nanoparticle system. In spite of enhanced retention of targeted SPIO nanoparticles in the tumor, not all tumor cells possessed particles and therefore would not receive magnetic hyperthermia therapy. As a result, the treatment showed a significant delay in tumor growth but not complete eradication. However, this problem could potentially be addressed by using agents that normalize the tumor extracellular matrix and enhance the penetration of nanoparticles into the tumor [247,248]. Additionally, SPIO nanoparticle mediated magnetic hyperthermia may be highly effective as an adjuvant therapy for killing isolated tumors cells left behind after surgical resection of the lung tumors.

4.5. Conclusions

Inhalation delivery of EGFR-targeted SPIO nanoparticles was investigated in this study as a potential approach for lung cancer treatment. Our studies show that EGFR targeting enhances tumor retention of SPIO nanoparticles while minimizing systemic exposure. Tracheal instillation allowed for high doses of SPIO nanoparticles to be administered, however, aerosol delivery resulted in better intra-tumoral distribution. Magnetic hyperthermia using targeted SPIO nanoparticles resulted in a significant inhibition of *in vivo* tumor growth. Overall this work highlights the potential for developing magnetic hyperthermia as an effective anticancer treatment modality for the treatment of non-small cell lung cancer.

Chapter 5

SUMMARY

Poor response rates and survival with current treatments indicates an urgent need for the development an effective means to treat NSCLC. In this study, an aerosol-based, tumor-targeted SPIO nanoparticles system was used to induce highly selective magnetic hyperthermia for the treatment of lung cancer.

The objective of the first study was to identify the mechanism of cell kill by magnetic hyperthermia, with a particular focus on the effect of aggregation state of SPIO nanoparticles. Overabundance of salt and protein in biological milieu often favors aggregation of inorganic nanoparticles. Studies in Chapter 2 demonstrate that the particle size of aggregates affects the therapeutic performance of SPIO nanoparticles. Well-dispersed SPIO nanoparticles induced apoptosis, similar to that observed with conventional hyperthermia. Sub-micron size aggregates (hydrodynamic diameter less than 500 nm), on the other hand, induced temperature-dependent autophagy through generation of ROS. Micron size aggregates (larger than 1 μm) caused rapid membrane damage and acute cell kill even in the absence of temperature elevation, suggesting a temperature-independent mechanism of action, likely due to physical motion of the aggregates in AMF. Interestingly, solid micron size iron oxide particles did not exhibit enhanced acute cell kill in the absence of temperature elevation, thus confirming the importance of the smaller superparamagnetic iron oxide cores and the micron size of the final aggregate in this process. This novel mechanism of cell kill induced by micro aggregates translated into effective *in vivo* tumor growth inhibition. Overall this work

highlighted the potential for developing highly effective anticancer therapeutics through simple yet often overlooked modifications of delivery systems such as their state of aggregation.

This is a very important finding especially in the field of magnetic hyperthermia. One of the primary limitations of this technique is the necessity of a "sufficient" quantity of magnetic particles at the site of action to successfully induce heat-mediated cell death. Depending on the heating potential of the magnetic particles used, the quantity required is often in the range of a few milligrams per gram (or cm^3) of tumor. Studies in Chapter 2 suggested that for a well-designed SPIO nanoparticle system, the distribution of these particles in the tumor, and not their amount, will be more critical for the effectiveness of magnetic hyperthermia.

CSCs are considered to play important roles in tumor drug resistance and recurrence. Studies in Chapter 3 evaluated the susceptibility of CSCs to magnetic hyperthermia. Our studies showed that CSCs and non-CSCs are equally susceptible to cell death induced by a mix of sub-micron and micron sized SPIO aggregate mediated magnetic hyperthermia. Further, magnetic hyperthermia induced both acute necrosis and a slower, ROS-mediated cell-death in treated cells. Some of the cell kill events appeared to be temperature-independent, although elevated temperatures appeared to amplify those effects. Overall, the results of this study suggested the potential for effective CSC eradication by magnetic hyperthermia.

This observation is of particular importance for the treatment of lung cancer where tumor recurrence is common in the first five years after diagnosis. While systemic

chemotherapy is used to treat circulating tumor cells, clinical results and numerous pre – clinical studies have shown that CSCs are resistant to chemotherapy. Thus, treatment options that completely eradicate the tumors including the CSCs can potentially decrease the risk of tumor recurrence. Studies in Chapter 3 demonstrate, through numerous *in vitro* and *in vivo* CSC assays, that magnetic hyperthermia can affect these cells in manifold ways. However, future studies need to be performed to investigate the effect of magnetic hyperthermia on *in vivo* tumor growth and tumor recurrence.

Inhalation delivery of EGFR-targeted SPIO nanoparticles was investigated, in the final study, as a potential approach for lung cancer treatment. Studies in Chapter 4 demonstrate that EGFR targeting enhances tumor retention of SPIO nanoparticles while minimizing systemic exposure. About 50 – 60% higher lung concentration of targeted SPIO nanoparticles was seen after different routes of lung delivery – tracheal instillation and inhalation. Tracheal instillation allowed for high doses of SPIO nanoparticles to be administered, while aerosol delivery resulted in better intra-tumoral distribution. Magnetic hyperthermia using inhaled targeted SPIO nanoparticles resulted in a significant inhibition of *in vivo* tumor growth.

Though these results are highly encouraging, it must be noted that the tumor progression was slower but not completely inhibited. One of the factors responsible for this incomplete response is the nature of lung tumor formation. Due to their epithelial nature, lung tumors fill up the alveolar region and thus, most tumors are not exposed to the circulating airways. Thus, inspite of enhanced retention of targeted SPIO nanoparticles, not all tumor cells had particles in them and therefore did not receive

magnetic hyperthermia therapy. A potential solution for this problem is co-administration agents that normalize the tumor extracellular matrix and enhance the penetration of nanoparticles into the tumor.

Another prospective application of SPIO nanoparticle mediated magnetic hyperthermia is as an adjuvant therapy for killing isolated tumors cells left behind after surgical resection of the lung tumors. While larger tumor nodules can be surgically removed, isolated cells often remain undetected by current imaging techniques. Due to their smaller dimensions, they are unlikely to occlude the whole alveolar space and can therefore be treated with inhaled targeted SPIO nanoparticle mediated magnetic hyperthermia.

Overall, this work highlights the potential for developing magnetic hyperthermia as an effective anticancer treatment modality for the treatment of NSCLC.

BIBLIOGRAPHY

1. Namduri, H.and Nasrazadani, S. Quantitative analysis of iron oxides using Fourier transform infrared spectrophotometry. *Corrosion Science* **2008**, 50, 2493-2497.
2. *Cancer Trends Progress Report – 2011/2012 Update*. August, 2012, National Cancer Institute, NIH, DHHS, Bethesda, MD.
3. Society, A.C. **2009**.
4. Jemal, A.; Siegel, R.; Ward, E.; Hao, Y.; Xu, J.; Murray, T.and Thun, M.J. Cancer statistics, 2008. *CA Cancer J Clin* **2008**, 58, 71-96.
5. Parkin, D.M.; Bray, F.; Ferlay, J.and Pisani, P. Global cancer statistics, 2002. *CA Cancer J Clin* **2005**, 55, 74-108.
6. Alberg, A.J.; Brock, M.V.and Samet, J.M. Epidemiology of lung cancer: looking to the future. *J Clin Oncol* **2005**, 23, 3175-3185.
7. Vineis, P.; Airoldi, L.; Veglia, F.; Olgiati, L.; Pastorelli, R.; Autrup, H.; Dunning, A.; Garte, S.; Gormally, E.; Hainaut, P.; Malaveille, C.; Matullo, G.; Peluso, M.; Overvad, K.; Tjonneland, A.; Clavel-Chapelon, F.; Boeing, H.; Krogh, V.; Palli, D.; Panico, S.; Tumino, R.; Bueno-De-Mesquita, B.; Peeters, P.; Berglund, G.; Hallmans, G.; Saracci, R.and Riboli, E. Environmental tobacco smoke and risk of respiratory cancer and chronic obstructive pulmonary disease in former smokers and never smokers in the EPIC prospective study. *BMJ* **2005**, 330, 277.
8. Wakelee, H.A.; Bernardo, P.; Johnson, D.H.and Schiller, J.H. Changes in the natural history of nonsmall cell lung cancer (NSCLC)--comparison of outcomes and characteristics in patients with advanced NSCLC entered in Eastern Cooperative Oncology Group trials before and after 1990. *Cancer* **2006**, 106, 2208-2217.
9. Yang, P.; Allen, M.S.; Aubry, M.C.; Wampfler, J.A.; Marks, R.S.; Edell, E.S.; Thibodeau, S.; Adjei, A.A.; Jett, J.and Deschamps, C. Clinical features of 5,628

primary lung cancer patients: experience at Mayo Clinic from 1997 to 2003. *Chest* **2005**, 128, 452-462.

10. Aberle, D.R.and Brown, K. Lung cancer screening with CT. *Clin Chest Med* **2008**, 29, 1-14, v.
11. Ahrendt, S.A.; Hu, Y.; Buta, M.; McDermott, M.P.; Benoit, N.; Yang, S.C.; Wu, L.and Sidransky, D. p53 mutations and survival in stage I non-small-cell lung cancer: results of a prospective study. *J Natl Cancer Inst* **2003**, 95, 961-970.
12. Xu, H.J.; Quinlan, D.C.; Davidson, A.G.; Hu, S.X.; Summers, C.L.; Li, J.and Benedict, W.F. Altered retinoblastoma protein expression and prognosis in early-stage non-small-cell lung carcinoma. *J Natl Cancer Inst* **1994**, 86, 695-699.
13. Fontanini, G.; Vignati, S.; Boldrini, L.; Chine, S.; Silvestri, V.; Lucchi, M.; Mussi, A.; Angeletti, C.A.and Bevilacqua, G. Vascular endothelial growth factor is associated with neovascularization and influences progression of non-small cell lung carcinoma. *Clin Cancer Res* **1997**, 3, 861-865.
14. Han, H.; Silverman, J.F.; Santucci, T.S.; Macherey, R.S.; d'Amato, T.A.; Tung, M.Y.; Weyant, R.J.and Landreneau, R.J. Vascular endothelial growth factor expression in stage I non-small cell lung cancer correlates with neoangiogenesis and a poor prognosis. *Ann Surg Oncol* **2001**, 8, 72-79.
15. Gessner, C.; Rechner, B.; Hammerschmidt, S.; Kuhn, H.; Hoheisel, G.; Sack, U.; Ruschpler, P.and Wirtz, H. Angiogenic markers in breath condensate identify non-small cell lung cancer. *Lung Cancer* **2009**.
16. LoCicero, J., 2nd. Minimally invasive thoracic surgery, video-assisted thoracic surgery and thoracoscopy. *Chest* **1992**, 102, 330-331.
17. Reckzeh, B.; Merte, H.; Pfluger, K.H.; Pfab, R.; Wolf, M.and Havemann, K. Severe lymphocytopenia and interstitial pneumonia in patients treated with paclitaxel and simultaneous radiotherapy for non-small-cell lung cancer. *J Clin Oncol* **1996**, 14, 1071-1076.
18. Cortes, J.; Rodriguez, J.; Calvo, E.; Gurpide, A.; Garcia-Foncillas, J.; Salgado, E.; Aramendia, J.M.; Lopez-Picazo, J.M.; Hernandez, B.; Hidalgo, R.; Aristu, J.J.; Brugarolas, A.and Martin-Algarra, S. Paclitaxel, cisplatin, and vinorelbine

combination chemotherapy in metastatic non-small-cell lung cancer. *Am J Clin Oncol* **2004**, 27, 299-303.

19. Comella, P.; Frasci, G.; Panza, N.; Manzione, L.; Lorusso, V.; Di Rienzo, G.; Cioffi, R.; De Cataldis, G.; Maiorino, L.; Bilancia, D.; Nicolella, G.; Natale, M.; Carpagnano, F.; Pacilio, C.; De Lena, M.; Bianco, A.and Comella, G. Cisplatin, gemcitabine, and vinorelbine combination therapy in advanced non-small-cell lung cancer: a phase II randomized study of the Southern Italy Cooperative Oncology Group. *J Clin Oncol* **1999**, 17, 1526-1534.
20. Georgoulias, V.; Androulakis, N.; Bouros, D.; Kouroussis, C.; Chatzakis, K.; Papadakis, M.; Apostopoloulou, F.; Georgopoulou, T.; Kotsakis, T.; Souklakos, J.; Hatzidaki, D.; Vlachonikolis, J.and Panagos, G. Combination chemotherapy with docetaxel, vinorelbine and cisplatin as first-line treatment of advanced non-small-cell lung cancer: a multicenter phase II study of the Greek Cooperative Group for Lung Cancer. *Lung Cancer* **1998**, 21, 213-220.
21. Berthaud, P.; Le Chevalier, T.; Ruffie, P.; Baldeyrou, P.; Arriagada, R.; Besson, F.and Tursz, T. Phase I-II study of vinorelbine (Navelbine) plus cisplatin in advanced non-small cell lung cancer. *Eur J Cancer* **1992**, 28A, 1863-1865.
22. Scagliotti, G.V.; Parikh, P.; von Pawel, J.; Biesma, B.; Vansteenkiste, J.; Manegold, C.; Serwatowski, P.; Gatzemeier, U.; Digumarti, R.; Zukin, M.; Lee, J.S.; Mellemgaard, A.; Park, K.; Patil, S.; Rolski, J.; Goksel, T.; de Marinis, F.; Simms, L.; Sugarman, K.P.and Gandara, D. Phase III study comparing cisplatin plus gemcitabine with cisplatin plus pemetrexed in chemotherapy-naive patients with advanced-stage non-small-cell lung cancer. *J Clin Oncol* **2008**, 26, 3543-3551.
23. Kreuter, M.; Vansteenkiste, J.; Griesinger, F.; Hoffmann, H.; Dienemann, H.; De Leyn, P.and Thomas, M. Trial on refinement of early stage non-small cell lung cancer. Adjuvant chemotherapy with pemetrexed and cisplatin versus vinorelbine and cisplatin: the TREAT protocol. *BMC Cancer* **2007**, 7, 77.
24. Karapanagiotou, E.M.; Boura, P.G.; Papamichalis, G.; Konstantinou, M.; Sepsas, E.; Chamalakis, G.; Simsiris, P.; Gkiozos, I.and Syrigos, K.N. Carboplatin-

pemetrexed adjuvant chemotherapy in resected non-small cell lung cancer (NSCLC): a phase II study. *Anticancer Res* **2009**, 29, 4297-4301.

25. Ramalingam, S.and Belani, C.P. State-of-the-art chemotherapy for advanced non-small cell lung cancer. *Semin Oncol* **2004**, 31, 68-74.
26. Belani, C.P. Single agents in the second-line treatment of non-small cell lung cancer. *Semin Oncol* **1998**, 25, 10-14.
27. Jain, R.K. Normalizing tumor vasculature with anti-angiogenic therapy: a new paradigm for combination therapy. *Nat Med* **2001**, 7, 987-989.
28. Sandler, A.; Gray, R.; Perry, M.C.; Brahmer, J.; Schiller, J.H.; Dowlati, A.; Lilenbaum, R.and Johnson, D.H. Paclitaxel-carboplatin alone or with bevacizumab for non-small-cell lung cancer. *N Engl J Med* **2006**, 355, 2542-2550.
29. Mendelsohn, J.and Baselga, J. Status of epidermal growth factor receptor antagonists in the biology and treatment of cancer. *J Clin Oncol* **2003**, 21, 2787-2799.
30. Lynch, T.J.; Bell, D.W.; Sordella, R.; Gurubhagavatula, S.; Okimoto, R.A.; Brannigan, B.W.; Harris, P.L.; Haserlat, S.M.; Supko, J.G.; Haluska, F.G.; Louis, D.N.; Christiani, D.C.; Settleman, J.and Haber, D.A. Activating mutations in the epidermal growth factor receptor underlying responsiveness of non-small-cell lung cancer to gefitinib. *N Engl J Med* **2004**, 350, 2129-2139.
31. Pao, W.; Miller, V.; Zakowski, M.; Doherty, J.; Politi, K.; Sarkaria, I.; Singh, B.; Heelan, R.; Rusch, V.; Fulton, L.; Mardis, E.; Kupfer, D.; Wilson, R.; Kris, M.and Varmus, H. EGF receptor gene mutations are common in lung cancers from "never smokers" and are associated with sensitivity of tumors to gefitinib and erlotinib. *Proc Natl Acad Sci U S A* **2004**, 101, 13306-13311.
32. Ross, P., Jr.; Grecula, J.; Bekaii-Saab, T.; Villalona-Calero, M.; Otterson, G.and Magro, C. Incorporation of photodynamic therapy as an induction modality in non-small cell lung cancer. *Lasers Surg Med* **2006**, 38, 881-889.
33. LoCicero, J., 3rd; Metzdorff, M.and Almgren, C. Photodynamic therapy in the palliation of late stage obstructing non-small cell lung cancer. *Chest* **1990**, 98, 97-100.

34. Maziak, D.E.; Markman, B.R.; MacKay, J.A.and Evans, W.K. Photodynamic therapy in nonsmall cell lung cancer: a systematic review. *Ann Thorac Surg* **2004**, 77, 1484-1491.
35. Sutedja, G.and Postmus, P.E. The role of photodynamic therapy in the management of stage I/II NSCLC. *Lung Cancer* **2001**, 34 Suppl 3, S35-38.
36. Dewhirst, M.W.; Prosnitz, L.; Thrall, D.; Prescott, D.; Clegg, S.; Charles, C.; MacFall, J.; Rosner, G.; Samulski, T.; Gillette, E.and LaRue, S. Hyperthermic treatment of malignant diseases: current status and a view toward the future. *Semin Oncol* **1997**, 24, 616-625.
37. Atkinson, W.J.; Brezovich, I.A.and Chakraborty, D.P. Usable frequencies in hyperthermia with thermal seeds. *IEEE Trans. Biomed, Eng. BME* **1984**, 31, 70-75.
38. Heckel, M. [Whole body warming and controlled hyperthermia using deep-penetrating short wave infrared rays]. *Med Welt* **1970**, 8, 308-313.
39. Pettigrew, R.T.and Lugate, C.M. Whole-body hyperthermia. A systemic treatment for disseminated cancer. *Recent Results Cancer Res* **1977**153-170.
40. Knorr, C.; Melling, N.; Goehl, J.; Drachsler, T.; Hohenberger, W.and Meyer, T. Long-term functional outcome after hyperthermic isolated limb perfusion (HILP). *Int J Hyperthermia* **2008**, 24, 409-414.
41. Knorr, C.; Meyer, T.; Janssen, T.; Goehl, J.and Hohenberger, W. Hyperthermic isolated limb perfusion (HILP) in malignant melanoma. Experience with 101 patients. *Eur J Surg Oncol* **2006**, 32, 224-227.
42. Loescher, L.J.and Leigh, S. Isolated regional limb hyperthermic perfusion as treatment for melanoma. *Cancer Nurs* **1984**, 7, 461-467.
43. Euler, J.; Priesching, A.; Wenzl, J.; Sauermann, G.; Klockler, K.and Kretschmer, G. [Hyperthermic peritoneal perfusion in ascites tumours in rats (author's transl)]. *Wien Klin Wochenschr* **1974**, 86, 220-225.
44. Maeta, M.; Koga, S.; Shimizu, N.; Hamazoe, R.; Kanayama, H.; Osaki, Y.and Izumi, A. [Continuous hyperthermic peritoneal perfusion for peritoneal

dissemination of gastric cancer (author's transl)]. *Nippon Gan Chiryo Gakkai Shi* **1981**, 16, 1346-1350.

45. Roseman, J.M.; Tench, D.and Bryant, L.R. The safe use of cisplatin in hyperthermic isolated limb perfusion systems. *Cancer* **1985**, 56, 742-744.
46. Cotte, E.; Glehen, O.; Mohamed, F.; Lamy, F.; Falandry, C.; Golfier, F.and Gilly, F.N. Cytoreductive surgery and intraperitoneal chemo-hyperthermia for chemo-resistant and recurrent advanced epithelial ovarian cancer: prospective study of 81 patients. *World J Surg* **2007**, 31, 1813-1820.
47. Huang, J.L. [Application of localized hyperthermia solidification combined with surgery in the treatment of liver cancer: a report of 34 cases]. *Zhonghua Wai Ke Za Zhi* **1989**, 27, 535-537, 574.
48. Dumbadze, N.D. [Prophylactic course of chemotherapy against the background of hyperthermia following radical surgery for gastric cancer]. *Klin Khir* **1973**, 6, 31-34.
49. Bull, J.M. An update on the anticancer effects of a combination of chemotherapy and hyperthermia. *Cancer Res* **1984**, 44, 4853s-4856s.
50. Dewey, W.C.; Thrall, D.E.and Gillette, E.L. Hyperthermia and radiation--a selective thermal effect on chronically hypoxic tumor cells in vivo. *Int J Radiat Oncol Biol Phys* **1977**, 2, 99-103.
51. Burd, R.; Dziedzic, T.S.; Xu, Y.; Caligiuri, M.A.; Subjeck, J.R.and Repasky, E.A. Tumor cell apoptosis, lymphocyte recruitment and tumor vascular changes are induced by low temperature, long duration (fever-like) whole body hyperthermia. *J Cell Physiol* **1998**, 177, 137-147.
52. Sakaguchi, Y.; Stephens, L.C.; Makino, M.; Kaneko, T.; Strebel, F.R.; Danhauser, L.L.; Jenkins, G.N.and Bull, J.M. Apoptosis in tumors and normal tissues induced by whole body hyperthermia in rats. *Cancer Res* **1995**, 55, 5459-5464.
53. Li, G.C.; Mivechi, N.F.and Weitzel, G. Heat shock proteins, thermotolerance, and their relevance to clinical hyperthermia. *Int J Hyperthermia* **1995**, 11, 459-488.

54. Mivechi, N.F.and Ogilvie, P.D. Effects of heat shock proteins (Mr 70,000) on protein and DNA synthesis at elevated temperatures in vitro. *Cancer Res* **1989**, 49, 1492-1496.

55. Ikeda, N.; Hayashida, O.; Kameda, H.; Ito, H.and Matsuda, T. Experimental study on thermal damage to dog normal brain. *Int J Hyperthermia* **1994**, 10, 553-561.

56. Matsuoka, F.; Shinkai, M.; Honda, H.; Kubo, T.; Sugita, T.and Kobayashi, T. Hyperthermia using magnetite cationic liposomes for hamster osteosarcoma. *Biomagn Res Technol* **2004**, 2, 3.

57. *US PATENT SUBCLASS 219 / 764*. 1999.

58. Tseng, H.Y.; Lee, G.B.; Lee, C.Y.; Shih, Y.H.and Lin, X.Z. Localised heating of tumours utilising injectable magnetic nanoparticles for hyperthermia cancer therapy. *IET Nanobiotechnol* **2009**, 3, 46-54.

59. Gilchrist, R.K.; Medal, R.; Shorey, W.D.; Hanselman, R.C.; Parrott, J.C.and Taylor, C.B. Selective inductive heating of lymph nodes. *Ann Surg* **1957**, 146, 596-606.

60. Kalambur, V.S.; Han, B.; Hammer, B.E.; Shield, T.W.and Bischof, J.C. In vitro characterization of movement, heating and visualization of magnetic nanoparticles for biomedical application. *Nanptechnology* **2005**, 16, 1221-1233.

61. Wada, S.; Tazawa, K.; Furuta, I.and Nagae, H. Antitumor effect of new local hyperthermia using dextran magnetite complex in hamster tongue carcinoma. *Oral Dis* **2003**, 9, 218-223.

62. Liu, J.; Sun, Z.; Deng, Y.; Zou, Y.; Li, C.; Guo, X.; Xiong, L.; Gao, Y.; Li, F.and Zhao, D. Highly water-dispersible biocompatible magnetite particles with low cytotoxicity stabilized by citrate groups. *Angew Chem Int Ed Engl* **2009**, 48, 5875-5879.

63. Schulze, K.; Koch, A.; Petri-Fink, A.; Steitz, B.; Kamau, S.; Hottiger, M.; Hilbe, M.; Vaughan, L.; Hofmann, M.; Hofmann, H.and von Rechenberg, B. Uptake and biocompatibility of functionalized poly(vinylalcohol) coated superparamagnetic maghemite nanoparticles by synoviocytes in vitro. *J Nanosci Nanotechnol* **2006**, 6, 2829-2840.

64. Halbreich, A.; Roger, J.; Pons, J.N.; Geldwerth, D.; Da Silva, M.F.; Roudier, M.and Bacri, J.C. Biomedical applications of maghemite ferrofluid. *Biochimie* **1998**, 80, 379-390.

65. Corot, C.; Robert, P.; Idee, J.M.and Port, M. Recent advances in iron oxide nanocrystal technology for medical imaging. *Adv Drug Deliv Rev* **2006**, 58, 1471-1504.

66. Hergt, R.; Andra, W.; d'Ambly, C.; Hilger, I.; Kaiser, W.; Richter, U.and Schmidt, H. Physical limits of hyperthermia using magnetite fine particles. *IEEE Trans.Magn.* **1988**, 34, 3745-3754.

67. Hergt, R.; Andra, W.; d'Ambly, C.G.; Hilger, I.; Kaiser, W.A.; Richter, U.and Schmidt, H.G. Physical limits of hyperthermia using magnetite fine particles. *Magnetics, IEEE Transactions on* **1998**, 34, 3745-3754.

68. Rosensweig, R.E. Heating magnetic fluid with alternating magnetic field. *Journal of Magnetism and Magnetic Materials* **2002**, 252, 370-374.

69. Brown, W.F., Jr. Thermal Fluctuations of a Single-Domain Particle. *Physical Review* **1963**, 130, 1677-1686.

70. Rosensweig, R.E. Heating magnetic fluid with alternaing magnetic field *Journal of magnetism and magnetic materials* **2002**, 252, 370-374.

71. Dolgin, E. Animal testing alternatives come alive in US. *Nat Med* **2010**, 16, 1348.

72. Mueller, M.M.and Fusenig, N.E. Friends or foes - bipolar effects of the tumour stroma in cancer. *Nat Rev Cancer* **2004**, 4, 839-849.

73. Teicher, B.A. Tumor models for efficacy determination. *Mol Cancer Ther* **2006**, 5, 2435-2443.

74. Hu, J.; Bianchi, F.; Ferguson, M.; Cesario, A.; Margaritora, S.; Granone, P.; Goldstraw, P.; Tetlow, M.; Ratcliffe, C.; Nicholson, A.G.; Harris, A.; Gatter, K.and Pezzella, F. Gene expression signature for angiogenic and nonangiogenic non-small-cell lung cancer. *Oncogene* **2005**, 24, 1212-1219.

75. McLemore, T.L.; Liu, M.C.; Blacker, P.C.; Gregg, M.; Alley, M.C.; Abbott, B.J.; Shoemaker, R.H.; Bohlman, M.E.; Litterst, C.C.; Hubbard, W.C.and et al. Novel

intrapulmonary model for orthotopic propagation of human lung cancers in athymic nude mice. *Cancer Res* **1987**, 47, 5132-5140.

76. Kang, Y.; Omura, M.; Suzuki, A.; Oka, T.; Nakagami, Y.; Cheng, C.; Nagashima, Y.and Inoue, T. Development of an orthotopic transplantation model in nude mice that simulates the clinical features of human lung cancer. *Cancer Sci* **2006**, 97, 996-1001.
77. March, T.H.; Marron-Terada, P.G.and Belinsky, S.A. Refinement of an orthotopic lung cancer model in the nude rat. *Vet Pathol* **2001**, 38, 483-490.
78. McLemore, T.L.; Eggleston, J.C.; Shoemaker, R.H.; Abbott, B.J.; Bohlman, M.E.; Liu, M.C.; Fine, D.L.; Mayo, J.G.and Boyd, M.R. Comparison of intrapulmonary, percutaneous intrathoracic, and subcutaneous models for the propagation of human pulmonary and nonpulmonary cancer cell lines in athymic nude mice. *Cancer Res* **1988**, 48, 2880-2886.
79. Nagamachi, Y.; Tani, M.; Shimizu, K.; Tsuda, H.; Niitsu, Y.and Yokota, J. Orthotopic growth and metastasis of human non-small cell lung carcinoma cell injected into the pleural cavity of nude mice. *Cancer Lett* **1998**, 127, 203-209.
80. Reddy, S.; Piccione, D.; Takita, H.and Bankert, R.B. Human lung tumor growth established in the lung and subcutaneous tissue of mice with severe combined immunodeficiency. *Cancer Res* **1987**, 47, 2456-2460.
81. Yen, W.C.; Prudente, R.Y.; Corpuz, M.R.; Negro-Vilar, A.and Lamph, W.W. A selective retinoid X receptor agonist bexarotene (LGD1069, targretin) inhibits angiogenesis and metastasis in solid tumours. *Br J Cancer* **2006**, 94, 654-660.
82. Jenkins, D.E.; Oei, Y.; Hornig, Y.S.; Yu, S.F.; Dusich, J.; Purchio, T.and Contag, P.R. Bioluminescent imaging (BLI) to improve and refine traditional murine models of tumor growth and metastasis. *Clin Exp Metastasis* **2003**, 20, 733-744.
83. Wang, X.; Fu, X.and Hoffman, R.M. A patient-like metastasizing model of human lung adenocarcinoma constructed via thoracotomy in nude mice. *Anticancer Res* **1992**, 12, 1399-1401.

84. Wang, X.; Fu, X.; Kubota, T.and Hoffman, R.M. A new patient-like metastatic model of human small-cell lung cancer constructed orthotopically with intact tissue via thoracotomy in nude mice. *Anticancer Res* **1992**, 12, 1403-1406.

85. Wang, X.; Fu, X.and Hoffman, R.M. A new patient-like metastatic model of human lung cancer constructed orthotopically with intact tissue via thoracotomy in immunodeficient mice. *Int J Cancer* **1992**, 51, 992-995.

86. Kraus-Berthier, L.; Jan, M.; Guilbaud, N.; Naze, M.; Pierre, A.and Atassi, G. Histology and sensitivity to anticancer drugs of two human non-small cell lung carcinomas implanted in the pleural cavity of nude mice. *Clin Cancer Res* **2000**, 6, 297-304.

87. Shimkin, M.B.and Stoner, G.D. Lung tumors in mice: application to carcinogenesis bioassay. *Adv Cancer Res* **1975**, 21, 1-58.

88. Malkinson, A.M. Primary lung tumors in mice as an aid for understanding, preventing, and treating human adenocarcinoma of the lung. *Lung Cancer* **2001**, 32, 265-279.

89. Lynch, C.J. Studies on the Relation between Tumor Susceptibility and Heredity : Iii. Spontaneous Tumors of the Lung in Mice. *J Exp Med* **1926**, 43, 339-355.

90. Andervont, H.B.and Shimkin, M.B. Biologic Testing of Carcinogens. II. Pulmonary-Tumor-Induction Technique. *Journal of the National Cancer Institute* **1940**, 1, 225-239.

91. Shimkin, M.B.and Leiter, J. Induced Pulmonary Tumors in Mice. III. The Role of Chronic Irritation in the Production of Pulmonary Tumors in Strain a Mice. *Journal of the National Cancer Institute* **1940**, 1, 241-254.

92. Wattenberg, L.W.and Leong, J.L. Inhibition of the carcinogenic action of benzo(a)pyrene by flavones. *Cancer Research* **1970**, 30, 1922-1925.

93. Stoner, G.D.; Adam-Rodwell, G.and Morse, M.A. Lung tumors in strain A mice: application for studies in cancer chemoprevention. *J Cell Biochem Suppl* **1993**, 17F, 95-103.

94. Stoner, G.D. Lung tumors in strain A mice as a bioassay for carcinogenicity of environmental chemicals. *Experimental lung research* **1991**, 17, 405-423.

95. Hecht, S.S.; Morse, M.A.; Amin, S.; Stoner, G.D.; Jordan, K.G.; Choi, C.I.and Chung, F.L. Rapid single-dose model for lung tumor induction in A/J mice by 4-(methylnitrosamino)-1-(3-pyridyl)-1-butanone and the effect of diet. *Carcinogenesis* **1989**, 10, 1901-1904.

96. Kim, S.H.and Lee, C.S. Induction of benign and malignant pulmonary tumours in mice with benzo(a)pyrene. *Anticancer research* **1996**, 16, 465-470.

97. Meuwissen, R.; Linn, S.C.; van der Valk, M.; Mooi, W.J.and Berns, A. Mouse model for lung tumorigenesis through Cre/lox controlled sporadic activation of the K-Ras oncogene. *Oncogene* **2001**, 20, 6551-6558.

98. Li, D.; Ji, H.; Zaghlul, S.; McNamara, K.; Liang, M.C.; Shimamura, T.; Kubo, S.; Takahashi, M.; Chirieac, L.R.; Padera, R.F.; Scott, A.M.; Jungbluth, A.A.; Cavenee, W.K.; Old, L.J.; Demetri, G.D.and Wong, K.K. Therapeutic anti-EGFR antibody 806 generates responses in murine de novo EGFR mutant-dependent lung carcinomas. *J Clin Invest* **2007**, 117, 346-352.

99. Pritchard, C.; Carragher, L.; Aldridge, V.; Giblett, S.; Jin, H.; Foster, C.; Andreadi, C.and Kamata, T. Mouse models for BRAF-induced cancers. *Biochem Soc Trans* **2007**, 35, 1329-1333.

100. Engelman, J.A.; Chen, L.; Tan, X.; Crosby, K.; Guimaraes, A.R.; Upadhyay, R.; Maira, M.; McNamara, K.; Perera, S.A.; Song, Y.; Chirieac, L.R.; Kaur, R.; Lightbown, A.; Simendinger, J.; Li, T.; Padera, R.F.; Garcia-Echeverria, C.; Weissleder, R.; Mahmood, U.; Cantley, L.C.and Wong, K.K. Effective use of PI3K and MEK inhibitors to treat mutant Kras G12D and PIK3CA H1047R murine lung cancers. *Nat Med* **2008**, 14, 1351-1356.

101. Chen, Z.; Sasaki, T.; Tan, X.; Carretero, J.; Shimamura, T.; Li, D.; Xu, C.; Wang, Y.; Adelmant, G.O.; Capelletti, M.; Lee, H.J.; Rodig, S.J.; Borgman, C.; Park, S.I.; Kim, H.R.; Padera, R.; Marto, J.A.; Gray, N.S.; Kung, A.L.; Shapiro, G.I.; Janne, P.A.and Wong, K.K. Inhibition of ALK, PI3K/MEK, and HSP90 in murine lung adenocarcinoma induced by EML4-ALK fusion oncogene. *Cancer Res* **2010**, 70, 9827-9836.

102. Singh, M.; Lima, A.; Molina, R.; Hamilton, P.; Clermont, A.C.; Devasthali, V.; Thompson, J.D.; Cheng, J.H.; Bou Reslan, H.; Ho, C.C.; Cao, T.C.; Lee, C.V.; Nannini, M.A.; Fuh, G.; Carano, R.A.; Koeppen, H.; Yu, R.X.; Forrest, W.F.; Plowman, G.D.and Johnson, L. Assessing therapeutic responses in Kras mutant cancers using genetically engineered mouse models. *Nat Biotechnol* **2010**, 28, 585-593.

103. de Seranno, S.and Meuwissen, R. Progress and applications of mouse models for human lung cancer. *European Respiratory Journal* **2010**, 35, 426-443.

104. Politi, K.; Zakowski, M.F.; Fan, P.D.; Schonfeld, E.A.; Pao, W.and Varmus, H.E. Lung adenocarcinomas induced in mice by mutant EGF receptors found in human lung cancers respond to a tyrosine kinase inhibitor or to down-regulation of the receptors. *Genes Dev* **2006**, 20, 1496-1510.

105. Hadjantonakis, A.K.; Dickinson, M.E.; Fraser, S.E.and Papaioannou, V.E. Technicolour transgenics: Imaging tools for functional genomics in the mouse. *Nat Rev Genet* **2003**, 4, 613-625.

106. Contag, C.H.; Jenkins, D.; Contag, F.R.and Negrin, R.S. Use of reporter genes for optical measurements of neoplastic disease in vivo. *Neoplasia* **2000**, 2, 41-52.

107. Giard, D.J.; Aaronson, S.A.; Todaro, G.J.; Arnstein, P.; Kersey, J.H.; Dosik, H.and Parks, W.P. In vitro cultivation of human tumors: establishment of cell lines derived from a series of solid tumors. *J Natl Cancer Inst* **1973**, 51, 1417-1423.

108. Yang, W.; Peters, J.I.and Williams, R.O., 3rd. Inhaled nanoparticles--a current review. *Int J Pharm* **2008**, 356, 239-247.

109. Patton, J.S.and Byron, P.R. Inhaling medicines: delivering drugs to the body through the lungs. *Nat Rev Drug Discov* **2007**, 6, 67-74.

110. Mansour, H.M.; Rhee, Y.S.and Wu, X. Nanomedicine in pulmonary delivery. *Int J Nanomedicine* **2009**, 4, 299-319.

111. Labiris, N.R.and Dolovich, M.B. Pulmonary drug delivery. Part I: physiological factors affecting therapeutic effectiveness of aerosolized medications. *Br J Clin Pharmacol* **2003**, 56, 588-599.

112. Hiller, F.C., *Therapeutic Aerosols*, in *Pharmaceutical Inhalation Aerosol Technology, Second Edition*. 2003, Informa Healthcare.
113. Rees, P.J.; Clark, T.J.and Moren, F. The importance of particle size in response to inhaled bronchodilators. *Eur J Respir Dis Suppl* **1982**, 119, 73-78.
114. Zanen, P.; Go, L.T.and Lammers, J.W. Optimal particle size for beta 2 agonist and anticholinergic aerosols in patients with severe airflow obstruction. *Thorax* **1996**, 51, 977-980.
115. Dolovich, M. Physical principles underlying aerosol therapy. *Journal of Aerosol Medicine* **1989**, 2, 171 - 186.
116. Ruffin, R.E.; Dolovich, M.B.; Wolff, R.K.and Newhouse, M.T. The effects of preferential deposition of histamine in the human airway. *Am Rev Respir Dis* **1978**, 117, 485-492.
117. Lourenco, R.V.and Cotromanes, E. Clinical aerosols. I. Characterization of aerosols and their diagnostic uses. *Arch Intern Med* **1982**, 142, 2163-2172.
118. Heyder, J. Particle transport onto human airway surfaces. *Eur J Respir Dis Suppl* **1982**, 119, 29-50.
119. Newman, S.P.; Agnew, J.E.; Pavia, D.and Clarke, S.W. Inhaled aerosols: lung deposition and clinical applications. *Clin Phys Physiol Meas* **1982**, 3, 1-20.
120. Hogg, J.C. Response of the lung to inhaled particles. *Med J Aust* **1985**, 142, 675-678.
121. Byron, P.R. Prediction of drug residence times in regions of the human respiratory tract following aerosol inhalation. *J Pharm Sci* **1986**, 75, 433-438.
122. Yi, D.; Naqwi, A.; Panoskaltsis-Mortari, A.and Wiedmann, T.S. Distribution of aerosols in mouse lobes by fluorescent imaging. *International Journal of Pharmaceutics* **2012**, 426, 108-115.
123. Raabe, O.G.; Al-Bayati, M.A.; Teague, S.V.and Rasolt, A. Regional Deposition of Inhaled Monodisperse Coarse and Fine Aerosol Particles in Small Laboratory Animals. *Annals of Occupational Hygiene* **1988**, 32, 53-63.

124. Xie, Y.; Longest, P.W.; Xu, Y.H.; Wang, J.P.and Wiedmann, T.S. In vitro and in vivo lung deposition of coated magnetic aerosol particles. *Journal of Pharmaceutical Sciences* **2010**, 99, 4658-4668.

125. Beck, S.E.; Laube, B.L.; Barberena, C.I.; Fischer, A.C.; Adams, R.J.; Chesnut, K.; Flotte, T.R.and Guggino, W.B. Deposition and expression of aerosolized rAAV vectors in the lungs of Rhesus macaques. *Mol Ther* **2002**, 6, 546-554.

126. Steinhauser, I.; Spankuch, B.; Strebhardt, K.and Langer, K. Trastuzumab-modified nanoparticles: optimisation of preparation and uptake in cancer cells. *Biomaterials* **2006**, 27, 4975-4983.

127. Tada, H.; Higuchi, H.; Wanatabe, T.M.and Ohuchi, N. In vivo real-time tracking of single quantum dots conjugated with monoclonal anti-HER2 antibody in tumors of mice. *Cancer Res* **2007**, 67, 1138-1144.

128. Hallahan, D.; Geng, L.; Qu, S.; Scarfone, C.; Giorgio, T.; Donnelly, E.; Gao, X.and Clanton, J. Integrin-mediated targeting of drug delivery to irradiated tumor blood vessels. *Cancer Cell* **2003**, 3, 63-74.

129. Tsutsui, Y.; Tomizawa, K.; Nagita, M.; Michiue, H.; Nishiki, T.; Ohmori, I.; Seno, M.and Matsui, H. Development of bionanocapsules targeting brain tumors. *J Control Release* **2007**, 122, 159-164.

130. Smith, J.E.; Medley, C.D.; Tang, Z.; Shangguan, D.; Lofton, C.and Tan, W. Aptamer-conjugated nanoparticles for the collection and detection of multiple cancer cells. *Anal Chem* **2007**, 79, 3075-3082.

131. Raz, A.; Meromsky, L.and Lotan, R. Differential expression of endogenous lectins on the surface of nontumorigenic, tumorigenic, and metastatic cells. *Cancer Res* **1986**, 46, 3667-3672.

132. Yamazaki, N.; Kojima, S.; Bovin, N.V.; Andre, S.; Gabius, S.and Gabius, H.J. Endogenous lectins as targets for drug delivery. *Adv Drug Deliv Rev* **2000**, 43, 225-244.

133. Fujita, M.; Lee, B.S.; Khazenzon, N.M.; Penichet, M.L.; Wawrowsky, K.A.; Patil, R.; Ding, H.; Holler, E.; Black, K.L.and Ljubimova, J.Y. Brain tumor tandem

targeting using a combination of monoclonal antibodies attached to biopoly(beta-L-malic acid). *J Control Release* **2007**, 122, 356-363.

134. Liu, Y.; Steiniger, S.C.; Kim, Y.; Kaufmann, G.F.; Felding-Habermann, B.and Janda, K.D. Mechanistic studies of a peptidic GRP78 ligand for cancer cell-specific drug delivery. *Mol Pharm* **2007**, 4, 435-447.

135. Pun, S.H.; Tack, F.; Bellocq, N.C.; Cheng, J.; Grubbs, B.H.; Jensen, G.S.; Davis, M.E.; Brewster, M.; Janicot, M.; Janssens, B.; Floren, W.and Bakker, A. Targeted delivery of RNA-cleaving DNA enzyme (DNAzyme) to tumor tissue by transferrin-modified, cyclodextrin-based particles. *Cancer Biol Ther* **2004**, 3, 641-650.

136. Iwakiri, S.; Sonobe, M.; Nagai, S.; Hirata, T.; Wada, H.and Miyahara, R. Expression status of folate receptor alpha is significantly correlated with prognosis in non-small-cell lung cancers. *Ann Surg Oncol* **2008**, 15, 889-899.

137. Lennon, F.E.; Mirzapoiazova, T.; Mambetsariev, B.; Salgia, R.; Moss, J.and Singleton, P.A. Overexpression of the mu-opioid receptor in human non-small cell lung cancer promotes Akt and mTOR activation, tumor growth, and metastasis. *Anesthesiology* **2012**, 116, 857-867.

138. Li, S.; Huang, S.and Peng, S.B. Overexpression of G protein-coupled receptors in cancer cells: involvement in tumor progression. *Int J Oncol* **2005**, 27, 1329-1339.

139. Yin, M.; Guan, X.; Liao, Z.and Wei, Q. Insulin-like growth factor-1 receptor-targeted therapy for non-small cell lung cancer: a mini review. *Am J Transl Res* **2009**, 1, 101-114.

140. Merrick, D.T.; Kittelson, J.; Winterhalder, R.; Kotantoulas, G.; Ingeberg, S.; Keith, R.L.; Kennedy, T.C.; Miller, Y.E.; Franklin, W.A.and Hirsch, F.R. Analysis of c-ErbB1/epidermal growth factor receptor and c-ErbB2/HER-2 expression in bronchial dysplasia: evaluation of potential targets for chemoprevention of lung cancer. *Clin Cancer Res* **2006**, 12, 2281-2288.

141. Tang, X.; Varella-Garcia, M.; Xavier, A.C.; Massarelli, E.; Ozburn, N.; Moran, C.and Wistuba, II. Epidermal growth factor receptor abnormalities in the

pathogenesis and progression of lung adenocarcinomas. *Cancer Prev Res (Phila Pa)* **2008**, 1, 192-200.

142. Varella-Garcia, M.; Mitsudomi, T.; Yatabe, Y.; Kosaka, T.; Nakajima, E.; Xavier, A.C.; Skokan, M.; Zeng, C.; Franklin, W.A.; Bunn, P.A., Jr.and Hirsch, F.R. EGFR and HER2 genomic gain in recurrent non-small cell lung cancer after surgery: impact on outcome to treatment with gefitinib and association with EGFR and KRAS mutations in a Japanese cohort. *J Thorac Oncol* **2009**, 4, 318-325.
143. Li, Z.; Zhao, R.; Wu, X.; Sun, Y.; Yao, M.; Li, J.; Xu, Y.and Gu, J. Identification and characterization of a novel peptide ligand of epidermal growth factor receptor for targeted delivery of therapeutics. *FASEB J* **2005**, 19, 1978-1985.
144. Matsumura, Y.and Maeda, H. A new concept for macromolecular therapeutics in cancer chemotherapy: mechanism of tumoritropic accumulation of proteins and the antitumor agent smancs. *Cancer Res* **1986**, 46, 6387-6392.
145. Desai, N.; Trieu, V.; Yao, Z.; Louie, L.; Ci, S.; Yang, A.; Tao, C.; De, T.; Beals, B.; Dykes, D.; Noker, P.; Yao, R.; Labao, E.; Hawkins, M.and Soon-Shiong, P. Increased antitumor activity, intratumor paclitaxel concentrations, and endothelial cell transport of cremophor-free, albumin-bound paclitaxel, ABI-007, compared with cremophor-based paclitaxel. *Clin Cancer Res* **2006**, 12, 1317-1324.
146. Singh, S.; Sharma, A.and Robertson, G.P. Realizing the clinical potential of cancer nanotechnology by minimizing toxicologic and targeted delivery concerns. *Cancer Res* **2012**, 72, 5663-5668.
147. Perrault, S.D.; Walkey, C.; Jennings, T.; Fischer, H.C.and Chan, W.C. Mediating tumor targeting efficiency of nanoparticles through design. *Nano Lett* **2009**, 9, 1909-1915.
148. Kong, G.; Braun, R.D.and Dewhirst, M.W. Hyperthermia enables tumor-specific nanoparticle delivery: effect of particle size. *Cancer Res* **2000**, 60, 4440-4445.
149. Qian, X.; Peng, X.H.; Ansari, D.O.; Yin-Goen, Q.; Chen, G.Z.; Shin, D.M.; Yang, L.; Young, A.N.; Wang, M.D.and Nie, S. In vivo tumor targeting and

spectroscopic detection with surface-enhanced Raman nanoparticle tags. *Nat Biotechnol* **2008**, 26, 83-90.

150. Lee, H.; Lee, E.; Kim do, K.; Jang, N.K.; Jeong, Y.Y.and Jon, S. Antibiofouling polymer-coated superparamagnetic iron oxide nanoparticles as potential magnetic resonance contrast agents for in vivo cancer imaging. *J Am Chem Soc* **2006**, 128, 7383-7389.
151. Peng, X.H.; Qian, X.; Mao, H.; Wang, A.Y.; Chen, Z.G.; Nie, S.and Shin, D.M. Targeted magnetic iron oxide nanoparticles for tumor imaging and therapy. *Int J Nanomedicine* **2008**, 3, 311-321.
152. Diaz, B.; Sanchez-Espinel, C.; Arruebo, M.; Faro, J.; de Miguel, E.; Magadan, S.; Yague, C.; Fernandez-Pacheco, R.; Ibarra, M.R.; Santamaria, J.and Gonzalez-Fernandez, A. Assessing methods for blood cell cytotoxic responses to inorganic nanoparticles and nanoparticle aggregates. *Small* **2008**, 4, 2025-2034.
153. van Landeghem, F.K.; Maier-Hauff, K.; Jordan, A.; Hoffmann, K.T.; Gneveckow, U.; Scholz, R.; Thiesen, B.; Bruck, W.and von Deimling, A. Post-mortem studies in glioblastoma patients treated with thermotherapy using magnetic nanoparticles. *Biomaterials* **2009**, 30, 52-57.
154. Safi, M.; Sarrouj, H.; Sandre, O.; Mignet, N.and Berret, J.F. Interactions between sub-10-nm iron and cerium oxide nanoparticles and 3T3 fibroblasts: the role of the coating and aggregation state. *Nanotechnology* **2010**, 21, 145103.
155. Lundqvist, M.; Stigler, J.; Elia, G.; Lynch, I.; Cedervall, T.and Dawson, K.A. Nanoparticle size and surface properties determine the protein corona with possible implications for biological impacts. *Proc Natl Acad Sci U S A* **2008**, 105, 14265-14270.
156. Hiergeist, R.; Andrä, W.; Buske, N.; Hergt, R.; Hilger, I.; Richter, U.and Kaiser, W. Application of magnetite ferrofluids for hyperthermia. *Journal of Magnetism and Magnetic Materials* **1999**, 201, 420-422.
157. Jordan, A.; Scholz, R.; Wust, P.; Fähling, H.and Roland, F. Magnetic fluid hyperthermia (MFH): Cancer treatment with AC magnetic field induced

excitation of biocompatible superparamagnetic nanoparticles. *Journal of Magnetism and Magnetic Materials* **1999**, 201, 413-419.

158. Tasci, T.O.; Vargel, I.; Arat, A.; Guzel, E.; Korkusuz, P.and Atalar, E. Focused RF hyperthermia using magnetic fluids. *Med Phys* **2009**, 36, 1906-1912.
159. Foy, S.P.; Manthe, R.L.; Foy, S.T.; Dimitrijevic, S.; Krishnamurthy, N.and Labhasetwar, V. Optical imaging and magnetic field targeting of magnetic nanoparticles in tumors. *ACS Nano* **2010**, 4, 5217-5224.
160. Krishna Murti, G.S.R.; Moharir, A.V.and Sarma, V.A.K. Spectrophotometric determination of iron with orthophenanthroline. *Microchemical Journal* **1970**, 15, 585-589.
161. Sugimoto, T.and Matijević, E. Formation of uniform spherical magnetite particles by crystallization from ferrous hydroxide gels. *Journal of Colloid and Interface Science* **1980**, 74, 227-243.
162. Liu, D.; Wang, L.; Wang, Z.and Cuschieri, A. Magnetoporation and Magnetolysis of Cancer Cells via Carbon Nanotubes Induced by Rotating Magnetic Fields. *Nano Lett* **2012**, 12, 5117-5121.
163. Giustini, A.J.; Ivkov, R.and Hoopes, P.J. Magnetic nanoparticle biodistribution following intratumoral administration. *Nanotechnology* **2011**, 22, 345101.
164. Luchetti, F.; Canonico, B.; Della Felice, M.; Burattini, S.; Battistelli, M.; Papa, S.and Falcieri, E. Hyperthermia triggers apoptosis and affects cell adhesiveness in human neuroblastoma cells. *Histol Histopathol* **2003**, 18, 1041-1052.
165. Rodriguez-Luccioni, H.L.; Latorre-Esteves, M.; Mendez-Vega, J.; Soto, O.; Rodriguez, A.R.; Rinaldi, C.and Torres-Lugo, M. Enhanced reduction in cell viability by hyperthermia induced by magnetic nanoparticles. *Int J Nanomedicine* **2011**, 6, 373-380.
166. Takasu, T.; Lyons, J.C.; Park, H.J.and Song, C.W. Apoptosis and perturbation of cell cycle progression in an acidic environment after hyperthermia. *Cancer Res* **1998**, 58, 2504-2508.
167. Nicholson, D.W.; Ali, A.; Thornberry, N.A.; Vaillancourt, J.P.; Ding, C.K.; Gallant, M.; Gareau, Y.; Griffin, P.R.; Labelle, M.; Lazebnik, Y.A.and et al.

Identification and inhibition of the ICE/CED-3 protease necessary for mammalian apoptosis. *Nature* **1995**, 376, 37-43.

168. Lazebnik, Y.A.; Kaufmann, S.H.; Desnoyers, S.; Poirier, G.G.and Earnshaw, W.C. Cleavage of poly(ADP-ribose) polymerase by a proteinase with properties like ICE. *Nature* **1994**, 371, 346-347.
169. Uchiyama, Y. Autophagic cell death and its execution by lysosomal cathepsins. *Arch Histol Cytol* **2001**, 64, 233-246.
170. Chaitanya, G.V.; Steven, A.J.and Babu, P.P. PARP-1 cleavage fragments: signatures of cell-death proteases in neurodegeneration. *Cell Commun Signal* **2010**, 8, 31.
171. Kabeya, Y.; Mizushima, N.; Ueno, T.; Yamamoto, A.; Kirisako, T.; Noda, T.; Kominami, E.; Ohsumi, Y.and Yoshimori, T. LC3, a mammalian homologue of yeast Apg8p, is localized in autophagosome membranes after processing. *EMBO J* **2000**, 19, 5720-5728.
172. Tsujimoto, Y.and Shimizu, S. Another way to die: autophagic programmed cell death. *Cell Death Differ* **2005**, 12 Suppl 2, 1528-1534.
173. Zhang, H.; Kong, X.; Kang, J.; Su, J.; Li, Y.; Zhong, J.and Sun, L. Oxidative stress induces parallel autophagy and mitochondria dysfunction in human glioma U251 cells. *Toxicol Sci* **2009**, 110, 376-388.
174. Chen, Y.; McMillan-Ward, E.; Kong, J.; Israels, S.J.and Gibson, S.B. Oxidative stress induces autophagic cell death independent of apoptosis in transformed and cancer cells. *Cell Death Differ* **2008**, 15, 171-182.
175. Scherz-Shouval, R.; Shvets, E.; Fass, E.; Shorer, H.; Gil, L.and Elazar, Z. Reactive oxygen species are essential for autophagy and specifically regulate the activity of Atg4. *EMBO J* **2007**, 26, 1749-1760.
176. Cerella, C.; D'Alessio, M.; Cristofanon, S.; De Nicola, M.; Radogna, F.; Dicato, M.; Diederich, M.and Ghibelli, L. Subapoptogenic oxidative stress strongly increases the activity of the glycolytic key enzyme glyceraldehyde 3-phosphate dehydrogenase. *Ann N Y Acad Sci* **2009**, 1171, 583-590.

177. Colell, A.; Ricci, J.E.; Tait, S.; Milasta, S.; Maurer, U.; Bouchier-Hayes, L.; Fitzgerald, P.; Guio-Carrion, A.; Waterhouse, N.J.; Li, C.W.; Mari, B.; Barbry, P.; Newmeyer, D.D.; Beere, H.M.and Green, D.R. GAPDH and autophagy preserve survival after apoptotic cytochrome c release in the absence of caspase activation. *Cell* **2007**, 129, 983-997.

178. Proskuryakov, S.Y.; Konoplyannikov, A.G.and Gabai, V.L. Necrosis: a specific form of programmed cell death? *Exp Cell Res* **2003**, 283, 1-16.

179. Frossard, J.L. Heat shock protein 70 (HSP70) prolongs survival in rats exposed to hyperthermia. *Eur J Clin Invest* **1999**, 29, 561-562.

180. Ito, A.; Shinkai, M.; Honda, H.; Yoshikawa, K.; Saga, S.; Wakabayashi, T.; Yoshida, J.and Kobayashi, T. Heat shock protein 70 expression induces antitumor immunity during intracellular hyperthermia using magnetite nanoparticles. *Cancer Immunol Immunother* **2003**, 52, 80-88.

181. Patil, Y.; Sadhukha, T.; Ma, L.and Panyam, J. Nanoparticle-mediated simultaneous and targeted delivery of paclitaxel and tariquidar overcomes tumor drug resistance. *J Control Release* **2009**, 136, 21-29.

182. Barros, L.F.; Kanaseki, T.; Sabirov, R.; Morishima, S.; Castro, J.; Bittner, C.X.; Maeno, E.; Ando-Akatsuka, Y.and Okada, Y. Apoptotic and necrotic blebs in epithelial cells display similar neck diameters but different kinase dependency. *Cell Death Differ* **2003**, 10, 687-697.

183. Huang, H.; Delikanli, S.; Zeng, H.; Ferkey, D.M.and Pralle, A. Remote control of ion channels and neurons through magnetic-field heating of nanoparticles. *Nat Nanotechnol* **2010**, 5, 602-606.

184. Polo-Corrales, L.and Rinaldi, C. Monitoring iron oxide nanoparticle surface temperature in an alternating magnetic field using thermoresponsive fluorescent polymers. *Journal of Applied Physics* **2012**, 111, 07B334-333.

185. Vaughan, T.E.and Weaver, J.C. Energetic constraints on the creation of cell membrane pores by magnetic particles. *Biophys J* **1996**, 71, 616-622.

186. Carrstensen, H.; Muller, R.H.and Muller, B.W. Particle size, surface hydrophobicity and interaction with serum of parenteral fat emulsions and model drug carriers as parameters related to RES uptake. *Clin Nutr* **1992**, 11, 289-297.

187. Zarogoulidis, P.; Chatzaki, E.; Porpodis, K.; Domvri, K.; Hohenforst-Schmidt, W.; Goldberg, E.P.; Karamanos, N.and Zarogoulidis, K. Inhaled chemotherapy in lung cancer: future concept of nanomedicine. *Int J Nanomedicine* **2012**, 7, 1551-1572.

188. Yi, D.and Wiedmann, T.S. Inhalation adjuvant therapy for lung cancer. *J Aerosol Med Pulm Drug Deliv* **2010**, 23, 181-187.

189. Chandler, J.M.and Lagasse, E. Cancerous stem cells: deviant stem cells with cancer-causing misbehavior. *Stem Cell Res Ther* **2010**, 1, 13.

190. Potten, C.S.and Loeffler, M. Stem cells: attributes, cycles, spirals, pitfalls and uncertainties. Lessons for and from the crypt. *Development* **1990**, 110, 1001-1020.

191. Li, X.; Lewis, M.T.; Huang, J.; Gutierrez, C.; Osborne, C.K.; Wu, M.F.; Hilsenbeck, S.G.; Pavlick, A.; Zhang, X.; Chamness, G.C.; Wong, H.; Rosen, J.and Chang, J.C. Intrinsic resistance of tumorigenic breast cancer cells to chemotherapy. *J Natl Cancer Inst* **2008**, 100, 672-679.

192. Moitra, K.; Lou, H.and Dean, M. Multidrug efflux pumps and cancer stem cells: insights into multidrug resistance and therapeutic development. *Clin Pharmacol Ther* **2011**, 89, 491-502.

193. Bao, S.; Wu, Q.; McLendon, R.E.; Hao, Y.; Shi, Q.; Hjelmeland, A.B.; Dewhirst, M.W.; Bigner, D.D.and Rich, J.N. Glioma stem cells promote radioresistance by preferential activation of the DNA damage response. *Nature* **2006**, 444, 756-760.

194. Diehn, M.; Cho, R.W.; Lobo, N.A.; Kalisky, T.; Dorie, M.J.; Kulp, A.N.; Qian, D.; Lam, J.S.; Ailles, L.E.; Wong, M.; Joshua, B.; Kaplan, M.J.; Wapnir, I.; Dirbas, F.M.; Somlo, G.; Garberoglio, C.; Paz, B.; Shen, J.; Lau, S.K.; Quake, S.R.; Brown, J.M.; Weissman, I.L.and Clarke, M.F. Association of reactive oxygen species levels and radioresistance in cancer stem cells. *Nature* **2009**, 458, 780-783.

195. Moore, N.and Lyle, S. Quiescent, slow-cycling stem cell populations in cancer: a review of the evidence and discussion of significance. *J Oncol* **2011**, 2011.

196. Dylla, S.J.; Beviglia, L.; Park, I.K.; Chartier, C.; Raval, J.; Ngan, L.; Pickell, K.; Aguilar, J.; Lazetic, S.; Smith-Berdan, S.; Clarke, M.F.; Hoey, T.; Lewicki, J.and Gurney, A.L. Colorectal cancer stem cells are enriched in xenogeneic tumors following chemotherapy. *PLoS One* **2008**, 3, e2428.

197. van der Zee, J.; Gonzalez Gonzalez, D.; van Rhoon, G.C.; van Dijk, J.D.; van Putten, W.L.and Hart, A.A. Comparison of radiotherapy alone with radiotherapy plus hyperthermia in locally advanced pelvic tumours: a prospective, randomised, multicentre trial. Dutch Deep Hyperthermia Group. *Lancet* **2000**, 355, 1119-1125.

198. Atkinson, R.L.; Zhang, M.; Diagaradjane, P.; Peddibhotla, S.; Contreras, A.; Hilsenbeck, S.G.; Woodward, W.A.; Krishnan, S.; Chang, J.C.and Rosen, J.M. Thermal enhancement with optically activated gold nanoshells sensitizes breast cancer stem cells to radiation therapy. *Sci Transl Med* **2010**, 2, 55ra79.

199. Maier-Hauff, K.; Ulrich, F.; Nestler, D.; Niehoff, H.; Wust, P.; Thiesen, B.; Orawa, H.; Budach, V.and Jordan, A. Efficacy and safety of intratumoral thermotherapy using magnetic iron-oxide nanoparticles combined with external beam radiotherapy on patients with recurrent glioblastoma multiforme. *J Neurooncol* **2011**, 103, 317-324.

200. Johannsen, M.; Thiesen, B.; Jordan, A.; Taymoorian, K.; Gneveckow, U.; Waldofner, N.; Scholz, R.; Koch, M.; Lein, M.; Jung, K.and Loening, S.A. Magnetic fluid hyperthermia (MFH)reduces prostate cancer growth in the orthotopic Dunning R3327 rat model. *Prostate* **2005**, 64, 283-292.

201. Jones, S.K.; Winter, J.G.and Gray, B.N. Treatment of experimental rabbit liver tumours by selectively targeted hyperthermia. *Int J Hyperthermia* **2002**, 18, 117-128.

202. Jordan, A.; Scholz, R.; Maier-Hauff, K.; van Landeghem, F.K.; Waldoefner, N.; Teichgraeber, U.; Pinkernelle, J.; Bruhn, H.; Neumann, F.; Thiesen, B.; von Deimling, A.and Felix, R. The effect of thermotherapy using magnetic nanoparticles on rat malignant glioma. *J Neurooncol* **2006**, 78, 7-14.

203. Balivada, S.; Rachakatla, R.S.; Wang, H.; Samarakoon, T.N.; Dani, R.K.; Pyle, M.; Kroh, F.O.; Walker, B.; Leaym, X.; Koper, O.B.; Tamura, M.; Chikan, V.; Bossmann, S.H.and Troyer, D.L. A/C magnetic hyperthermia of melanoma mediated by iron(0)/iron oxide core/shell magnetic nanoparticles: a mouse study. *BMC Cancer* **2010**, 10, 119.

204. Jain, T.K.; Morales, M.A.; Sahoo, S.K.; Leslie-Pelecky, D.L.and Labhasetwar, V. Iron oxide nanoparticles for sustained delivery of anticancer agents. *Mol Pharm* **2005**, 2, 194-205.

205. Tae-Youb, K.and Yamazaki, Y. Determination of the magnetic compensation composition in Al-substituted Bi-DyCoIG nanoparticles with enhanced coercive-force. *Magnetics, IEEE Transactions on* **2004**, 40, 2793-2795.

206. Ho, M.M.; Ng, A.V.; Lam, S.and Hung, J.Y. Side population in human lung cancer cell lines and tumors is enriched with stem-like cancer cells. *Cancer Res* **2007**, 67, 4827-4833.

207. Grimshaw, M.; Cooper, L.; Papazisis, K.; Coleman, J.; Bohnenkamp, H.; Chiapero-Stanke, L.; Taylor-Papadimitriou, J.and Burchell, J. Mammosphere culture of metastatic breast cancer cells enriches for tumorigenic breast cancer cells. *Breast Cancer Research* **2008**, 10, R52.

208. Ginestier, C.; Hur, M.H.; Charafe-Jauffret, E.; Monville, F.; Dutcher, J.; Brown, M.; Jacquemier, J.; Viens, P.; Kleer, C.G.; Liu, S.; Schott, A.; Hayes, D.; Birnbaum, D.; Wicha, M.S.and Dontu, G. ALDH1 is a marker of normal and malignant human mammary stem cells and a predictor of poor clinical outcome. *Cell stem cell* **2007**, 1, 555-567.

209. Franken, N.A.P.; Rodermond, H.M.; Stap, J.; Haveman, J.and van Bree, C. Clonogenic assay of cells in vitro. *Nat. Protocols* **2006**, 1, 2315-2319.

210. He, L.; Yang, C.P.and Horwitz, S.B. Mutations in beta-tubulin map to domains involved in regulation of microtubule stability in epothilone-resistant cell lines. *Mol Cancer Ther* **2001**, 1, 3-10.

211. Croker, A.K.; Goodale, D.; Chu, J.; Postenka, C.; Hedley, B.D.; Hess, D.A.and Allan, A.L. High aldehyde dehydrogenase and expression of cancer stem cell

markers selects for breast cancer cells with enhanced malignant and metastatic ability. *J Cell Mol Med* **2009**, 13, 2236-2252.

212. Iliopoulos, D.; Hirsch, H.A.; Wang, G.and Struhl, K. Inducible formation of breast cancer stem cells and their dynamic equilibrium with non-stem cancer cells via IL6 secretion. *Proc Natl Acad Sci U S A* **2011**, 108, 1397-1402.
213. Burke, A.R.; Singh, R.N.; Carroll, D.L.; Wood, J.C.S.; D'Agostino Jr, R.B.; Ajayan, P.M.; Torti, F.M.and Torti, S.V. The resistance of breast cancer stem cells to conventional hyperthermia and their sensitivity to nanoparticle-mediated photothermal therapy. *Biomaterials* **2012**, 33, 2961-2970.
214. Korzeniewski, C.and Callewaert, D.M. An enzyme-release assay for natural cytotoxicity. *J Immunol Methods* **1983**, 64, 313-320.
215. Spagnuolo, G.; D'Anto, V.; Cosentino, C.; Schmalz, G.; Schweikl, H.and Rengo, S. Effect of N-acetyl-L-cysteine on ROS production and cell death caused by HEMA in human primary gingival fibroblasts. *Biomaterials* **2006**, 27, 1803-1809.
216. Heldin, C.H.; Rubin, K.; Pietras, K.and Ostman, A. High interstitial fluid pressure - an obstacle in cancer therapy. *Nat Rev Cancer* **2004**, 4, 806-813.
217. Rebodos, R.L.and Vikesland, P.J. Effects of oxidation on the magnetization of nanoparticulate magnetite. *Langmuir* **2010**, 26, 16745-16753.
218. Available from: http://www.magforce.de/english/clinical-trials/overview.html.
219. Wehner, H.; von Ardenne, A.and Kaltofen, S. Whole-body hyperthermia with water-filtered infrared radiation: technical-physical aspects and clinical experiences. *Int J Hyperthermia* **2001**, 17, 19-30.
220. Issels, R.D.; Abdel-Rahman, S.; Wendtner, C.; Falk, M.H.; Kurze, V.; Sauer, H.; Aydemir, U.and Hiddemann, W. Neoadjuvant chemotherapy combined with regional hyperthermia (RHT) for locally advanced primary or recurrent high-risk adult soft-tissue sarcomas (STS) of adults: long-term results of a phase II study. *Eur J Cancer* **2001**, 37, 1599-1608.
221. Charafe-Jauffret, E.; Ginestier, C.and Birnbaum, D. Breast cancer stem cells: tools and models to rely on. *BMC Cancer* **2009**, 9, 202.

222. Krakstad, C.and Chekenya, M. Survival signalling and apoptosis resistance in glioblastomas: opportunities for targeted therapeutics. *Mol Cancer* **2010**, 9, 135.

223. Festjens, N.; Vanden Berghe, T.and Vandenabeele, P. Necrosis, a well-orchestrated form of cell demise: signalling cascades, important mediators and concomitant immune response. *Biochim Biophys Acta* **2006**, 1757, 1371-1387.

224. Apopa, P.L.; Qian, Y.; Shao, R.; Guo, N.L.; Schwegler-Berry, D.; Pacurari, M.; Porter, D.; Shi, X.; Vallyathan, V.; Castranova, V.and Flynn, D.C. Iron oxide nanoparticles induce human microvascular endothelial cell permeability through reactive oxygen species production and microtubule remodeling. *Part Fibre Toxicol* **2009**, 6, 1.

225. Seton-Rogers, S. Cancer stem cells: Survival skills. *Nat Rev Cancer* **2009**, 9, 147-147.

226. *Non-Small Cell Lung Cancer Treatment (PDQ®)*. Available from: http://www.cancer.gov/cancertopics/pdq/treatment/non-small-cell-lung/patient.

227. Shaw, E.G.; Brindle, J.S.; Creagan, E.T.; Foote, R.L.; Trastek, V.F.and Buskirk, S.J. Locally recurrent non-small-cell lung cancer after complete surgical resection. *Mayo Clin Proc* **1992**, 67, 1129-1133.

228. Kelsey, C.R.; Marks, L.B.; Hollis, D.; Hubbs, J.L.; Ready, N.E.; D'Amico, T.A.and Boyd, J.A. Local recurrence after surgery for early stage lung cancer: an 11-year experience with 975 patients. *Cancer* **2009**, 115, 5218-5227.

229. Thomas, P.and Rubinstein, L. Cancer recurrence after resection: T1 N0 non-small cell lung cancer. Lung Cancer Study Group. *Ann Thorac Surg* **1990**, 49, 242-246; discussion 246-247.

230. Jung, H. Interaction of thermotolerance and thermosensitization induced in CHO cells by combined hyperthermic treatments at 40 and 43 degrees C. *Radiat Res* **1982**, 91, 433-446.

231. Chittasupho, C.; Xie, S.X.; Baoum, A.; Yakovleva, T.; Siahaan, T.J.and Berkland, C.J. ICAM-1 targeting of doxorubicin-loaded PLGA nanoparticles to lung epithelial cells. *Eur J Pharm Sci* **2009**, 37, 141-150.

232. Grabarek, Z.and Gergely, J. Zero-length crosslinking procedure with the use of active esters. *Analytical Biochemistry* **1990**, 185, 131-135.

233. Zhang, G.; Fandrey, C.; Naqwi, A.and Wiedmann, T.S. High-frequency ultrasonic atomization for drug delivery to rodent animal models - optimal particle size for lung inhalation of difluoromethyl ornithine. *Exp Lung Res* **2008**, 34, 209-223.

234. Liao, X.; Liang, W.; Wiedmann, T.; Wattenberg, L.and Dahl, A. Lung distribution of the chemopreventive agent difluoromethylornithine (DFMO) following oral and inhalation delivery. *Exp Lung Res* **2004**, 30, 755-769.

235. Xie, Y.; Longest, P.W.; Xu, Y.H.; Wang, J.P.and Wiedmann, T.S. In vitro and in vivo lung deposition of coated magnetic aerosol particles. *J Pharm Sci* **2010**, 99, 4658-4668.

236. Corti, C.; Pratesi, G.; DeCesare, M.; Pellegrini, R.; Giardini, R.; Supino, R.and Zunino, F. Spontaneous lung metastases in a human lung tumor xenograft: a new experimental model. *J Cancer Res Clin Oncol* **1996**, 122, 154-160.

237. Hastings, R.H.and Summers-Torres, D. Direct Laryngoscopy in Mice. *Contemp Top Lab Anim Sci* **1999**, 38, 33-35.

238. Frank, J.A.; Kalish, H.; Jordan, E.K.; Anderson, S.A.; Pawelczyk, E.and Arbab, A.S. Color transformation and fluorescence of Prussian blue-positive cells: implications for histologic verification of cells labeled with superparamagnetic iron oxide nanoparticles. *Mol Imaging* **2007**, 6, 212-218.

239. Taratula, O.; Garbuzenko, O.B.; Chen, A.M.and Minko, T. Innovative strategy for treatment of lung cancer: targeted nanotechnology-based inhalation co-delivery of anticancer drugs and siRNA. *J Drug Target* **2011**, 19, 900-914.

240. Drazen, J.M.; Finn, P.W.and De Sanctis, G.T. Mouse models of airway responsiveness: physiological basis of observed outcomes and analysis of selected examples using these outcome indicators. *Annu Rev Physiol* **1999**, 61, 593-625.

241. Chen, C.H., S; Mohite, V; Yuan, H; Chatterjee, J; Haik, Y, *Nanomagnetics and magnetic hyperthermia*, in *Cancer nanotechnology: Nanomaterials for cancer diagnosis and therapy*, W.T. Nalwa HS, Editor. 2007, American Scientific: San Diego, CA. p. 160 - 191.

242. Hu, R.; Ma, S.; Li, H.; Ke, X.; Wang, G.; Wei, D.and Wang, W. Effect of magnetic fluid hyperthermia on lung cancer nodules in a murine model. *Oncol Lett* **2011**, 2, 1161-1164.

243. Hu, R.; Zhang, X.; Liu, X.; Xu, B.; Yang, H.; Xia, Q.; Li, L.; Chen, C.and Tang, J. Higher temperature improves the efficacy of magnetic fluid hyperthermia for Lewis lung cancer in a mouse model. *Thoracic Cancer* **2012**, 3, 34-39.

244. Jaracz, S.; Chen, J.; Kuznetsova, L.V.and Ojima, I. Recent advances in tumor-targeting anticancer drug conjugates. *Bioorg Med Chem* **2005**, 13, 5043-5054.

245. Garbuzenko, O.B.; Saad, M.; Betigeri, S.; Zhang, M.; Vetcher, A.A.; Soldatenkov, V.A.; Reimer, D.C.; Pozharov, V.P.and Minko, T. Intratracheal versus intravenous liposomal delivery of siRNA, antisense oligonucleotides and anticancer drug. *Pharm Res* **2009**, 26, 382-394.

246. Li, Z.; Zhao, R.; Wu, X.; Sun, Y.; Yao, M.; Li, J.; Xu, Y.and Gu, J. Identification and characterization of a novel peptide ligand of epidermal growth factor receptor for targeted delivery of therapeutics. *The FASEB Journal* **2005**, 19, 1978-1985.

247. Brown, E.; McKee, T.; diTomaso, E.; Pluen, A.; Seed, B.; Boucher, Y.and Jain, R.K. Dynamic imaging of collagen and its modulation in tumors in vivo using second-harmonic generation. *Nat Med* **2003**, 9, 796-800.

248. Eikenes, L.; Bruland, Ø.S.; Brekken, C.and Davies, C.d.L. Collagenase Increases the Transcapillary Pressure Gradient and Improves the Uptake and Distribution of Monoclonal Antibodies in Human Osteosarcoma Xenografts. *Cancer Research* **2004**, 64, 4768-4773.